UNIVERSITY OF CALIFORNIA
Santa Barbara

Development of Semipolar III-Nitride Vertical-Cavity Surface-Emitting Lasers

A dissertation submitted in partial satisfaction of the requirements for the degree

Doctor of Philosophy

in

Materials

By

Jared A. Kearns

Committee in charge:

Professor Shuji Nakamura, Chair

Professor Steven P. DenBaars

Professor James S. Speck

Dr. Daniel A. Cohen

September 2020

The dissertation of Jared A. Kearns is approved.

_____

James S. Speck

_____

Steven P. DenBaars

_____

Daniel A. Cohen

_____

Shuji Nakamura (Committee Chair)

August 2020

Development of Semipolar III-Nitride Vertical-Cavity Surface-Emitting Lasers

by

Jared A. Kearns

Acknowledgements

There are many people that have contributed to helping me reach this point and there is no way that I could properly thank them all. However, I would like to thank my committee members for their support, advice, and direction through my time here. I want to especially thank my advisor Prof. Shuji Nakamura for his unwavering optimism that no matter how many roadblocks I ran into I would eventually get some working lasers. I would also like to particularly thank Dr. Dan Cohen for his patience with me as I continually asked him questions on any topic I was curious about. Outside my committee, I would like to thank Dr. Brian Thibeault and Dr. Demis John for all their help talking through processing issues and just life in general. I have learned a lot from all of them and would not have been able to complete this project without them.

In terms of garnering my interest in science, I would like to thank my high school physics teacher Dr. Johnathan Eales for instilling a love of physics. I would also like to thank my undergraduate professors Prof. Yonathan Thio and Prof. Pradeep Agrawal for pushing me to consider graduate school. Without them my path would likely have been very different.

Finally, I want to thank all my family, friends, and fellow researchers who have not only helped me solve complex technical issues but have also made grad school fun. To the SSLEEC research group past and present, thank you for all the great conversations, for all that I have learned, and for being there to pick me up when experiments didn't work out as well as I might have hoped. I am grateful to my housemates Sanjeev Kolli, Sean Murray, and Naga Sri Harsha Gunda in addition to everyone else who made living here enjoyable for helping me to forget about work. I would especially like to thank my family for supporting me and pushing me to go further. Finally, I would like to thank Elohim for His continual guidance, support, and assistance. Without His help I never would have made it this far.

Curriculum Vitae

Jared Kearns

kearns@ucsb.edu

Education

University of California, Santa Barbara **Aug 2016 - Present**
- Ph.D. – Materials
- Advisor: Shuji Nakamura
- Research focus: semi-polar vertical-cavity surface-emitting lasers

Georgia Institute of Technology **Aug 2012 - May 2016**
- Bachelor of Science – Chemical and Biomolecular Engineering
- Minor: Leadership Studies
- Overall GPA: 3.98/4.0

International School of Bangkok **Aug 2008 – June 2012**
- High school and International Baccalaureate diploma
- Jared Kearns, Hole Size in a Spherical Resonator, ISB Journal of Physics (2012)

Experience

UCSB Materials Department – Graduate Student Researcher **Sept 2016 – Present**
- Shuji Nakamura's Lab
- Investigated bulk production of ternary III-N alloys using the basic ammonothermal method
- Design, grow, fabricate, and test GaN based VCSELs and LEDs

UCSB Materials Department – Teaching Assistant **Sept 2016 – Dec 2016**
- Developed and taught supplemental lessons for students

Binergy Scientific Inc. – Test Engineer **May 2015 – July 2016**
- Designed and tested parts for biosensor product development
- Wrote code for prototype testing

Georgia Tech – Undergraduate Student Researcher **Jan 2014 – May 2015**
- Gleb Yushin's Lab
- Investigated production of novel states of aluminum through electrochemical treatments

Rhodia, Member of the Solvay Group – Production Engineer **May 2013 – Aug 2013**
- Optimized operational batch size planning, and updated manufacturing procedures
- Developed preventative maintenance plans for critical equipment
- Conducted an internal review for OSHA compliance

Skills

Characterization: AFM, Chromatography, EBSD, EDX, electroluminescence, ellipsommetry, FIB, mass spectroscopy, NMR, photoluminescence, profilometry, QCM, SEM, SIMS, UV-Vis-IR spectroscopy, XRD, XRR

Fabrication: MOCVD, IBD, RIE, ICP, thermal/e-beam evaporation, photolithography, photo electrochemical etching, flip-chip bonding, stepper, thermal oxidation

Programs: ASPEN, FIMMWAVE, Google Sketch Up, L-Edit, MATLAB, Microsoft Office, Origin, TFCalc, Vertical, SiLENSe, SRIM/TRIM

Awards

- SSLEEC Outstanding Researcher Award **Nov 2017, Nov 2019**
- Dean's List at Georgia Tech **Aug 2012 - May 2016**
- Chevron Merit Scholarship **Aug 2014 - May 2015**
- Shell Merit Scholarship **May 2014 – Aug 2014**
- National Honors Society **Mar. 2011 - Present**

Activities and Leadership

- School on Wheels tutor **Dec 2016 - Present**
- Reality Santa Barbara member and volunteer **Sept 2016 – Present**
- Veritas Forum Leader **Jan 2014- May 2016**
- IPA Peer Support **Aug. 2015 – May 2016**
- Solar Jackets member **Jan. 2013 – Dec. 2013**
- Varsity Soccer, Cross Country, Track & Field **Aug 2008 – May 2012**

Publications

1. Jared A. Kearns, Nathan Palmquist, Joonho Back, SeungGeun Lee, Daniel A. Cohen, Steven P. DenBaars, and Shuji Nakamura, *Blue semipolar III-nitride vertical-cavity surface-emitting lasers*, Gall. Nitride Mater. Devices XV **11280**, Eds., 15, SPIE, https://doi.org/10.1117/12.2540508 (2020).
2. Jared A. Kearns, Joonho Back, Daniel A. Cohen, Steven P. DenBaars, and Shuji Nakamura, *Demonstration of blue semipolar (20-2-1) GaN-based vertical-cavity surface-emitting lasers*, Optics Express, https://doi.org/10.1364/OE.27.023707 (2019)
3. Jared A. Kearns, Joonho Back, Nathan C. Palmquist, Daniel A. Cohen, Steven P. DenBaars, Shuji Nakamura, *Inhomogeneous Current Injection and Filamentary Lasing of Semipolar (20-2-1) Blue GaN‐Based Vertical‐Cavity Surface‐Emitting Lasers with Buried Tunnel Junctions*, physica status solidi (a), https://doi.org/10.1002/pssa.201900718 (2019)
4. Matthew S. Wong, Jared A. Kearns, Changmin Lee, Jordan M. Smith, Cheyenne Lynsky, Guillaume Lheureux, Hyoshik Choi, Jinwan Kim, Chaehon kim, Shuji Nakamura, James S. Speck, and Steven P. DenBaars, *Improved performance of AlGaInP red micro-light-emitting diodes with sidewall treatments*, Opt. Express **28**(4), 5787 https://doi.org/10.1364/oe.384127 (2020).
5. SeungGeun Lee, Charles A. Forman, Jared Kearns, John T. Leonard, Daniel A. Cohen, Shuji Nakamura, and Steven P. DenBaars, *Demonstration of GaN-based vertical-cavity surface-emitting lasers with buried tunnel junction contacts*, Optics Express, https://doi.org/10.1364/OE.27.031621 (2019)
6. Steven Griffiths, Siddha Pimputkar, Jared Kearns, Thomas Malkowski, Michael Doherty, James Speck, Shuji Nakamura, *Growth Kinetics of Basic Ammonothermal Gallium Nitride Crystals*, Journal of Crystal Growth, http://dx.doi.org/10.1016/j.jcrysgro.2018.08.028 (2018)
7. Charles Forman, SeungGeun Lee, Erin Young, Jared Kearns, Daniel Cohen, John Leonard, Tal Margalith, Steven DenBaars, Shuji Nakamura, *Continuous-wave operation of m-plane GaN-based vertical-cavity surface-emitting lasers with a tunnel junction intracavity contact*, Applied Physics Letters, https://doi.org/10.1063/1.5007746 (2018)
8. SeungGeun Lee, Charles Forman, Changmin Lee, Jared Kearns, Erin young, John Leonard, Daniel Cohen, James Speck, Shuji Nakamura, Steven Denbaars, *GaN-based vertical-cavity surface-emitting lasers with tunnel junction contacts grown by metal-*

organic chemical vapor deposition, Applied Physics Express, https://doi.org/10.7567/APEX.11.062703 (2018)

9. SeungGeun Lee, Charles A. Forman, Changmin Lee, Jared Kearns, John T. Leonard, Daniel A. Cohen, James S. Speck, Shuji Nakamura, and Steven P. DenBaars, *A violet III-nitride vertical-cavity surface-emitting laser with a MOCVD-grown tunnel junction contact*, Conference on Lasers and Electro-Optics, https://doi.org/10.1364/CLEO_SI.2018.SF1G.7 (2018)
10. Charles A. Forman, SeungGeun Lee, Erin C. Young, Jared A. Kearns, Daniel A. Cohen, John T. Leonard, Tal Margalith, Steven P. DenBaars, Shuji Nakamura, *Continuous-wave operation of nonpolar GaN-based vertical-cavity surface-emitting lasers*, Proc. SPIE 10532, Gallium Nitride Materials and Devices XIII, https://doi.org/10.1117/12.2314885 (2018)
11. Matthew S. Wong, Changmin Lee, Daniel J. Myers, David Hwang, Jared A. Kearns, Thomas Li, James S. Speck, Shuji Nakamura, and Steven P. DenBaars, *Size-independent peak efficiency of III-nitride micro-light-emitting-diodes using chemical treatment and sidewall passivation*, Applied Physics Express, https://doi.org/10.7567/1882-0786/ab3949 (2019)
12. Hongjian Li, Matthew S. Wong, Michel Khoury, Bastien Bonef, Haojun Zhang, YiChao Chow, Panpan Li, Jared Kearns, Aidan A. Taylor, Philippe De Mierry, Zainuriah Hassan, Shuji Nakamura, and Steven P. DenBaars, *Study of efficient semipolar (11-22) InGaN green micro-light-emitting diodes on high-quality (11-22) GaN/sapphire template*, Optics Express, https://doi.org/10.1364/OE.27.024154 (2019)

Patents

- Multifaceted III-Nitride Surface-Emitting Laser, UC Case 2018-253-0, *Patent Pending*
- Vertical Cavity Surface-Emitting Lasers with Continuous Wave Operation, UC Case 2018-250-0
- III-Nitride Based VCSEL with Curved Mirror on P-Side of the Aperture, UC Case 2019-934-0, *Patent Pending*

Conferences and presentations

- Laser Display and Lighting Conference (LDC), Yokohama, Japan, 2020, invited speaker
- SPIE Photonics West, San Francisco, USA, 2020, invited speaker
- SSLEEC Review, Santa Barbara, USA, 2019, oral presentation
- International Conference on Nitride Semiconductors (ICNS), Bellevue, Washington, 2019, oral presentation
- SSLEEC Review, Santa Barbara, USA, 2018, oral presentation
- International Workshop on Nitride Semiconductors (IWN), Kanazawa, Japan, 2018, oral presentation

Abstract

Development of Semipolar III-Nitride Vertical-Cavity Surface-Emitting Lasers
By
Jared A. Kearns

III-N vertical-cavity surface-emitting lasers (VCSELs) show promise for numerous communications, lighting, display, and sensor applications due to their low threshold current, high beam quality, and arraying capabilities. Primarily, research has been focused on using c-plane based devices, but non-basal growth planes provide an interesting alternative due to a reduced quantum confined Stark effect; higher material gain; lower transparency current density; and inherent polarized emission. The anisotropic gain leads to VCSELs and VCSEL arrays where each laser is polarization locked along the a-direction. At UCSB, an m-plane VCSEL was first demonstrated in 2012 under pulsed injection and in 2018 under CW operation. Through that time, the device performance has improved and the polarization properties of the VCSELs has been experimentally verified. However, the wavelength of m-plane lasers is severely limited due to poor indium incorporation and high defect formation, inhibiting their adoption in many applications. This led to the question of how the benefits of using m-plane can be retained, such as the inherent polarization, while expanding the available wavelengths.

The answer that was developed in this thesis is the use of a semipolar growth plane with higher indium uptake. After developing an epitaxial growth recipe and optimizing processing parameters for semipolar planes, we achieved the first demonstration of semipolar $(20\bar{2}1)$ VCSELs which were experimentally shown to be polarization locked along the a-direction and emit in the blue region. The devices had a 5λ cavity length, an ion implanted aperture, and a dual dielectric DBR design and showed an improvement in the differential efficiency, threshold current density and

total output power relative to m-plane VCSELs with the same design. However, there were issues. The devices were only able to lase under pulsed operation, up to a 70% duty cycle. Focused ion beam images in conjunction with COMSOL modeling was used to identify the key structural features that contributed to the high measured thermal impedance. Nearfield images suggest that the LP_{01} mode was lasing near the edge of the aperture. This commonly observed spatial misalignment introduced additional sources of loss beyond the expected material absorption loss, including mode overlap with the implanted region and the metal contacts. The effect of these absorbing layers on the device performance relative to simulation models was estimated and highlighted the need for proper mode control.

To improve the optical confinement, devices using a buried tunnel junction (BTJ) scheme to confine the current were fabricated and were found to lack the excess losses due to absorption seen on the initial semipolar samples. Significant filamentation was observed on these samples and several characterization methods, including optical and thermal nearfield images, were used to identify the source of the filamentation. Further comparison of multiple BTJ samples with different index guiding showed that the mode behavior was driven by the interplay of inhomogeneous current injection and index guiding. The cause of the inhomogeneous current injection is projected to be due to doping variations in the p-GaN but still requires further investigation for verification.

Table of Contents

1 Introduction

Vertical-cavity surface-emitting lasers (VCSELs) are characterized by having an output beam that is emitted perpendicular to the substrate surface as compared to a conventional edge emitting laser diodes (EELD) which emits parallel. While the transition from emitting "sideways" to "up" may seem trivial, the required changes to the device design are anything but. VCSELs have gained prominence since their inception in 1977 due to a number of inherent advantages over LEDs and EELDs[1]. A wide range of wavelengths are commercially available for a variety of applications, with devices emitting between 650 nm and 1300 nm and are typically GaAs based. Longer wavelengths are often based on dilute nitrides GaInNAs or InP based alloys with the arsenide system. However, a shorter wavelength device is not yet available despite being beneficial for many applications. To this end, we have turned to the III-N system which has been imperative for achieving efficient LEDs and EELDs with UV and visible wavelengths. This introduction section will give an overview of VCSEL applications, with a focus on high impact and growth markets that would be impacted by the availability of visible wavelengths. It will follow with an overview of the semiconductor materials and laser physics that will be relevant for the results discussed in the later chapters. The VCSEL design aspects that are significant for the III-N system will be presented before stating a summary of the work that was done previously at UCSB.

1.1 VCSEL Applications

VCSELs have several advantages over typical light emitting diodes (LEDs) or edge emitting laser diodes (EELDs) that make them desirable for a range of applications. Typical of lasers, they have a narrow spectral peak, high modulation speed, high brightness, and highly

directional emission that an LED cannot match. However, they retain many of the advantages of an LED, such as 2D arraying capability, on chip testing, low cost, high reliability, and low power consumption that are lost with EELDs. Additionally, the circular beam emission from a VCSEL is generally superior to the stigmated beam from an EELD in terms of fiber coupling efficiency and ease of optical control. The relatively short cavity length increases thermal stability of the mode but limits the dynamic range and wavelength tunability. They are more complicated to fabricate than LEDs and have a much lower output power than EELDs, which does limit their uses, but new applications continue to be discovered that can capitalize on the VCSEL's strengths.

Arsenide and phosphide VCSELs have reached a level of maturity allowing widespread adoption, traditionally as optical interconnects used in data transfer[2]. However, III-nitride devices still have a way to go despite recent research improvements before they are widespread. III-Nitride (III-N) VCSELs have potential for applications ranging from pico-projectors to laser lighting to bio-sensing, some of which will be presented below. Each application's requirements vary, but in general having a high power, low threshold VCSEL with a uniform beam emission profile for a range of wavelengths would be beneficial.

Research and Markets estimated that by 2025 the VCSEL market will reach 2.9 billion USD with a compound annual growth rate of 23.7%[3]. This increase in demand is expected to be primarily due to the ever-increasing demand for data communication, the implementation of VCSELs for 3D sensing in consumer electronics, and their use in LiDAR for autonomous vehicles. Several emerging applications, such as atomic clocks, illumination, and displays were projected to grow rapidly in the next few years by taking advantage of recent research advances[4]. As III-N VCSELs are not currently commercially available, the applications

discussed below will include both potential VCSEL applications as well as applications that currently use VCSELs from other material systems that may also be able to use GaN based ones.

1.1.1 Current VCSEL Applications

1.1.1.1 Data Communication

The ever-expanding requirements for data communication with increased cloud computing, and streaming services raises demand on information transfer hardware, such as lasers, that provide server to server data transfer in data centers. VCSELs were initially introduced to the data communications industry in 1996 and quickly replaced the existing edge emitting lasers due to their increased reliability and temperature stability to become the most used laser type in data communication networks[5]. Most of the data communication VCSELs operate at 850 nm and are typically used for low cost multimode fiberoptic interconnects to transmit over a short range. Line rates have grown from 1 Gbps to over 85 Gbps and different multiplexing schemes allow for the use of a multi-channel VCSEL arrays to reach even faster speeds per module. While 100 Gbps modules are expected to continue to replace the previous 40 Gbps ones for the next few years, transceivers with rates over 400 Gbps are being developed[5,6]. Despite the high speeds achievable, the low power and subsequently low transmission range

is expected to be the limiting factor in their market development[3].

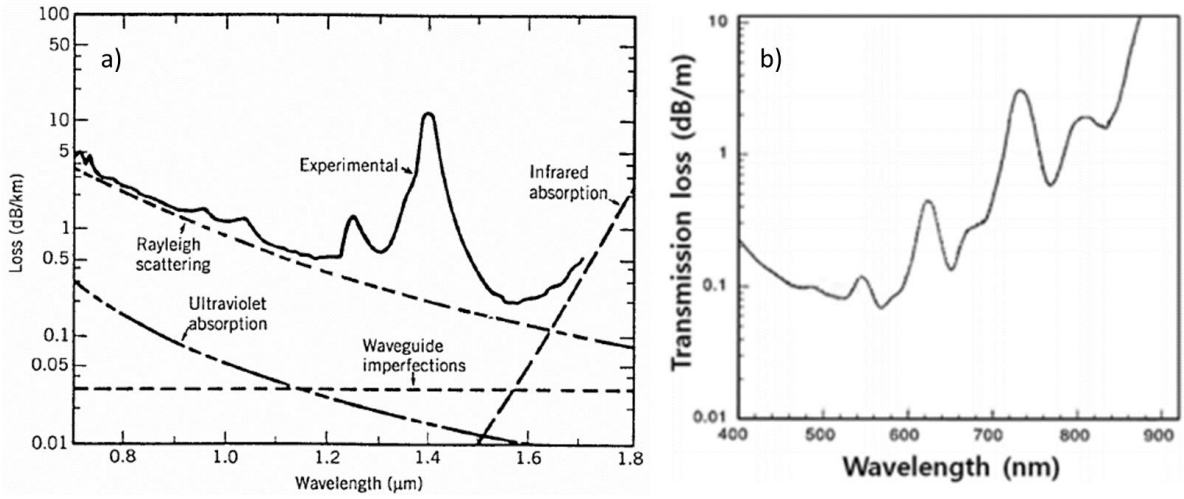

Figure 1-1 Shows the absorption spectra of a typical silica optical fiber (a) and a PMMA fiber (b)[7,8]. Reprinted by permission from Springer Nature ©2012.

While it is unlikely III-N based VCSELs will compete in data center applications anytime soon, they may present the optimal device for improving applications where III-N based LEDs are currently used, specifically in plastic optical fiber (POF) data transmission. POF is low cost, has higher mechanical stability, easier handling, and easier light coupling than traditional silica based fiber, making it desirable to use for commonplace short range data transmission like automobiles or home networks[9]. Polymethyl methacrylate (PMMA) based fibers have absorption minima in the green (~500 nm) and red (~650 nm) regions of the spectra. Green GaN based LEDs have the lower attenuation and higher temperature stability than the red arsenide-based devices leading to their implementation in vehicle optical fiber networks. However, the modulation speed of LEDs is severely limited relative to a laser. Therefore, a green or blue VCSEL could retain the advantageous use of POF, while allowing for increased data rates.

1.1.1.2 Sensors

Aside from communication, a major application for VCSELs lies in sensing. This ranges from determining relative distance and speed to object identification or chemical detection. The largest sector historically has been in producing doppler interferometers that have been used in optical mice; however, two recent applications are highlighted here that are expected to significantly increase VCSEL demand in the coming years. They use two different methods for sensing distance: light detection and ranging (lidar) and depth mapping with structured light.

With the push for autonomous and semi-autonomous vehicles, it is important to be able to sense and model the surrounding accurately. Most attempts at fully autonomous cars use a system that incorporates lidar due to its high resolution, ability to prepare 3D images, and ability to sense in low light settings. Time of flight lidar has also been implemented in the recent iPad Pro, showing its applicability to consumer products as well[10].

Due to their low power, VCSELs are better suited to short range lidar systems, though large arrays can overcome the power limitation. Using arrays of VCSELs can improve the reliability of a lidar system compared to one based on edge emitters by having far more emitting elements. If a few VCSELs fail in an array, then it is more likely for sufficient light to still be produced than if an edge emitter fails in a system with only a couple lasers[11].

The wavelength used for the automotive lidar laser is often chosen to match dips in the solar spectrum caused by adsorption of water vapor in the atmosphere to reduce the background noise in the system and keep from emitting in the visible. However, lidar used in other environments require different emitter wavelengths, such as the green lasers needed for underwater lidar[12].

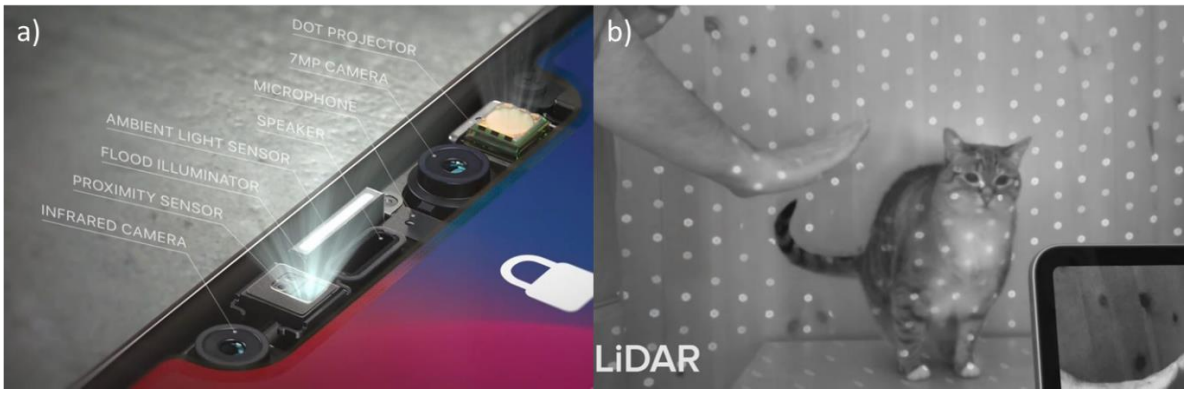

Figure 1-2 Shows the top bar of an iPhone with the VCSEL based dot projector (a) an infrared image of the light pattern used for the iPad's lidar (b)[13,14].

In 2017, Apple released the iPhone X which used the second method for distance measurement, structured light illumination, for facial recognition[15]. A VCSEL array was chosen as the illumination element and the popularity of this system brought VCSELs into the public light, paving the way for their incorporation in mass market products. Using structured light has the advantage of being very accurate within its standard working distance, which is necessary for a security feature such as facial recognition and is relatively insensitive to background light[11,16]. However, it requires complex image processing and has a short operating range. For this approach, patterned light is first emitted from the light source and then reflects off a surface within the working distance of the system. As the depth of the reflective surface changes the local interdot spacing of the reflected pattern changes. A camera is used to record the reflected pattern and the distortions in the initial pattern are analyzed to generate the depth map. In the phone, a VCSEL array was used as the illumination source and was collimated by a lens into a diffractive optical element (DOE). That DOE then split the beams such that over 30,000 dots were projected on a user's face[17]. Using a DOE that can replicate a pattern of input beams allows for the final pattern to have a dot pitch that is less than the minimum pitch between VCSELs during fabrication[11]. This increases the resolution of the sensor. VCSELs are also used in the proximity sensor and the auto focus but operate in a time-of-flight

orientation due to its simplicity and longer range. The 3D mapping using structured light is also being developed for gesture recognition and other novel machine interfacing methods.

1.1.1.3 Atomic Clocks

Atomic clocks are instrumental in accurate navigational positioning and for a variety of scientific measurements; however, they are often large setups based on a RF cavity that require significant power consumption to maintain. Being able to reduce the size and power consumption of such a system by moving to an all optical system would potentially allow for GPS-free navigation in consumer electronics or vehicles. The first demonstration of an all optical atomic clock based on a modulated GaAs based VCSEL pumping cesium atoms was in 2000[18]. This method used a coherent population trapping (CPT) technique with, typically, either cesium or rubidium. The requirements on the VCSEL used in atomic clocks is much more stringent than in other applications as the wavelength must very precisely match an atomic transition with a small linewidth; it must operate under single mode operation; emit with a single linear polarization; have a high modulation speed; have a low power consumption; and have a low relative intensity noise.

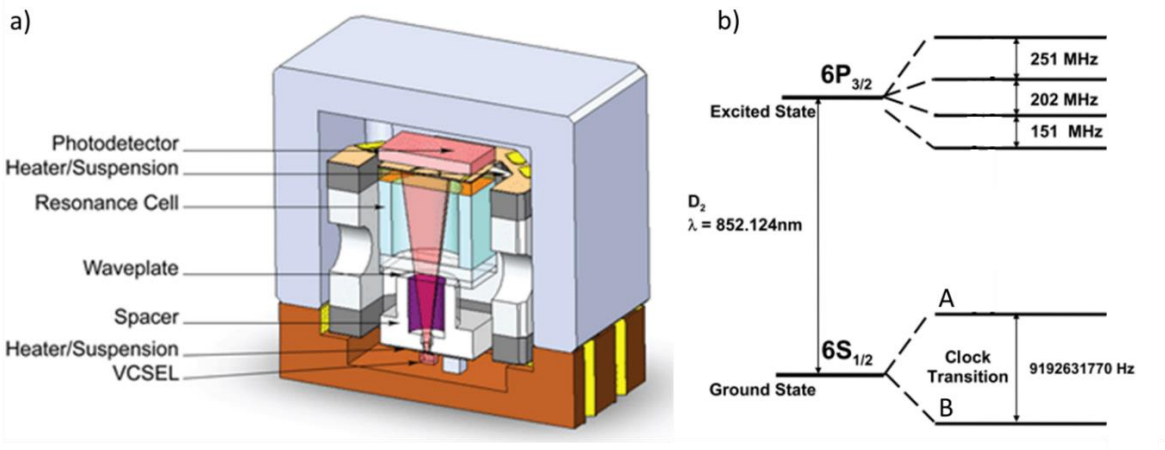

Figure 1-3 Shows a schematic of an all optical atomic clock (a) and the cesium energy levels that show the hyperfine splitting (b)[19,20].

In cesium, the $6S_{1/2}$ ground state is split into two sublevels due to the interaction between the electronic and nuclear spins, as shown in Figure 1-3(b) [18]. This separation is about 9.2 GHz. To achieve CPT, transitions to $6P_{3/2}$ states from both A and B need to be stimulated concurrently. This can be achieved by a single device with frequency modulation. As the drive current of the VCSEL changes, the frequency of light emitted changes as well due to heating. If the device is slightly modulated at 4.6 GHz, then frequency modulated sidebands can be formed at ± 4.6 GHz from the nominal lasing peak. If the DC aspect of the drive current is tuned to halfway between the transitions, then both can be excited simultaneously. When this condition is met, some of the cesium atoms will become optically transparent as they are "trapped" in a superposition of stated that eliminates the net excitation transition probability. This leads to an increase in the transmitted power of a beam aligned to the absorption resonance when modulated at 4.6 GHz, thereby determining the oscillation frequency of the splitting. Due to selection rules, the light needs to be pure circularly polarized at a stable wavelength for the entire operation of the clock, necessitating stable polarization control of the VCSEL. The optimal transition for cesium occurs at 894 nm; therefore, GaAs based devices have been used. Strontium has transitions around 420/460 nm that would be optimal for a GaN based device and present more accurate and stable options than the traditional cesium definition of the second[21].

1.1.2 Potential VCSEL Applications

1.1.2.1 Lighting

GaN based LEDs have led to a dramatic shift in lighting. Due to their high efficiency, small form factors, low toxicity, and significant lifespans they have become the standard illumination

source for a wide range of applications. However, there are some applications that LEDs do not dominate that provide opportunities for laser-based lighting. Specifically, high powered directional lighting, as used in entertainment, architectural lighting, underwater illumination, or automotive lighting, benefits from the advantages of using a laser source[22]. Lasers do not suffer the same efficiency droop at high pump powers as LEDs enabling them to be some of the highest luminance light sources.

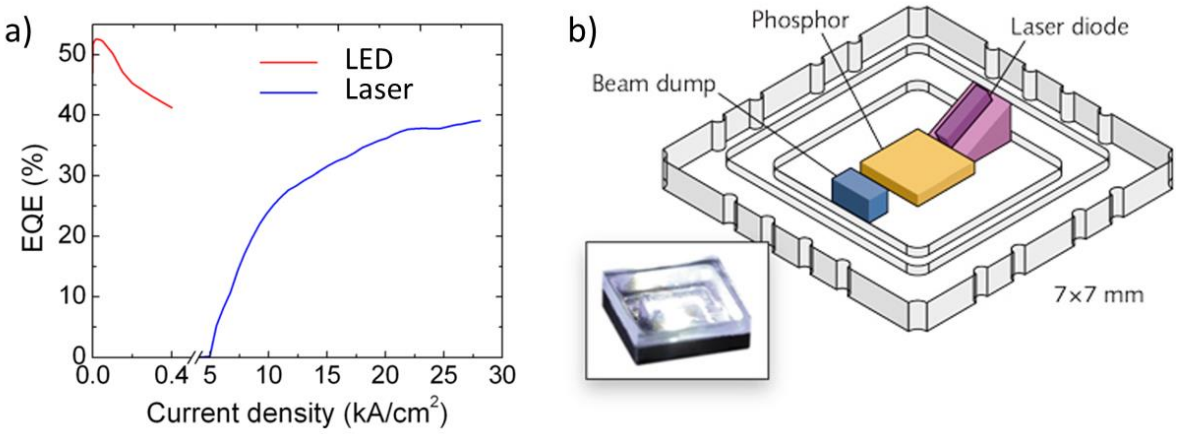

Figure 1-4 Shows the efficiency of LEDs and Lasers as a function of pump power (a). Reprinted from Ref 23 with the permission of AIP Publishing. The laser based light source (b) has a reflection geometry[24].

While a white light source can be formed from the combination of a red, green, and blue laser, the low efficiency of green layers and high cost of reliable high-power red ones means that the majority of white laser lighting involves the use of a blue or violet laser with a phosphor convertor[22]. The efficient coupling of lasers into optical fibers allows for the laser source to be removed from the phosphor and the main light emission point[25]. This can provide additional options in system design, as efficient heatsinks are needed for both the laser and the phosphor for steady and reliable operation.

These laser-based lighting systems are increasingly becoming adopted, with several car manufactures, including BMW and Audi, implementing a laser-based headlight system in the

luxury models. It has been found that errors in visual perception when driving are five times more likely to occur in the dark[26]. Improving the headlight illumination helps both depth perception and peripheral vision, thereby improving the safety of night driving. The small divergence angle of the illuminator allows for adaptive control of the beam. Therefore, the illumination pattern can be adjusted for changing environments to highlight important information, such as road lines or signs, without blinding people in the surroundings/other drivers. This adaptive control does require accurate sensors for identifying the surroundings and optical elements to keep the light from emitting as a dangerous high-powered coherent laser beam. Thus, design of the phosphor is also very important and can depend heavily on the application power and geometry. Additional safety measures may be needed to ensure that there is no leakage of the laser light before it has interacted with the phosphor and been diffused, which could further increase the cost of such a system.

Traditionally edge emitting lasers have been used for these applications, but if III-N VCSELs can realize some of the advantages shown in traditional GaAs devices, such as being cheaper, more reliable, and having an easily controlled output beam, then VCSEL arrays may present an excellent option for laser-based lighting. Current VCSEL array results have a ~5x higher threshold than edge emitting lasers for a similar total output power[27,28]. Thus, further efficiency improvements are necessary for VCSELs to become serious competition.

1.1.2.2 Visible Light Communication

Another component of using lasers for lighting is the potential to add data communication functionality to lighting systems through light fidelity (LiFi). With the rapid increase in the number of devices that are connected, the demand on data transmission continues to expand. The RF spectrum is getting saturated and new frequencies are needed to keep up with the

continually growing requirements for data transmission. Visible light communication (VLC) offers an attractive option as the visible and IR regions of the spectra are unlicensed and 2600 times larger than the RF spectrum[29]. Additionally, VLC does not induce electromagnetic interference, allowing its use in sensitive environments, such as in hospitals or on airplanes[30].

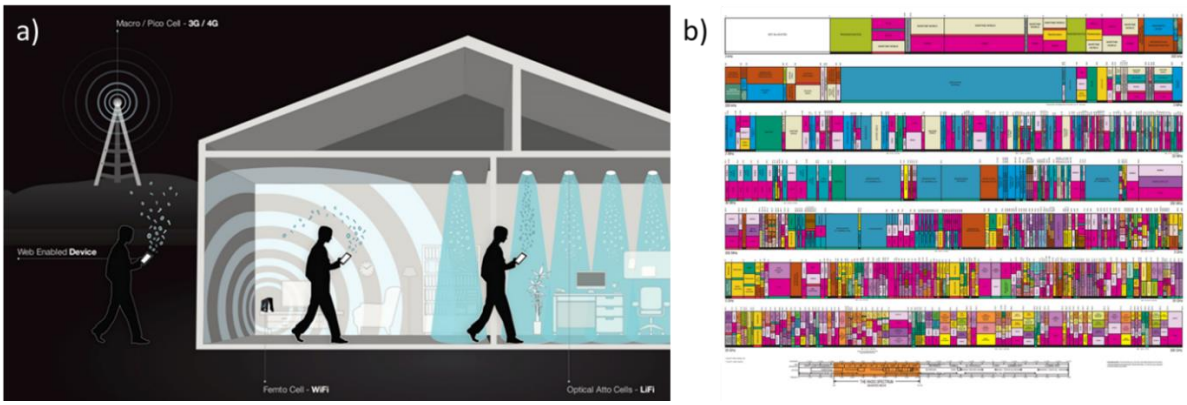

Figure 1-5 Shows an illustration of different methods of wireless communication (a) ranging from cellular on the left, to Wi-Fi in the middle, and a VLC based attocell on the right[31]. The current US frequency allocation chart (b) is quite crowded[32].

VLC also has large potential for underwater communication[33]. The increasing number of wireless sensors, environmental monitoring, or use of autonomous or unmanned vehicles is not limited to the surface and leads to significant difficulties in a medium such as water where the typical RF data transmission frequencies are limited to a few meters range due to the high attenuation. Traditionally acoustic communication has been used under water for its low attenuation, but it is quite slow. Visible light, however, has a relatively low attenuation and has been demonstrated to provide relatively high data rates over tens of meters.

While, lasers have traditionally been the main source for high speed data transfer, initial work on VLC systems was done using LEDs due to their prevalence. The ubiquitous nature of LEDs in lighting gives the option for adding data communication capabilities with limited infrastructural changes needed. Unfortunately, LEDs are severely limited in bandwidth by high RC parasitic effects[30]. Super-luminescent LEDs and μLEDs have been used to combat the

limitations of large area LEDs[34]. The bandwidth of the μLEDs becomes limited by the carrier lifetime instead of the RC time constant. However, these are still an order of magnitude slower than using a laser based source that is limited by the photon lifetime and likely only represent a stepping stone in the progression of VLC technology[35]. The directionality of a laser-based system allows for the information to travel further, increasing the effective range. While most lasers are not eye-safe, after being properly combined with an elastic scattering element, as they would likely be in a laser-based lighting scheme, the coherent laser light can be made safe without sacrificing data transmission speeds. As an alternative, a RGB white light laser system could be used in conjunction with wavelength division multiplexing (WDM) to further increase the data rate from a single fixture[30]. To show this potential, the use of WDM has been demonstrated to work with multiple blue lasers illuminating a single phosphor. Thus, using an array of devices to pump a phosphor may also be a relatively easy way to get very high data rates from a "single light". VCSELs, with their ease of forming 2D arrays, could be an optimal device for this sort of application.

1.1.2.3 Near eye displays

Near eye displays (NED) represent what may be the next major wave of consumer electronics. They are the basis of virtual-reality (VR), augmented-reality (AR), and mixed reality (MR) devices that are being developed by many of the biggest technology companies worldwide[36]. A dominant method has not been identified for most aspects of the devices, producing a wide range of approaches. Currently, μLEDs appear to be the predominant choice for the display source due to their similarity with previous display technology and relative ease of implementation, although they have had limited implementation thus far[37]. Alternatively, there

are several successful implementations of edge emitting lasers that provide high image quality but must deal with the power and optical difficulties associated with lasers[38].

Figure 1-6 Shows an image of Intel's Vaunt smart glasses (a) and Microsoft's HoloLens 2 (b) that used VCSELs and EELDs as illumination sources, respectively[39,40]. A schematic showing the laser light being projected on the retina is shown in (c)[41].

Despite the limited progress in VCSEL research, their potential use as a miniature display was noted in 1994[42]. The 2D array capabilities make their integration much easier than edge emitters, relatively low optical power is beneficial for maintaining eye safety, and the low divergence angle and circularly symmetric beam reduce the additional optical elements that are required. An array can be used that is scanned or swept such that the full image is larger than and has a finer resolution than the device array. This can be used to form a virtual retinal display, where the light is directly projected onto the retina producing an image that is always in focus. To increase the field of view, an important parameter in NEDs, specific optical elements can be used with polarization locked emitters[43].

In 2018, Intel demonstrated such a system that used a red VCSEL to form a monochrome display due to a lack of commercial blue and green devices[39,44]. The laser sits in the frame of the Vaunt glasses and reflects off a holographic reflector on the lens to form a small display on the retina. Later that year, VCSELs were highlighted as an optimal light source for computer-generated hologram displays[45]. Again, the display was a monochromatic red. This highlights the need for the wide wavelength range of III-N based devices.

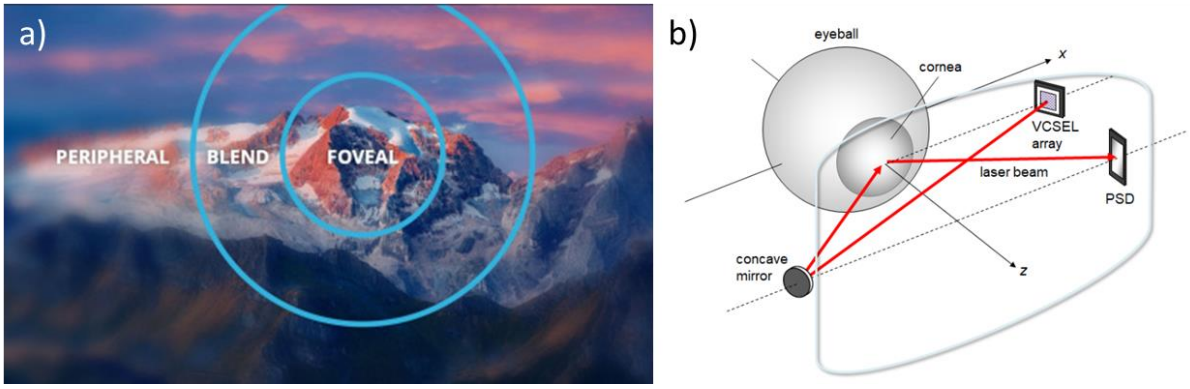

Figure 1-7 Shows a simulated image using foveated rendering to only produce detail where the user is focusing (a)[46]. (b) depicts a sample configuration for measuring the eye rotation with the reflection of a VCSEL emission[47].

In addition to forming the display, VCSELs have also been identified as optimal sources for eye tracking[47]. Foveated rendering has emerged as a popular method to reduce the graphical load in rendering the image by only fully rendering the part of the image the user is focused on[48]. Outside of that area, the image is formed with much lower resolution as it is only seen in the periphery. To achieve this, an accurate measurement of where the eye is focused is needed at all times. It has been shown with an IR device, that a VCSEL emission can be reflected off the cornea such that the angle of reflection can be measured to give the orientation of the eye[47,49]. Directly measuring the spatial coordinates of the eye allows for high speed tracking that enables endpoint prediction of where the eye will focus next. This further reduces the computational power required when the eye is in motion. An array of devices could be used with a position sensitive detector to further increase the sensitivity of the eye-tracking by observing how the overall shape of the reflection changes. Being able to combine a VCSEL based display system with the eye tracking system would allow for a cheaper and lighter system that consumes less power.

In all, VCSELs are used in a variety of applications currently and show promise for many more. These applications generally capitalize on the low cost, low power consumption and

high beam quality that VCSELs provide and are often limited by the low output powers of individual devices. However, there are some applications that are more reliant on stable single mode emission with known polarization and are more inhibited by the wavelengths available. III-nitride based devices are promising to ameliorate that lack, and thus we shall look at this material system in the next section.

1.2 III-N Optoelectronics

GaN is a wide bandgap semiconductor with a wurtzite crystal structure, different planes are shown in Figure 1-8. It first garnered interest in the late 1960s but research was stymied for around 20 years due to the high impurity concentration and inability to dope as a conductive p-type material[50]. The III-N material system spans a wide range of wavelengths, meaning it is potentially useful in many different systems. However, the lattice mismatch between the different binary alloys induces significant strain when the disparate materials are incorporated into one structure. This limits the achievable compositions and is the topic of continuing development.

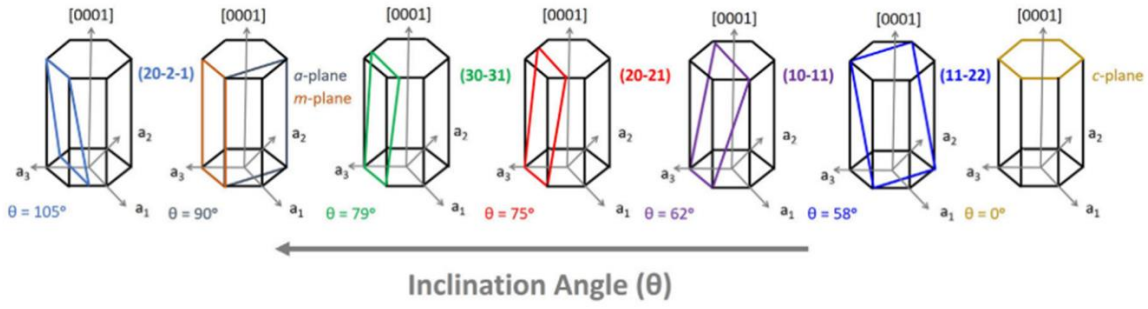

Figure 1-8 Shows the hexagonal crystal structure of GaN and some common non-basal planes[51]. Copyright Wiley-VCH GmbH. Reproduced with permission.

Until the late 1980s GaN was considered to have limited usefulness due to the poor growth quality and lack of a p-type dopant. The use of Si as a n-type dopant was known initially, but

the use of Mg to produce efficient and relatively conductive p-type material wasn't determined until much later. Between 1989 and 1996, Shuji Nakamura, Isamu Akasaki, and Hiroshi Amano separately developed methods to heteroepitaxially grow GaN, reliably dope as p-type, and fabricate efficient double heterostructure LEDs, which later won them the Nobel Prize in Physics in 2014. Since then, interest in the material system has expanded and it has become the core component in a wide variety of applications.

1.2.1 MOCVD Growth

The thin film epitaxial layers that make up the GaN based devices are typically grown using metal-organic chemical-vapor deposition (MOCVD) due to its uniformity, doping control, growth rate, interface control, and throughput[52]. This involves flowing gaseous metal-organic precursors over a growth substrate at elevated temperatures to induce a chemical reaction at the growth surface, leaving the metal atom from the organometallic bonded to a nitrogen and sweeping the organic side chains into the exhaust. The overall process is highly dependent on the inlet composition and the ambient temperature and pressure. The lasers presented in this thesis were grown on freestanding GaN substrates; thus, the formation of a high quality GaN template on foreign substrates, such as sapphire, will not be discussed.

1.2.1.1 Inlet Flow Composition

While the nitrogen is typically introduced via thermally cracked ammonia, the group III elements have a variety of possible precursors, with the most common being trimethyl-III, or triethyl-III. The dopants are typically introduced with bis(cyclopentadienyl)magnesium (Cp_2Mg) for magnesium doped p-type and silane (SiH_4) or disilane (Si_2H_6) for silicon doped n-type. The basic reaction that occurs is given by[53]:

$$M(R)_3 + NH_3 \rightarrow MN + 3\,RH$$

where M is the metal atom and R is the organic sidechain. The reaction mechanisms are not well understood, though it is thought that there are two predominant pathways. The first involves gas phase decomposition of the metal organic which then reacts with the nitrogen to result in heterogeneous decomposition of the ammonia on the substrate surface. The next mechanism involves an initial reaction of the metal organic with the ammonia that forms an adduct[54]. This adduct reacts with others to form a circular species that decomposes above the surface of the substrate such that the decomposition species react on the substrate surface to form the III-N film. The steps in each of these mechanisms are complicated, and a more detailed list of the possible reactions can be found in Refs [55,56].

1.2.1.2 Growth Temperature

Depending on the composition of the material being grown, the growth temperatures may range from 700°C to 1400°C. This plays a key role in determining adatom mobility. If the temperature is not high enough for adatoms to reach the step edge, they will be incorporated at a random location along a terrace. This introduces small islands that can lead to surface roughness or nucleate defects.

Due to the large difference in binding strength between In, Ga, and Al with the substrate, the optimal growth temperature changes significantly for different compositions. A balance is desired between allowing adatom mobility for high quality growth and limiting material desorption for achieving reasonable growth rates. The compositions of high-quality alloys that can be achieved are limited by the relative rates of these factors for the different metals. This is especially an issue for indium containing layers as the onset of indium desorption is significant well below standard GaN growth temperatures[57]. Additionally, the ammonia

cracking efficiency decreases readily with lowering growth temperature due to the large energetic barrier for breaking the N-H bonds. For this reason, InGaN layers are typically grown at as high a temperature as is practical with a large excess of indium to gallium such that the composition is controlled by the growth temperature more than the relative flowrates. As the tendency for the metal reactant to desorb is temperature dependent, a growth regime can be reached where the growth rate is limited by the adatoms leaving the surface. This desorption limited regime is generally not desired for growth but is still often present for one element during alloy growth.

The desorption not only affects the metal atoms but also impacts impurity formation. Carbon incorporation from organic sidechains remaining attached to the metal atoms decreases with increasing temperature[58]. Hydrogen and oxygen incorporation follow a similar trend[59]. However, increasing the temperature too high may introduce excessive vacancy type point defect formation.

Thus, the growth temperature is an important design consideration impacting the composition, growth quality, and growth rate.

1.2.2 Band Structure

In addition to the physical growth of the crystals, the unique properties of the electronic band structure in the III-N system make it attractive for optoelectronic device fabrication and must be considered. III-N semiconductors have a direct gap, which means that both the conduction band minima and the valence band maxima occur at the same reciprocal space point, as seen in Figure 1-9(a). A direct gap is necessary for efficient radiative recombination as a phonon is not necessary for recombination, as in the case of an indirect gap semiconductor. The bandgap

changes drastically between the different binary alloys, resulting a in a large accessible wavelength range.

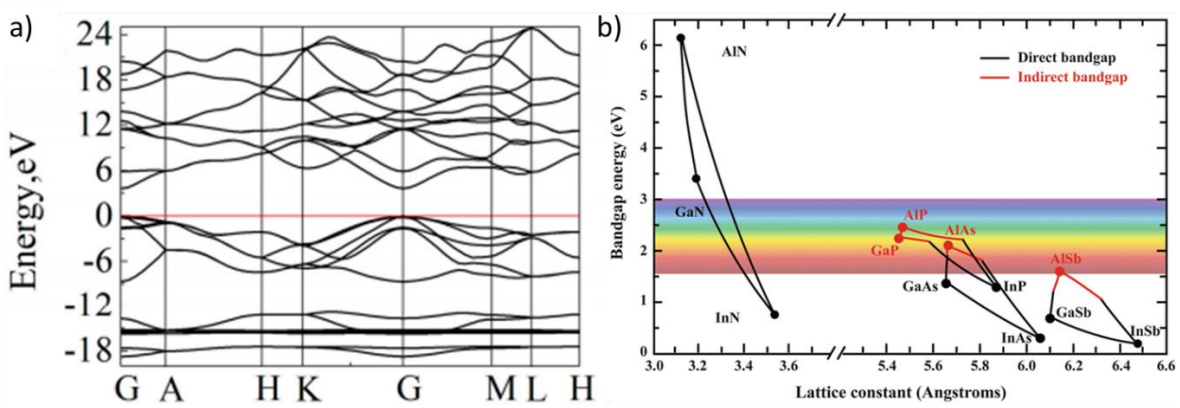

Figure 1-9 Shows the band diagram of GaN (a) and the band gap as a function of lattice parameter (b), corresponding to different compositions, shows the wide wavelength range that is accessible with the III-N system[60,61].

An electronic device's band diagram is not only affected by the band gap but is also affected by internal fields due to the material properties. The asymmetry of the group III and nitrogen atomic locations produces a polarization field along the [0001] (c-direction) due to the high electronegativity of the nitrogen atom, creating a strong dipole[62]. A second electric field is produced from the piezoelectric polarization due to the strain state of the active region. For an InGaN/GaN optoelectronic device, the In content of the active region affects its equilibrium lattice constant. Thus, as the In content increases, the piezoelectric polarization increases and generally dominates the dipole polarization due to the ~11% lattice mismatch between InN and GaN[63]. The total field is determined by the sum of the piezoelectric polarization and the spontaneous polarization. The quantum confined Stark effect (QCSE) results in band bending along the c-plane and separates the electron-hole wave functions as seen in Figure 1-10. This reduces the effective band gap for the QW, decreases the radiative recombination efficiency, reduces gain, and affects carrier injection. Since this field is in the c-direction, growth along a

non-polar plane would result in no polarization along the growth direction, and thus elimination of the band bending along the direction of interest.

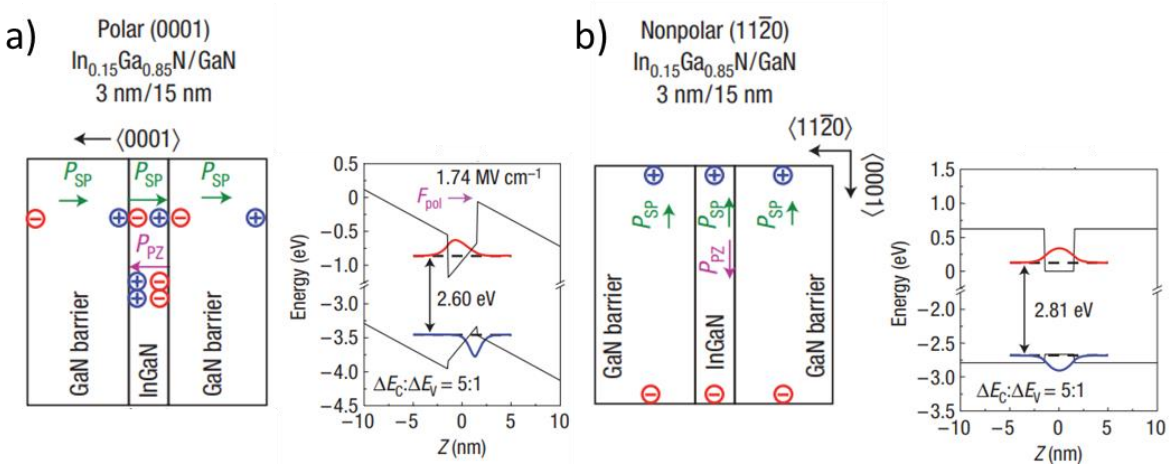

Figure 1-10. Shows the polarization fields and their effect on the band bending and wavefunction overlap in a c-plane (a) and m-plane (b) device. The direction of the field in the m-plane sample does not cause the band bending seen in the c-plane one[64]. Reprinted by permission from Springer Nature ©2006.

1.2.3 Non-Basal Orientations

Most uses of GaN are based on its c-plane orientation due to the relative ease of forming substrates. However, other crystal planes offer a number of advantages that may make it worth the increased cost in high performance devices, such as lasers. The primary differences between the planes are the changes in the internal electric fields, in the valence band structure, and in the growth considerations. A brief look into these effects is discussed below which will lead to the decision to use $(20\bar{2}\bar{1})$ for the semipolar VCSELs presented later.

1.2.3.1 Polarization Fields

An advantage to non-basal planes that was key in initially garnering interest is the reduction or elimination of polarization fields[65]. This has a significant effect on LEDs as it allows for more stable operation with less efficiency droop. As seen in Figure 1-11, the total polarization charge decreases as the inclination angle increases from (0001), until it becomes negative at

45° and then returns to zero at the non-polar planes at 90° [66]. In a diode (such as in a LED) there is a built-in field, that, for the case of a p-up device, points in the "negative" direction relative to the polarization shown in Figure 1-11. This means that it is against the polarization field in $(20\bar{2}\bar{1})$ and nearly cancels out to give a fairly flat band structure[67]. Nonpolar orientations lack the polarization fields across the QWs and have a nearly flat band as well. Having flat bands in the quantum wells increases the electron-hole wave function overlap, which increases the recombination efficiency. This allows for larger wells to be used to decrease the carrier density at a set injection current. Both effects reduce the efficiency droop in LEDs. This also has an improvement for laser performance. The improved overlap gives a larger optical matrix element and increases the gain, as will be discussed below. Using larger wells is a way to increase the confinement factor of the active region, without increasing the number of wells and potentially introducing carrier injection issues. However, this comes at the expense of reducing the gain as it is inversely related to the QW width. Thus, the modal gain remains relatively constant and the overall effect is a reduction the effect of auger recombination.

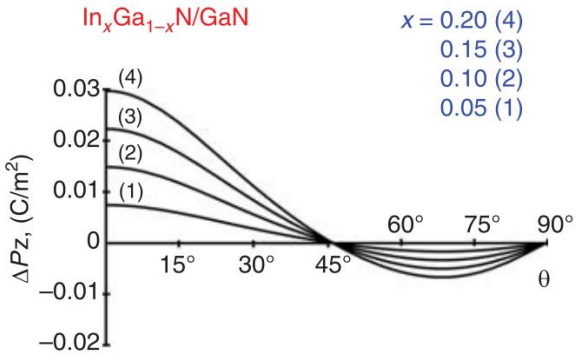

Figure 1-11 Shows how the polarization charge changes with inclination angle[65].

An additional effect of flat bands is that the wavelength is more stable with changing injection[67]. When the wells are tilted, the recombination emission is redshifted relative to the

standard bandgap emission. As the injection increases, the injected carriers screen the fields and flatten the bands. This results in a blueshifting of the emission as the devices are pumped harder, which is not seen in structures that begin with flat bands. However, the flat band condition does not provide an inherent redshift. Thus, to reach the same emission wavelength at low current injections, the quantum wells must have a higher indium composition. Finally, the reduction in the band bending lowers or eliminates the potential barrier at the edge of the QWs, improving hole injection[51]. At the high current densities that are used for laser operation, many of these effects are minimized and the impact of the polarization fields is small.

1.2.3.2 Valence Band Structure

The most significant advantages of using non-basal orientations for lasers comes from the changes in the valence band structure. As can be seen in Figure 1-12, anisotropic biaxial strain in the QWs leads to a splitting of the valence bands and a change in the hole effective mass[68]. As the conduction band is an s-like state with spherical symmetry, the polarization of light emitted during recombination is determined by the valence band character. The splitting breaks the degeneracy on the polarization dependence of recombination, where recombination with the A1 band leads to light that is polarized parallel to the a-direction and the B1 band produces light parallel to the projection of the c-axis[69]. Energetically, the holes want to be in the topmost valence band, with thermal distributions causing some percentage to be in the lower bands. Thus, the majority of the recombination occurs with the A1 subband leading to a total emission that is mostly polarized parallel to the a-direction, with the amount of polarization being determined by the energy difference in the band splitting. The polarization ratio (p) from a $(20\bar{2}\bar{1})$ device is given by:

$$p = \frac{(I_{[\bar{1}2\bar{1}0]} - I_{[\bar{1}01\bar{4}]})}{(I_{[\bar{1}2\bar{1}0]} + I_{[\bar{1}01\bar{4}]})}, \qquad \text{Eq. 1-1}$$

where I is the integrated intensity of a certain polarization. $[\bar{1}01\bar{4}]$ is the projection of the c-axis along the $(20\bar{2}\,\bar{1})$ surface and would be replaced with the c-parallel projection for finding the polarization on another plane of interest. The polarization ratio has been shown to be relatively independent of bias, and therefore independent in changes of the polarization field[69]. However, changing the indium content of the active region affects the anisotropic strain such that the polarization ratio increases significantly with emission wavelength. This preferential polarization in the spontaneous emission leads to significant polarization of the stimulated emission characteristics such that lasers on non-basal planes naturally emit fully polarized beams with a well-defined polarization angle. For VCSELs that are fabricated in 2D arrays, this means that all the devices are polarization locked in the same direction; a direction that is defined by the crystal orientation. This is highly advantageous for applications that rely on the polarization of the light source.

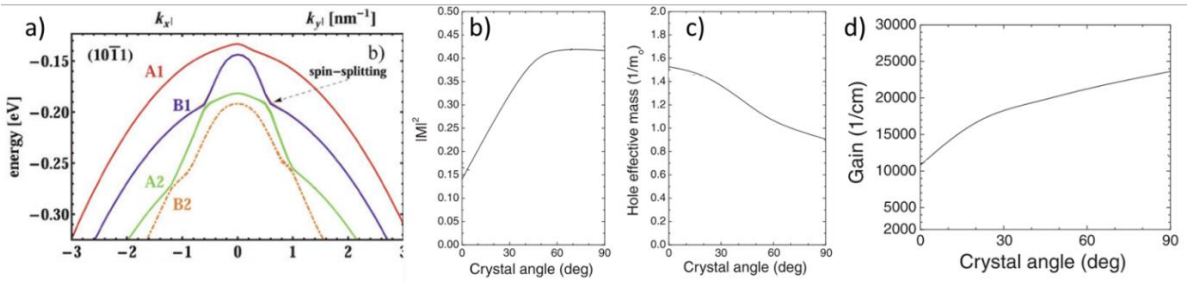

Figure 1-12 (a) Shows the valence band for semipolar $(10\bar{1}1)$ [70]. Copyright Wiley-VCH GmbH. Reproduced with permission. The matrix element (b), hole effective mass (c), and gain (d) change with inclination angle. The calculations assume a 3 nm wide $In_{0.15}Ga_{0.85}N$ QW and 2×10^{13} cm^{-2} carrier concentration[71]. Copyright 2003 The Japan Society of Applied Physics

The shape of the valence band changes with inclination angle, affecting both the density of states and the hole effective mass. The change in the density of states leads to a lower transparence carrier density as the inclination angle increases[51,71,72]. The decrease of the hole

effective mass increases the quasi-fermi level separation under operation, which increases the gain, as seen in Figure 1-12 (d). Simulations suggest that the increase of the optical matrix element due to the reduction in the polarization fields occurs up to an inclination angle of 60° before the benefit begins to saturate[71]. As the full gain curve continues to steadily increase even beyond that point, it can be concluded that the primary driving force behind the improved gain at higher inclination angles is the reduction in the hole effective mass. This increase in gain not only provides a lower threshold, but also a higher modulation bandwidth for faster communication[51].

A final point to be made is that the band structure can be significantly affected by alloy and well width fluctuations, as well as interface roughness[68]. Thus, the actual growth of the wells on these planes can also drastically affect the band splitting effects, such as the polarization ratio that is measured from devices on non-basal planes. Practically, it has been shown with different planes that have the same theoretical band structure, $(20\bar{2}\,\bar{1})$ and $(20\bar{2}1)$, that they have different experimental polarization ratios[69]. The lower polarization ratio seen on $(20\bar{2}1)$ is attributed to fluctuations in the QW width and composition. The difference in polarization ratio was taken further to include the optical gain to suggest that the higher measured band splitting on $(20\bar{2}\,\bar{1})$ would lead to higher optical gain. Thus, the theoretical increase in the gain curve with inclination angle may not be experimentally realized for certain orientations without adequate growth control.

1.2.3.3 Emission Wavelength

In addition to the value of gain achievable, the available wavelengths are also affected by the polarization. The shift of the wavefunctions due to the net polarization field can increase the wavelength without increasing the material strain but reduces the recombination efficiency and

leads to a changing wavelength at different drive currents. Thus, it is desired to control the wavelength through material composition only, if this can be achieved. Due to the different surface energetics on different planes driven by varying strain states and atomic configurations, the rate of indium desorption changes, therefore changing the indium incorporation rate[73]. This causes a wide variance in indium uptake across growth planes at the same growth temperature. The semipolar planes of $(11\bar{2}2)$, $(20\bar{2}\bar{1})$, $(10\bar{1}1)$, and $(30\bar{3}\bar{1})$ exhibit the highest indium uptake, whereas m-plane has been experimentally and theoretically shown to have the lowest indium incorporation[51,73].

This variation in indium incorporation affects the emission wavelength in two important ways: by changing the base band gap and the strain state. As the indium composition is increased the strain is increased. The orientation affects the symmetry of the strain which impacts the intermixing of different hole subbands such that for a set indium composition the band gap decreases with inclination angle up to 38°, where it then increases to give m-plane the largest band gap[73].

In addition to the total indium incorporation, the indium uniformity across a wafer is also dependent on the orientation. Carriers tend to localize in areas of high indium concentration that form potential wells in the lateral potential landscape[51]. Thus, the emission wavelength may be redshifted relative to the average indium composition due to the higher proportion of recombination occurring at areas of locally increased indium composition. This allows for longer wavelengths to be reached and potentially draws carriers away from high energy defects. However, it also leads to broadening of the emission spectra. Additionally, high carrier concentrations promote Auger recombination, enhancing droop in LEDs and further degrading performance in high threshold lasers. Finally, the indium composition affects the growth rate.

Thus, as the indium composition changes across the sample, the well width changes. This further increases the full width at half maximum (FWHM) of the emission spectra. While $(20\bar{2}\,\bar{1})$ has been shown to be grown with relatively uniform composition, $(10\,\bar{1}0)$, $(20\bar{2}1)$,and $(11\bar{2}2)$ have proved difficult to reduce indium fluctuations[51,67].

A concern associated with growing high indium containing layers on non-basal orientations is the potential for producing misfit dislocations and basal-plane stacking faults that are not significant issues on c-plane. These defects are non-radiative recombination centers and can facilitate leakage currents. The formation of these defects is plane dependent, but also heavily affected by the growth conditions. The formation of stacking faults is of particular concern on m-plane[51,72]. Thus, m-plane has the poorest indium uptake, preference for forming basal plane stacking faults which reduces the growth process window, and the largest bandgap for a given indium incorporation, thereby severely limiting the achievable wavelengths and motivating the use of a semipolar plane.

Now that the effects of the inclination angle have been presented, the potential planes of interest are considered. The main semipolar planes that have been investigated are $(11\bar{2}2)$, $(10\bar{1}2)$, $(10\bar{1}1)$, $(20\bar{2}1)$, $(30\bar{3}\,\bar{1})$, $(20\bar{2}\,\bar{1})$, and $(10\,\bar{1}\,\bar{1})$, with m-plane being the main non-polar plane of interest. Most of the investigated planes are less than 30° inclined from m-plane, likely due to the lower polarization fields for those orientations[72]. While m-plane has no polarization fields, the highest theoretical gain, the lowest transparency carrier density, and the highest polarization ratio, the limited indium uptake results in degraded performance as the wavelength is pushed much past blue-violet. In the interest of increasing the wavelength of the VCSELs at UCSB, it was decided that a semipolar VCSEL would be optimal. Blue LEDs grown on the different planes showed the best performance for planes that were slightly inclined towards the

n-face, $(20\bar{2}\bar{1})$ and $(30\bar{3}\bar{1})$ [72]. $(20\bar{2}\bar{1})$ has shown good results in both wavelength stability and narrow spectral width and has a good background of research. Thus, it was chosen as the optimal plane for growing the VCSELs.

1.3 M-plane VCSELs at UCSB

Before moving into an in-depth look at VCSEL design considerations, the VCSELs from UCSB that were state-of-the-art at the beginning of this thesis will be presented. This will continue building the context from which the results stem.

1.3.1 Previous UCSB Designs

At UCSB, the first electrically injected VCSEL was demonstrated on m-plane GaN by Holder et al. in 2012[74]. M-plane was used due to the potential for lowering the threshold relative to c-plane and for the ability to produce polarization locked arrays. The VCSELs fabricated at UCSB contain a dual dielectric structure and use photoelectrochemical (PEC) etching for substrate removal. PEC etching allows for precise cavity length control and is discussed in more depth in section 3.2.1. The initial demonstration of an m-plane VCSEL used a SiN_x defined aperture and an ITO based current spreader. The peak output power was 19.5 μW from the device with a threshold current of 70 mA and a 7.5λ cavity length. The high threshold current was attributed to high optical loss in the cavity and contributed to the low total output power. It was found that below threshold the polarization ratio towards the a-direction was 0.13 and reached a peak value of 0.72 after lasing. The low polarization ratio relative to theory, was due to the large amount of unpolarized spontaneous emission that impacted the measurement. However, they were able to demonstrate that all devices that were tested were polarization locked in the same direction. In the next demonstration of m-plane VCSELs,

Holder et al. were able to eliminate the impact of the spontaneous emission and measure a polarization ratio of 100%[75].

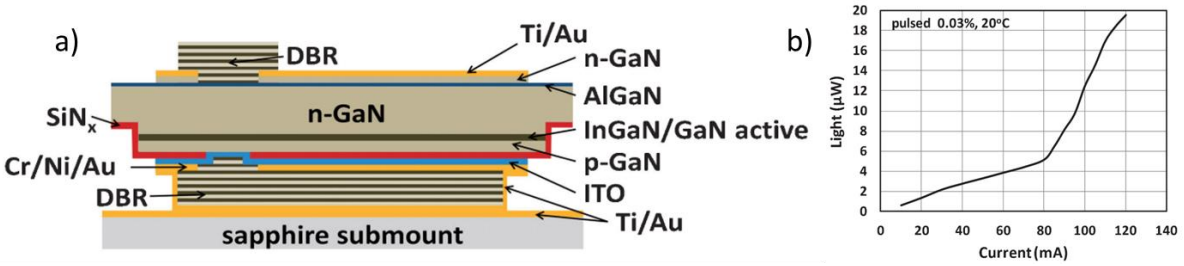

Figure 1-13 Schematic of the first m-plane VCSEL (a) and its LIV characteristics (b) under pulsed operation[74]. Copyright 2012 The Japan Society of Applied Physics

Over time improvements were made and the device design changed such that threshold current densities as low as 3.5 kA/cm^2 and peak output powers of 550 μW were achieved, though all under pulsed operation[76]. In 2018 Forman et al. demonstrated the first CW operation of an m-plane VCSEL[77]. The device used an aluminum ion implant defined aperture and an MBE grown tunnel junction contact, but otherwise had a similar general design to the original m-plane VCSELs. Aside from the design, a long 23 λ cavity length was used to improve the thermal performance. Shorter cavities have been shown to have a higher differential efficiency and wider mode spacing but lower tolerance for cavity length distortions/variations[78]. COMSOL simulations suggested that extending the cavity thickness from 7λ led to a reduction in the thermal impedance from 2750 K/W to 1500 K/W[77]. In addition to lower thermal impedance, longer cavities have a shorter lateral mode spacing, which means that longer cavities can better maintain good alignment of the gain curve with a resonance mode as the gain peak is thermally shifted. Thus, the effects of thermal inhomogeneity across an array can be lowered by having a longer cavity length. This enabled CW operation of a 6 μm device with a threshold current of 10 mA (35 kA/cm^2) and a peak output power of 145 μW. Under pulsed operation the same device had a threshold of 12 mA (42 kA/cm2) and a peak power of 700

μW. The fundamental mode was observed up to 2.5×Ith before a second lobe appeared. The high threshold current was attributed to the lower differential gain of the large QWs used and the low confinement factor due to the long cavity. It is important to also note that the diffraction loss increases with cavity length. Thus, as an increasing cavity length has been shown to increase the threshold due to the decrease in the confinement factor and increase in the round trip loss[79], using a shorter cavity would be beneficial for device performance if thermal improvements are not required for CW operation. Additionally, having a shorter effective length increases the mirror loss, thereby increasing the expected differential efficiency at the expense of some additional loss.

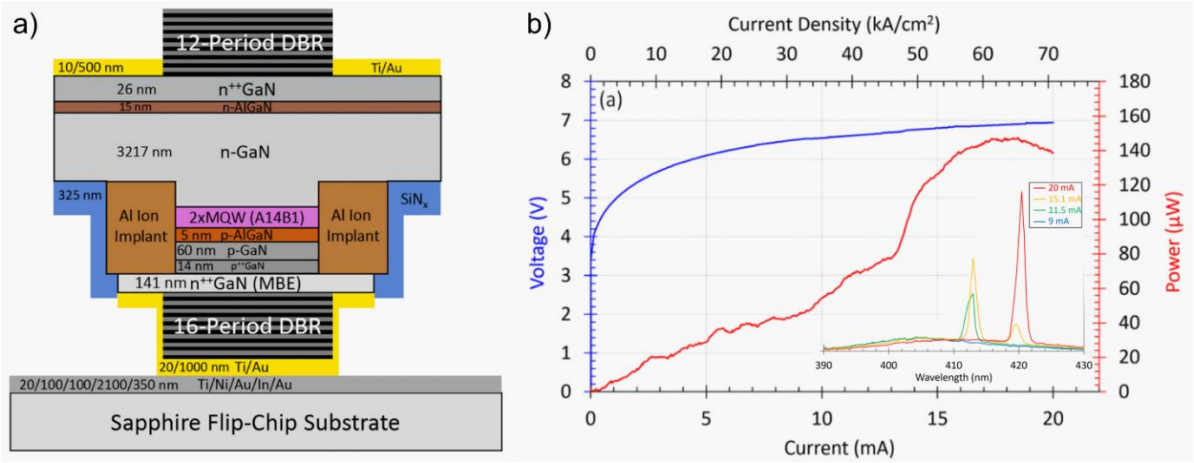

Figure 1-14 Schematic of the first CW m-plane VCSEL (a) with its LIV (b) and emission spectra (inset) under CW operation. Reprinted from Ref 77, with the permission of AIP Publishing.

It was noted that the differential efficiency increased with increasing current when the dominant mode shifted to a longer wavelength. This was partially attributed to the longer wavelength having lower material absorption in the cavity, lower scattering loss, and a reduced DBR reflectivity. While these effects didn't account for the full change in the differential efficiency, it does highlight that moving to a longer wavelength could provide improvements to device performance. Unfortunately, the indium uptake of m-plane is much smaller than

many other orientations, so switching to another plane may be required to reach the longer wavelengths[80].

The effect of scattering loss was highlighted with the 2 nm RMS roughness from the MBE grown TJ introducing an estimated 27 cm^{-1} of loss[77]. While this large roughness heavily increased the loss, the device was able to operate near threshold at ~ 1.4 V lower than the previously demonstrated ITO based VCSELs. Thus, this optimized TJ showed dramatic improvements relative to previous iterations of MBE tunnel junctions. However, the loss due to roughness suggests that a smoother intracavity contact is necessary for improving the device performance. This could be achieved by using an MOCVD grown TJ. The results from this device motivated the fabrication of a longer wavelength, semipolar VCSEL with a smooth MOCVD growth TJ.

2 Nitride VCSEL Design

Now that an overview of the III-N material system and a couple UCSB device designs have been presented, the concepts can be applied to a more detailed consideration of III-N VCSELs. For additional background information on laser physics, see Appendix A.1. The first continuous-wave (CW) operation of a GaN-based VCSEL was in 2008 when Lu et al. achieved lasing at 77K[81]. Since then, research has progressed extensively such that room temperature CW operation of VCSELs has been achieved on multiple planes of GaN, with wavelengths ranging from near UV to green[82–84]. The threshold current densities of these devices range from 0.64 kA/cm^2 to 141 kA/cm^2 [85–88], with the peak power of a single device ranging from 3 μW up to 23.7 mW[89–92]. Typically, III-N VCSELs are grown on freestanding GaN substrates as growth on sapphire substrates has been shown to increase the rollover, decrease the output power, and significantly decrease device lifetime[93]. The main difficulties associated with fabricating III-N VCSELs are the difficulty in forming an epitaxial distributed Bragg reflector, the low conductivity of p-type GaN, obtaining sufficient current confinement, and controlling the beam profile. Multiple approaches have been taken to address each of these issues and a brief summary of them is presented here.

2.1 Device Geometry

There are two main structures for GaN-based VCSELs that are primarily based on the DBR configuration: hybrid and dual dielectric. The primary consideration between these designs involves a tradeoff between growth and processing complexity, though they can also play an important role in the thermal performance of the device. The effect of operating temperature will be briefly discussed to demonstrate the importance of this aspect.

2.1.1 Thermal effects

Many device properties are temperature dependent and overall lead to a roll over in the power-current curve, shown in Figure 2-1(a), at higher operating conditions. This rollover is often primarily due to increased carrier leakage at elevated temperatures, but it can also be heavily affected by the overlap of the mode with the gain spectra. As the operating temperature increases, the gain curve tends to decrease and redshift, as shown in Figure 2-1(b) for GaAs based lasers. The reduction of the gain curve means that the device must be pumped harder for the gain to cancel out the loss. Additionally, as the gain redshifts it changes the position of the mode relative to the gain spectra. If the mode is originally aligned with the peak of the gain spectra, then the alignment will decrease with heating. The mode itself changes with temperature due to the temperature dependence of the refractive index changing the total optical cavity length. This further increases the required pump power for lasing. Finally, the increase in temperature reduces the differential gain, decreasing the potential modulation response of the device.

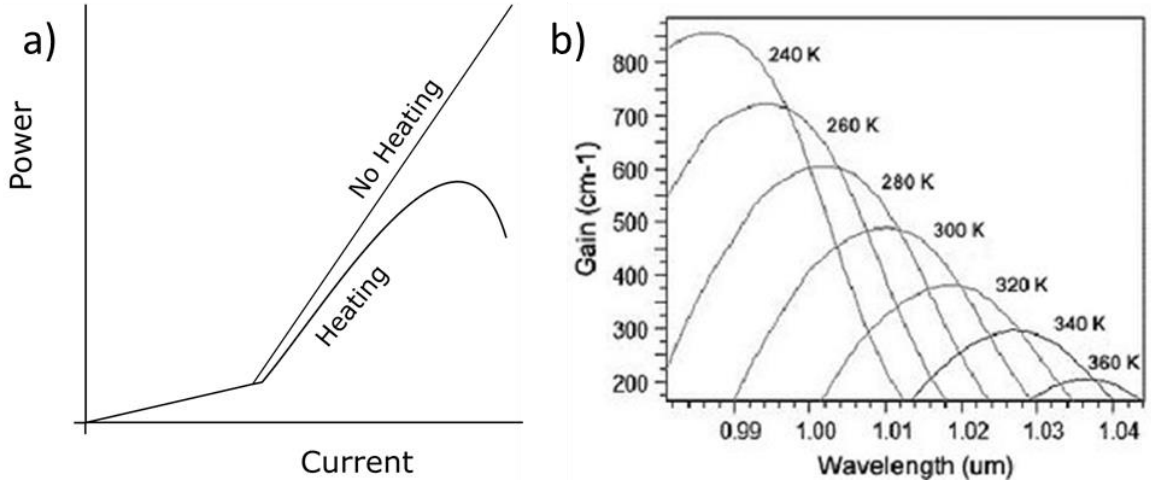

Figure 2-1 The LI curves (a) show the effect of adding thermal effects to the roll over. The gain curves as a function of wavelength (b) decrease and redshift as the temperature is increased[94].

The temperature of a device changes under operation due to several heat sources, such as joule heating, non-radiative recombination, Peltier heating, and Thomson heating. As with many processes, the excess power is dissipated as heat. At threshold the output power is expected to be very low, and thus the dissipated power, P_D, in the device can nearly be described by the total input power, P_{in}.

$$P_{D,th} \approx P_{in} = I_{th}V_{th} \qquad \text{Eq. 2-1}$$

The thermal impedance, Z_T, can then be used to calculate the temperature rise

$$\Delta T = P_D Z_T \qquad \text{Eq. 2-2}$$

The thermal impedance is heavily influenced by the geometry of the device in addition to the thermal conductivities of the layers. It has been shown that for flip-chip device designs, as will be discussed later, increasing the cavity length, reducing the bottom DBR diameter, choosing an appropriate submount, and increasing the mesa size can all improve thermal performance to a certain extent[95,96]. The thermal impedance can be measured experimentally by finding the shift in the emission spectra as a function of stage temperature and input power.

$$Z_t = \left(\frac{d\lambda}{dP}\right)_T \Big/ \left(\frac{d\lambda}{dT}\right)_P \qquad \text{Eq. 2-3}$$

Thus, self-heating increases the percentage of carriers that escape the active region. This results in a higher threshold current to reach the same carrier density in the quantum wells and leads to a reduced differential efficiency. In addition to just the carrier density, the material gain and the internal loss are affected by the temperature such that an exponential dependence on temperature is often observed.

To limit the effect of heating, devices can be operated under pulsed conditions; however, even under pulsed operation the power will eventually rollover due to the transient heating in

the pulse and/or spatial hole burning. Ideally, the pulses are long in terms of the optical response time, but short compared to the thermal response time. E.g. They are long enough that the device is lasing during most of the pulse but not so long that the temperature has increased much. This can be difficult experimentally as there is a rise and fall time for each pulse. As the pulses get shorter, the proportion of the pulse that is transient increases. Also, oscillations are often observed in the pulse after a transition, further increasing the time before it is stable at the desired pump parameters. In addition to the pulse width, the dead time between pulses should be long enough that the device can return back to room temperature. As the total thermal resistance of the device tends to increase with drive current, eventually the temperature increase over the pulse will become significant enough to limit the output power.

Regardless of device design, one common way to reduce the thermal impedance is to increase the cavity length. COMSOL simulations, shown in Figure 2-2, depict the importance of cavity length control in thermal performance

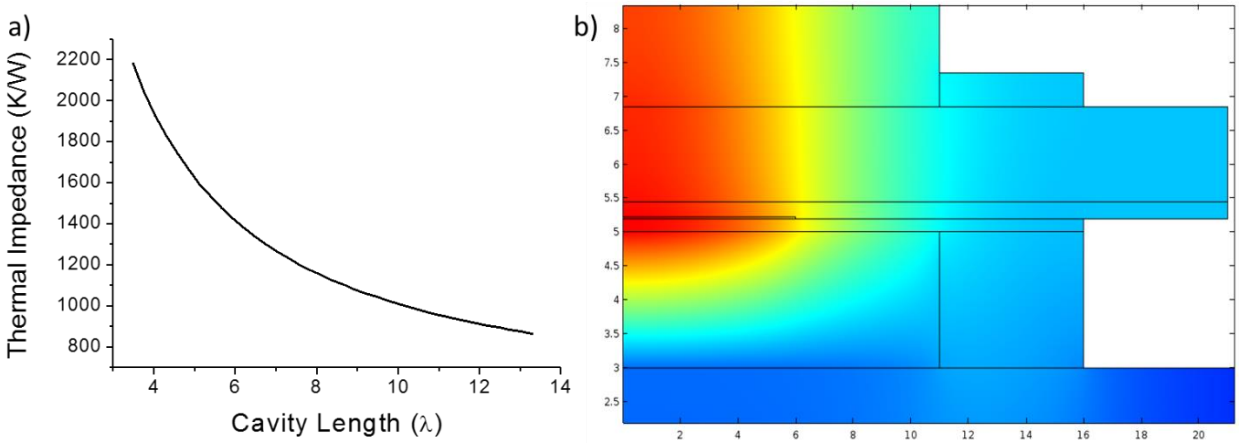

Figure 2-2. Shows the effect of the epitaxial cavity length on the total thermal impedance for a device (a). The temperature profile of a 10λ device (b) shows that most of the heat is concentrated in the aperture area. The IIA device structure is presented later and is similar to the m-plane devices presented above.

2.1.2 DBR Design

Traditionally, hybrid VCSELs utilize a bottom epitaxial DBR, consisting of either AlN/GaN or AlInN/GaN bilayers, and a dielectric DBR on the topside. The dual dielectric design, as its name implies, uses a dielectric based DBR on either side of the cavity. The main considerations in choosing a DBR design involves the ease of fabrication, the DBR reflectivity spectrum, and the DBR conductivity. Using epitaxial DBRs generally allows for easier fabrication and has better potential for thermal and electrical conductivity but requires many more periods for a comparable reflectivity and has smaller stopbands. For both styles of DBR, their advantages are not always seen in practice.

2.1.2.1 Hybrid DBR Design

The hybrid DBR structure emulates some aspects of typical GaAs based VCSELs which often use at least one epitaxially grown AlAs/GaAs DBR. This allows some advantages in ease of processing and improved electrical and thermal control. Directly applying the arsenide-based approach would suggest using an AlN/GaN epitaxial DBR. However, there are several limitations when using the nitride system. First of all, the limited difference in refractive index of the two nitride layers leads to a relatively small stopband shown in Figure 2-3[97]. By having a smaller stopband, there is a tighter tolerance for growth and processing variations that would shift the lasing wavelength. Additionally, a large number of layers are needed for the required reflectance, and the lattice mismatch between AlN and GaN can lead to crystal quality issues. This version of a hybrid DBR structure was used by Lu et al. in their demonstration of CW lasing in 2008 to produce a device with a threshold current of 1.4 mA at 77K[98]. To deal with the lattice mismatch and difference in thermal expansion coefficients that threatened to crack the AlN/GaN DBRs a 5.5 pair AlN/GaN superlattice was inserted between every four DBR

periods. The superlattice was designed to be a half wave thick to be "optically invisible" and acts to reduce the tensile strain in the epitaxial layers. While this allowed the device to lase, it only had a spectral bandwidth of 25 nm and likely took a very long time to grow the large number of layers required.

Although both GaN and AlN have relatively high thermal conductivity, the large number of interfaces in this DBR design significantly reduces the thermal advantage of using these materials. While using an epitaxial DBR provides the potential for electrical injection through the DBR, it is quite difficult and, as far as I am aware, has not been successfully demonstrated with an AlN/GaN DBR.

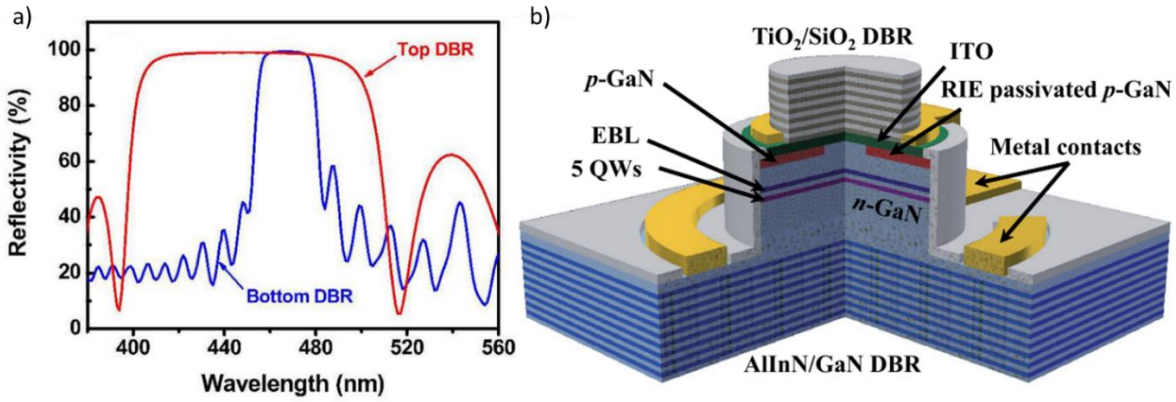

Figure 2-3 The reflectivity spectrum of a hybrid DBR (a) shows a much shorter stopband than that shown for the dielectric DBR[99] ©2009. (b) Shows a schematic of a hybrid VCSEL with an AlInN/GaN DBR. Reprinted from Ref 87, with the permission of AIP Publishing.

An alternative method that reduces the strain in the DBR, is to use AlInN that is lattice matched to GaN. However, the refractive index difference of these two layers is even smaller than that for AlN and GaN, so more layers are required, and the stopband is even shorter. Additionally, AlInN grows very slowly, on the order of 0.5um/hr, which means growth is expensive and time consuming[100]. Cosendey et al. initially demonstrated a VCSEL with this approach in 2012 which had a threshold current of 70 mA and a peak output power of ~325 μW[87]. Electrical injection through this style of DBR has been achieved by Muranaga et al. in

2019 producing a VCSEL with a differential resistance of 90 Ω[101]. Unfortunately, the AlInN has significant alloy scattering, which severely limits its thermal conductivity. This led Muranaga et al.'s demonstration of a 1.5λ cavity to have a very large thermal resistance of 2700 K/W. Finally, the short stopband of this type of DBR means that reactor drift of 1% can cause significant shifts in the reflectivity at the cavity mode when it is misaligned[101]. Despite the challenges of controlling the growth of this type of DBR, it has been used to fabricate some of the highest power VCSELs to date[91].

A final type of epitaxial DBR to be discussed here is a nanoporous GaN DBR. It has been shown that through electrochemical etching, GaN can be porousified, where the pore size and density are controlled by the doping in the GaN, the applied voltage during the etch, the concentration of the reactant, and the temperature[102–104]. Selective doping of GaN layers can produce alternating layers of porous and non-porous GaN that can act as a DBR due to the effective index difference of those layers. While this method adds several processing steps, due to having to etch below the DBR and laterally porosify under the device, it counteracts the main drawback of epitaxial DBRs, namely the small stopband and low reflectivity. Mishkat-Ul-Masabih et al. demonstrated a VCSEL with this type of DBR on m-plane GaN in 2019 that had a peak output power of 1.5 mW and a threshold current density of 20 kA/cm^2 [105]. They concluded that since all devices tested were uniformly polarized with a high polarization ratio, that there was no significant optical scattering from using a nanoporous DBR. Using a nanoporous DBR also has the potential for allowing high thermal and electrical conductivity, though that was not explored in this initial demonstration.

2.1.2.2 Dual Dielectric DBR Design

As an alternative, the dual dielectric DBR design can be implemented. It may increase the processing complexity but also increases the tolerance for process variability and reduces the growth complexity. While this DBR configuration avoids the growth difficulties, it generally requires flip chip bonding and removal of the substrate[106]. A number of techniques for removing the substrate have been demonstrated, including laser lift off, chemical mechanical polishing (CMP), and selective undercut etching[74,85,107]. Use of laser lift off and chemical mechanical polishing has shown issues with obtaining thickness uniformity and control[93]. Additionally, dielectric DBRs suffer from very low thermal conductivity, necessitating the addition of alternative thermal paths to the heatsink.

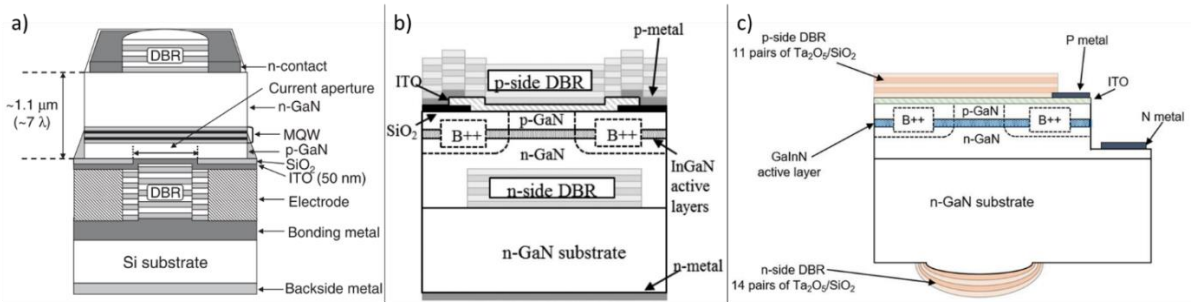

Figure 2-4 Shows device schematics for dual dielectric VCSELs with flip chip bonding substrate removal(a), epitaxial lateral overgrowth (b), and a curved back mirror (c)[107–109]. Copyright 2008 The Japan Society of Applied Physics. Copyright Wiley-VCH GmbH. Reproduced with permission. Copyright (2019) The Japan Society of Applied Physics

Shortly after Lu et al. demonstrated their hybrid VCSEL structure in 2008, Higuchi et al. showed a flip-chip dual dielectric DBR design that had a threshold current of 7 mA, a peak output power of 140 μW, and lased CW at room temperature[107]. In this case the device was grown on a sapphire substrate and laser lift-off was performed to remove the substrate followed by CMP to get the desired cavity thickness. The flip-chip dual dielectric design has been the primary method for VCSEL fabrication at UCSB, although the substrate has been removed by

a selective photoelectrochemical (PEC) etch of a sacrificial layer which negates the need for CMP. Holder et al, first demonstrated a VCSEL with this structure in 2012 on m-plane GaN[74].

Two alternative methods have been demonstrated by Sony that do not require substrate removal. The first approach uses epitaxial lateral overgrowth (ELO) over a deposited dielectric DBR to avoid flip-chip bonding and removing the substrate[108,110]. In 2015 Izumi et al. deposited SiO_2/SiN_x DBRs on a freestanding GaN substrate and using ELO grew 4 μm of GaN above the DBR before growing the VCSEL structure to define the cavity. A SiO_2/Ta_2O_5 dielectric DBR was deposited on top of the device to form the resonator before the GaN substrate was thinned. Depositing the n-contact on the back of the substrate made the whole device processing fairly simple and made the advantages of an electrically conducting DBR redundant. In the end, the device had a threshold current density of 16 kA/cm^2, and a peak output power of 0.9 mW[110]. By having highly thermally conductive n-GaN to surround the DBR, the device was able to efficiently dissipate heat and bypass the negative effects of the low dielectric thermal conductivity.

One issue with the ELO structure is the diffraction loss. For a resonator with two planar mirrors, the diffraction loss increases with cavity length. Thus, the thick n-GaN that covered the DBR and gave the good thermal performance, also increased the loss in the VCSEL. To address this, Hamaguchi et al. moved to using one curved mirror to focus the beam back on the other planar mirror[86]. This, however, was not achieved with ELO. Instead, curved lenses were etched into the backside of the substrate after polishing. DBRs were deposited on these curved lenses to form the curved mirrors. First demonstrated in early 2018, the device had a threshold current density of 141 kA/cm^2. However, by 2019 some modifications were made to the structure that allowed the threshold current to be as low as 0.25 mA[109]. Putting the mirror

on the backside effectively removes the negative effects of the low thermal conductivity of the dielectric DBR, in addition to eliminating the need for substrate removal. One consequence of having such a long cavity is that the mode spacing becomes very small. This allows for a high peak output power as there continues to be a mode that aligns well with the gain, even as it heats during operation. Using a dielectric DBR may be important for this sort of application as the wide stopband can maintain a high reflectivity, even as the lasing wavelength shifts with the gain. However, the mode hopping that allows for high power operation, also represents a mode instability that would be unacceptable in certain applications.

2.2 Current spreader

Due to the low conductivity of p-GaN, an intracavity contact is required to act as a current spreading layer. A proper current spreader allows for uniform current injection into the aperture. Without this, the current would crowd certain areas of the aperture, generally the edge, and lead to spatially varying gain. Nonuniform gain promotes lasing of modes that overlap most strongly with the regions of high gain. Thus, current crowding can introduce odd mode behavior that is difficult to predict. Over the operation of the device, the current pathway may change, which would lead to a change in the mode. This instability can be detrimental for applications that are sensitive to the mode shape or wavelength. A final concern is if the current nonuniformity is significant enough that certain regions of the aperture do not reach transparency. This would cause the active region to be absorbing instead of producing gain. Current spreading is commonly achieved by using an indium-tin-oxide (ITO) conductive oxide layer that is placed at the null of the optical mode standing wave to minimize its absorption. As an alternative to ITO, tunnel junction (TJ) based devices have also been fabricated and show an improved threshold current, at the expense of increasing the operating voltage[76].

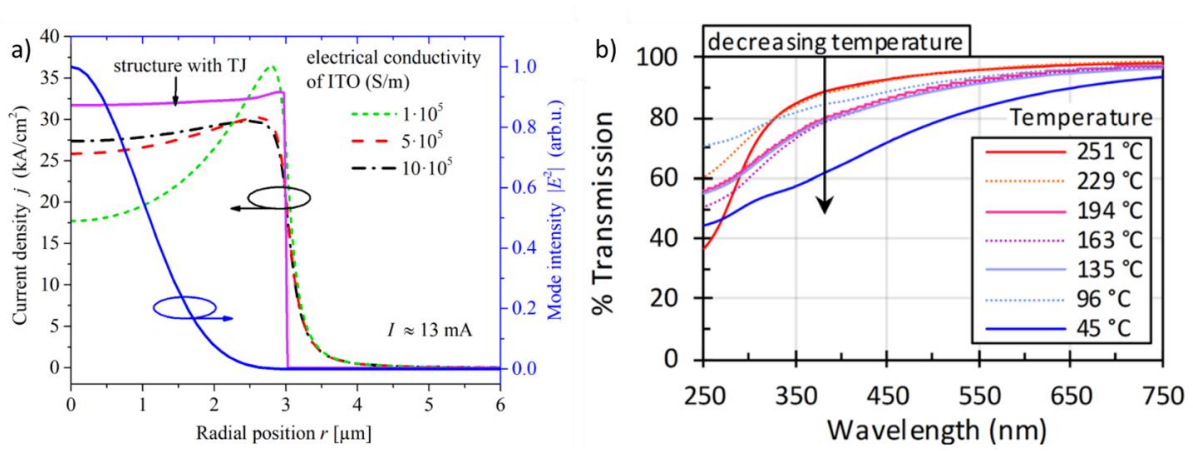

Figure 2-5 Schematic showing the effect of the current spreader conductivity on the current injection profile (a)[111] ©2019 . The profile of the fundamental mode drawn in blue shows poor overlap when the conductivity is low. Higher order modes with a greater intensity nearer the edge of the aperture may see higher gain due to nonuniform electrical injection. The transmission of 18 nm ITO films deposited on DSP sapphire is shown for several deposition temperatures (b). Reprinted from Ref 112, with the permission of AIP Publishing.

2.2.1 Indium-Tin-Oxide

The majority of demonstrations have used ITO as a current spreader due to its ease of deposition and industrial maturity, as it is commonly used in LED production. In the initial electrical injection demonstrated by Lu et al. a 240 nm layer of ITO was used and introduced significant loss[81]. This was quickly addressed by Higuchi et al. in their initial demonstration of the flip-chip structure. They estimated that their 50 nm of ITO introduced an optical loss of about 0.5%[107]. In 2012, Cosendey et al. used a similar thickness in their InAlN/GaN DBR hybrid structure and found that the ITO contributed 0.8% loss[87]. While this may seem small, it is still rather large for a VCSEL. The 0.8% loss, corresponded to an addition of 45 cm^{-1} to the total internal loss, which is nearly double the internal loss from all other sources in that device. They proposed that halving the thickness of the ITO could reduce the internal loss due to the ITO to 2 cm^{-1} if it was perfectly aligned with the null of the standing wave. In optimizing the curved mirror structure, Hamaguchi et al. lists decreasing their ITO thickness from 30 nm to

20 nm as one of the key design changes that enabled CW operation at the low threshold of 0.25 mA[109]. Using 20 nm of ITO, Kuramoto et al were able to demonstrate a 16x16 VCSEL array that emitted nearly 1.2 W of power[27].

Thus, the importance of decreasing the thickness of the ITO to reduce internal loss and improve performance has been shown over the development of III-N VCSELs. However, decreasing the thickness of the ITO impacts the resistance of the device and can limit current spreading to larger aperture devices. This trend of decreasing the thickness of the ITO, even at the expense of the voltage, seems to suggest that the use of a tunnel junction would be necessary for any device with a medium to large aperture size.

2.2.2 Tunnel Junction

A tunnel junction allows hole injection into the p-side of a device through an n-type semiconductor. This is achieved by using a highly doped n-type and a highly doped p-type region under reverse bias such that electrons can tunnel from the valence band of the p-type region to the conduction band of the n-type. As the tunneling probability is exponentially related to the tunneling distance, using highly doped layers to produce a thin depletion width is important for efficient operation. InP based VCSELs, which suffer from similarly poor p-type conductivity, have used tunnel junctions as intracavity contacts to achieve efficient current spreading by allowing thick n-type layers to be placed on both ends of the device. Leonard et al. identified that 74% of their total internal loss could be attributed to their λ/4 ITO current spreader, even when aligned to the null of the standing wave[76]. They fabricated a device with an MBE grown TJ on MOCVD grown base epi layers. MBE was used instead of MOCVD to eliminate hydrogen repassivation of the p-GaN during the TJ growth and to increase the Si doping in the n-GaN. The TJ based device showed a 56% decrease in threshold current density

(from 8 kA/cm^2 to 3.5 kA/cm^2) and an increase of max output power from 80 μW to 550 μW relative to the ITO VCSEL. Despite not seeing an increase in the differential resistance of the device, the TJ did introduce an additional 1.5 V. An additional effect of the MBE tunnel junction was that it increased the epitaxial surface roughness, thereby increasing the scattering loss. This was due to the misorientation in the substrate required for MOCVD growth being suboptimal for MBE growth.

In the interest of reducing the surface roughness, and making tunnel junctions more accessible for industrial production, Lee et al. demonstrated a VCSEL with a tunnel junction grown by MOCVD[113]. Through the introduction of a BHF dip and an in-situ activation procedure before growth, LED test samples with a 1.6 V reduction in voltage relative to samples without the surface treatment were demonstrated. The final VCSEL device had a threshold current density of 10 kA/cm^2, and a peak power out of 319 μW. At low currents, this device had a similar voltage to the MBE grown tunnel junction device, however it did suffer from a nearly double differential resistance.

2.3 Current Confinement

Current confinement defines the optical and electrical aperture for gain guided lasers. This is often achieved through deposition of an insulating layer or damaging the material outside the aperture in one part of the structure. In addition to aperture design, the size of the aperture can also significantly affect the device performance. As the aperture increases, current spreading becomes a greater issue, each aperture requires more current to lase, and heat dissipation becomes a bigger issue[88]. Alternatively, the lateral confinement factor decreases with decreasing aperture size such that the losses begin to increase. Different approaches provide different levels of optical confinement and reliability in keeping the current confined in

different operating regimes. In this section the primary current confinement schemes that have been used in III-N VCSELs are presented.

2.3.1 Dielectric

Depositing an insulating layer, such as SiO_2, outside the aperture is one of the simplest current confinement methods and was used by many of the initial VCSEL demonstrations from different groups[81,88,89,107,108]. However, as discussed by Hashemi et al. increasing the cavity length outside the aperture forms an anti-guiding cavity, increasing the internal loss[114–116]. They used 3D and quasi 2D simulations to estimate the effect of different aperture designs on the threshold gain. They found that a moderately positive index guiding resulted in the lowest threshold requirement. As the positive guiding increased, the diffraction loss also increased; once the cavity became anti-guiding the threshold increased significantly due to optical lateral losses. They suggested that a dielectric aperture could be used if a DBR spacer were introduced above the aperture, or the dielectric layers were planar with the GaN by introducing an additional etch to the processing.

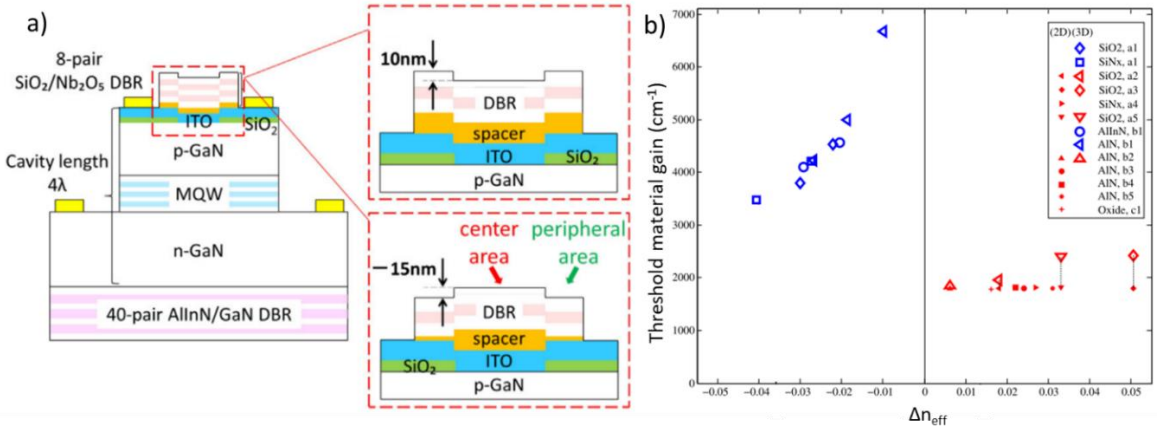

Figure 2-6 Depicts the convex and concave DBRs that are achieved by using a dielectric aperture (a)[117]. Copyright 2018 Wiley-VCH GmbH. Reproduced with permission. (b) shows the effect of the antiguiding cavity on the threshold gain[114]. Copyright 2013 The Japan Society of Applied Physics

Hayashi et al. later fabricated a device with a convex structure by adding a spacer layer in the aperture area of the DBR[117]. They report that moving to the convex structure gave a 1.5% relative refractive index difference for guiding that reduced the threshold current by around 70%. However, the increased guiding introduced multiple higher order modes. Shortly following this, Kuramoto et al. reported a device where the p-GaN was etched outside the aperture such that it was planar after the dielectric was deposited[118]. This "buried dielectric" structure produced an impressive 6 mW of output power, partly due to the 4.7 times higher differential efficiency achieved with the lower loss for a guided cavity. They calculated that the buried dielectric structure had 50 cm^{-1} less loss than the antiguided one. Multimode lasing was also observed in this case as well. Thus, a dielectric aperture may be simple in theory, but it can be difficult to implement without introducing additional loss.

2.3.2 Ion implantation

An alternative type of confinement revolves around damaging the GaN outside the aperture such that it is no longer conductive. This is traditionally done through ion implantation. This method keeps the surface planar and can provide a very slight index guiding. However, it also has the potential to increase the loss in the cavity as the damaged areas tend to have higher absorption values than unimplanted material. Additionally, if the implant heavily impacts the quantum well region, there is the potential for the performance to be affected by the large number of non-radiative recombination centers around the edge of the aperture. However, with the correct implantation conditions, neither of those should be significant issues. Leonard et al. initially demonstrated a VCSEL using aluminum ion implantation for current confinement that showed a 5x decrease in the threshold current density, to 16 kA/cm^2, compared to previous

devices with a dielectric aperture[119]. They reported that the ion implantation reduced the refractive index of the GaN by 2% at 405 nm, giving a slight index guiding to the cavity.

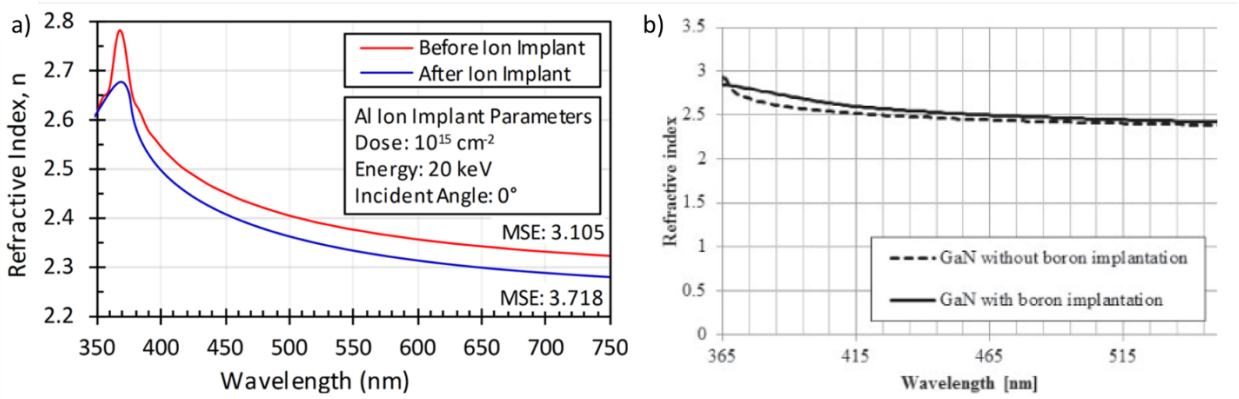

Figure 2-7 Refractive index data for Al ion implantation (a) and B ion implantation (b) as measured by Ellipsometry[78,119]. Copyright 2016 The Japan Society of Applied Physics

Later, Hamaguchi et al. demonstrated current confinement using boron ion passivation of a blue VCSEL[78]. They found that the boron implantation significantly increased the optical absorption and increased the refractive index of the passivated GaN; however, these effects seemed to be negligible for a device with an 8 μm aperture. It was determined that the implant into the active region did not constitute a significant source of nonradiative recombination centers for the aperture sizes tested (>6 μm). This was due to the short diffusion length of carriers in the InGaN QWs.

In evaluating the previous m-plane device performance, the implantation was identified to potentially be introducing significant loss in the cavity due to increased absorption in the damaged material. However, in order to provide effective current confinement, the implanted layer needs to have sufficiently high resistivity to minimize current leakage. By using a structure with a tunnel junction, the implanted area undergoes an anneal when the sample is regrown in either a molecular beam epitaxy (MBE) or MOCVD. At standard growth temperatures, some degree of the ion implant damage will heal, reducing the resistivity of the

layer and ultimately limiting the effectiveness of the region as a current blocking layer. There are several reports examining the effect of anneal conditions on implanted regions, but these studies generally didn't look at optical properties or look at Al or B implantation, the two species used for current confinement in III-N devices[120–122]. Therefore, the electrical and optical properties of Al and B were studies across a wide range of annealing conditions to provide a comprehensive profile of how these species will behave in a GaN-based VCSEL.

2.3.2.1 Implantation Tests

GaN samples were grown on (0001) sapphire wafers in an atmospheric MOCVD reactor using trimethyl gallium and ammonia as precursors. The GaN samples used for absorption measurements were grown on dual-side polished sapphire (DSP) and the GaN samples used for resistance measurements were grown on single-side polished sapphire (SSP) and had a n/p/n structure. For the resistance measurements, samples were patterned with a Ti/Au (20/800 nm) hardmask to expose 40nm-wide channels for ion implantation, shown in Figure 2-8 (a). The absorption samples were blanket implanted.

Ion implantation was performed at room temperature by Leonard Kroko, Inc. in a two-step process to maintain a relatively constant damage profile throughout the damage region. Wafers nominally implanted with 10^{15} Al ions were first implanted at a dose of 10^{15} ions at 360 keV and then with a dose of 3.21×10^{14} ions at 90 keV. Wafers nominally implanted with 10^{15} B ions, were first implanted at a dose of 10^{15} ions at 180 keV and then with a dose of 3.21×10^{14} ions at 50 keV. Nominal concentrations of 10^{14} ions and 10^{13} ions were explored for both Al and B. All samples were tilted at 7º during implantation to minimize ion channeling. Secondary ion mass spectroscopy (SIMS) measurements were performed on the 10^{15} ions samples to observe penetration depths and are shown in Figure 2-8 (c-d) along with a comparative depth

profile for the Al-implant calculated using Stopping-and-Range-of-Ions-in-Matter (SRIM) simulations with a full damage cascade Figure 2-8 (b-c). Note the steeper drop of the concentration of B in the B-implant (~150nm/dec) compared to the Al-implant (~250nm/dec). This affects the impact of the implant on deep layers in the structure, such as the QWs.

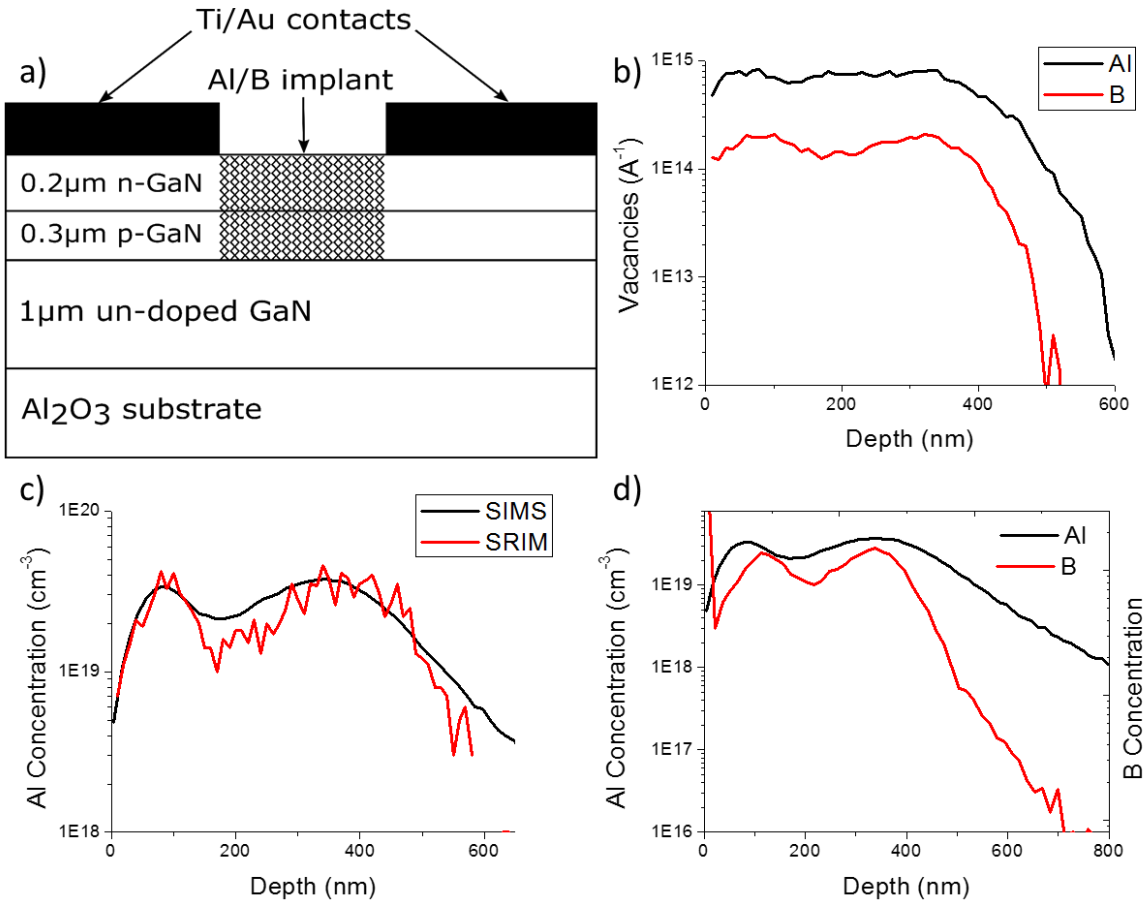

Figure 2-8. Schematic of the test structural epitaxial layers used for electrical testing (a). SRIM calculations of the damage at a 10^{15} cm^{-2} ion dose (b) suggest that the bimodal atomic distribution modelled in SRIM and measured in SIMS (c) produces a relatively constant crystal damage to a depth of ~450 nm. SIMS of the B and Al implanted samples implanted at 10^{15} cm^{-2} dose (d) shows that B has a much smaller penetration tail than Al. Unfortunately, a calibration standard was not available for the B; thus, the quantitative concentration profile is not known.

After implanting, atomic force microscopy (AFM) measurements were performed on implanted regions to observe roughness. Then, samples were diced and annealed in an AET RX6 Rapid Thermal Processor (RTA) for 20mins at temperatures ranging from 450C to 1000C

in 150C increments. Absorption measurements were taken using a Filmetrics FT-10R to measure transmission and reflectance on the DSP sapphire samples before and after annealing. High resolution x-ray diffraction (H-XRD) measurements were carried out using a Panalytical MRD Pro Diffractometer. After, Ti/Au (30nm/550nm) contacts were deposited on the SSP sapphire samples by electron-beam evaporation on both sides of the 40nm implanted channel and voltage sweeps were performed using a Kiethley 2420 before and after annealing.

2.3.2.2 Annealing effect on absorption

Figure 2-9 shows H-XRD measurements around the (0002) peak on the 10^{15} ions samples to measure crystal lattice repair as a function of anneal temperature.

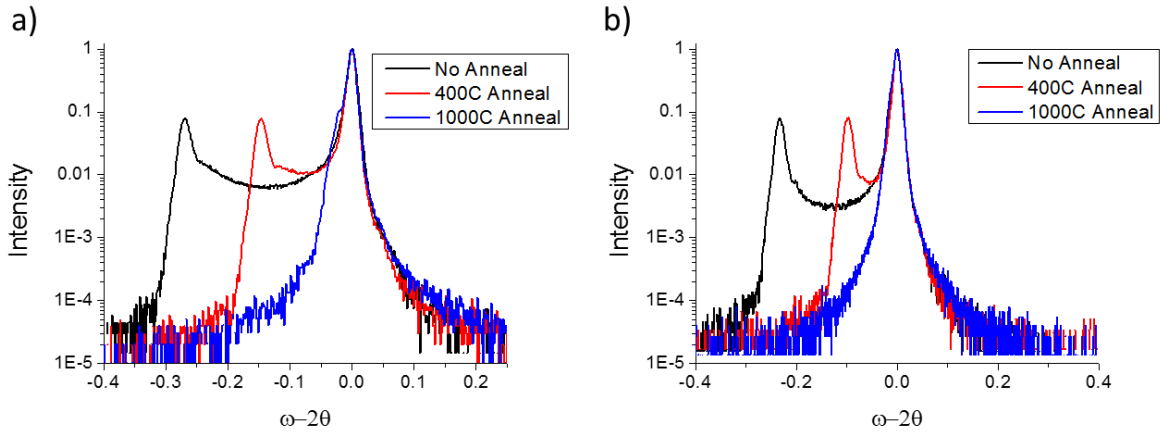

Figure 2-9 XRD scans of Al (a) and B (b) implantation after different anneals showing the reduction of the damage peak.

During implantation, incident ions create point defects in the crystal, including vacancies and interstitials. The ions expand the dimensions of the unit cell as it accommodates the extra ions, shifting the Bragg peak. The data shows that, before annealing, the Al (B) implantation creates a damage peak corresponding to an increase in the lattice constant. After annealing at 400C, the peak shifts by 0.122º (0.134º), indicating partial damage recovery. After annealing at 1000C, the implant damage is fully recovered for the B-implant, but a small damage peak

persists for the Al-implant, indicating that the damage created by B-implantation is more easily healed than the Al-implant. This is reasonable considering the difference in total damage predicted by the SRIM simulations which is demonstrated by the larger shift of the unannealed damage peak in the Al sample that the B implanted ones. AFM measurements found no significant increase in surface roughness as a function of dopant dosage, type (Al/B), or anneal temperature. Absorption data, shown in Figure 2-10, show a dramatic decrease in loss as the implant dosage decreases. Going from 10^{15} cm^{-2} to 10^{14} cm^{-2} and 10^{13} cm^{-2} led to a reduction in the absorption coefficient of 60% and 93% respectively. After annealing the samples in TJ regrowth conditions, the absorption of each dose decreased significantly, with the absorption coefficient at 450 nm decreasing by 85 %, 90 %, and 92 % for the 10^{15}, 10^{14}, and 10^{13} cm^{-2} samples, respectively.

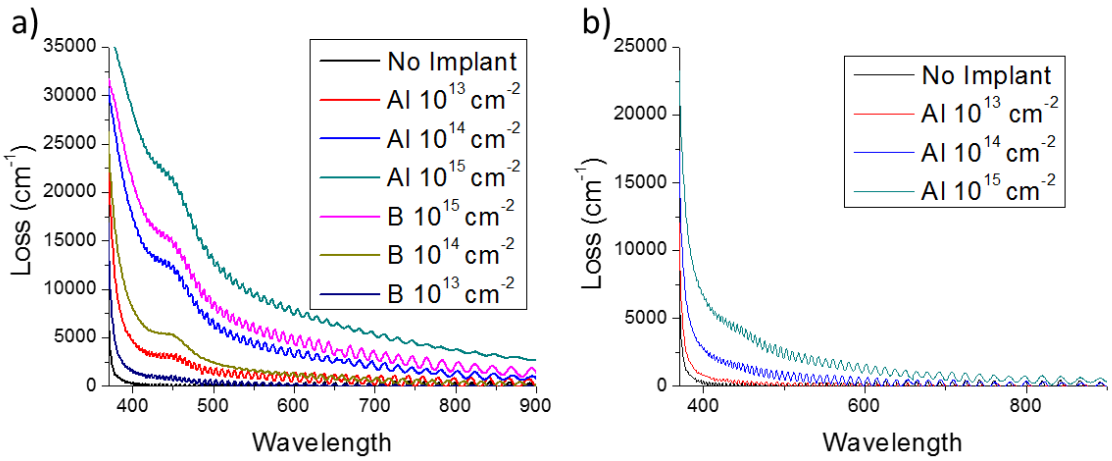

Figure 2-10. Shows how the absorption changes with ion dose and implantation species directly after implantation (a). The absorption of each dose decreases significantly after a 900 C anneal for 20 min under TJ regrowth conditions (b).

The 10^{15} cm^{-2} samples of both B and Al were further analyzed as a function of anneal temperature, shown in Figure 2-11. As expected, the absorption reduces as the anneal temperature increases, with absorption coefficients at 450nm (calculated assuming an implant depth of 450nm based on SIMS/SRIM) reducing by 50% after annealing at 400C, and by 90%

after annealing at 1000C for Al ions. Even with the reduced absorption, if these losses were present in the primary path of the optical mode, it would likely prevent the device from lasing. However, the minimal overlap of the optical mode with the implanted region allows for device operation with such high optical loss. Samples annealed in an MOCVD reactor at 900C for 30mins in hydrogen gas were compared with the samples annealed in the RTA and no significant impact on the absorption was noted by the difference in annealing method.

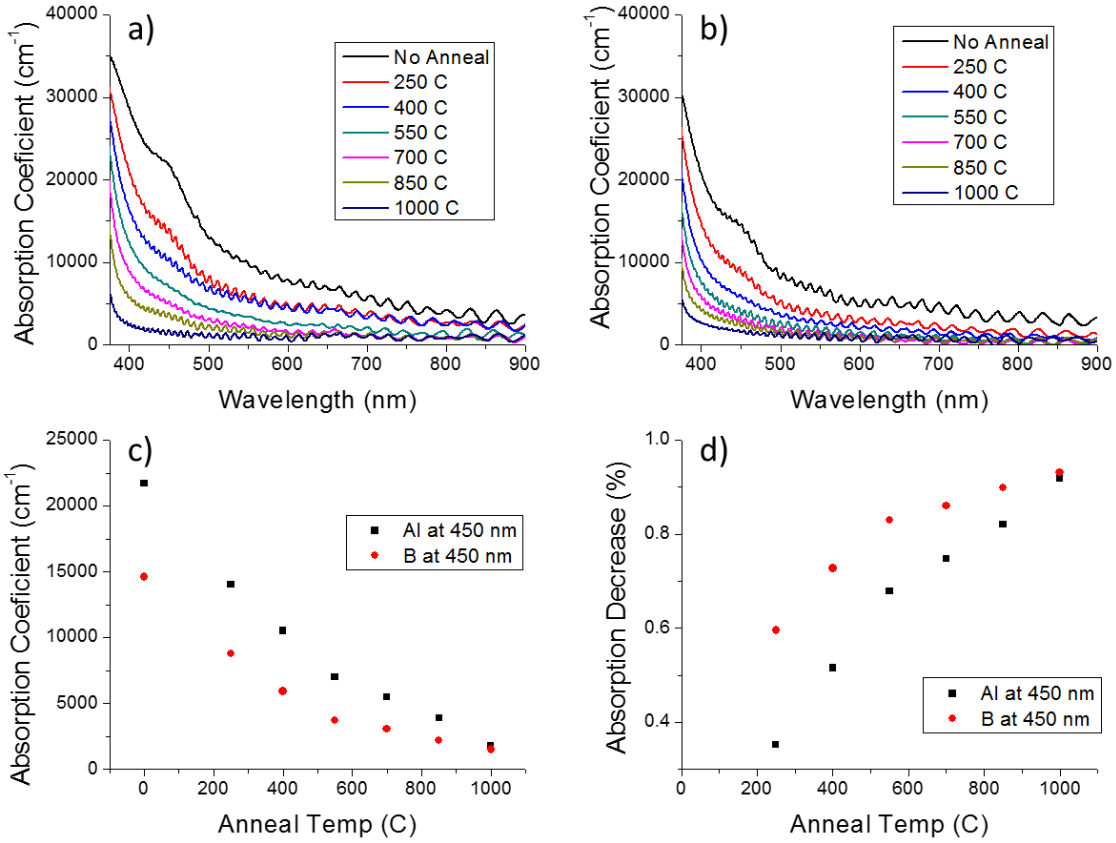

Figure 2-11 Impact of the anneal temperature on the implant absorption coefficient for Al (a) and B (b) implantation as a function of wavelength. At 450 nm, the absorption decreases steadily with increasing anneal temperature (c). The relative reduction in the absorption coefficient at 450 nm (d) shows that as the annealing temperature increases the implant becomes more equally recovered.

2.3.2.3 Electrical Impact

In VCSEL design, the implanted region needs to provide adequate electrical insulation to form a current confining aperture, thus the electrical conductivity was measured on annealed samples by depositing CTLM contact on annealed samples. It was found that the sample with B implantation with a dose of 10^{13} ions/cm^2 was quite conductive after the anneal. While all the other samples seemed relatively insulating there was suggestion that the 10^{13} ion/cm^2 Al sample might allow a small current flow. Due to this, it was decided that 10^{14} cm^{-2} implantation would be optimal for future devices as it minimizes the absorption while maintaining the electrical isolation that is necessary for device operation. It is recognized that the contacts themselves may have been poor as they were to implanted material. Thus, even the hint of conductivity in the Al 10^{13} ions/cm^2 sample was enough to dissuade from using that condition. More de3tailed electrical testing measuring just the implant conductivity may reveal that the lower dose is acceptable and that it would be possible to use 10^{13} ions/cm^2 to further reduce the optical loss.

2.3.3 Buried Tunnel Junction

The final current confinement scheme to be discussed is the buried tunnel junction (BTJ). This has been used to good effect in longer wavelength VCSEL devices for their uniform current injection and low loss[123–125]. The tunnel junction acts as a hole injector for the p-GaN and allows n-GaN to be used for current spreading. In a buried tunnel junction device, the highly doped region is confined to the aperture such that current will only flow through the area with the high doping. If low doping is used everywhere else to bury the junction, almost no current should flow outside the aperture until the junction breakdown voltage is reached. This is achieved by growing a planar tunnel junction and then etching the highly doped layers away

from everywhere outside the aperture before growing the current spreading layer. While this is a bit more complicated than the two previously mentioned confinement schemes, it incorporates both the aperture confinement and the current spreading, so the final process is not much more difficult. Additionally, the height difference introduces an effective index difference that is proportional to the relative difference in the cavity length within the aperture and without. This allows for some control of the index guiding. Forming a BTJ in the III-Nitrides generally takes three separate growths, which can be difficult to control repeatedly without the proper facilities.

Lee et al. recently demonstrated a VCSEL with a buried tunnel junction on m-plane GaN[126]. This device showed a significant improvement in output power and differential efficiency under CW operation, compared to previous devices with ion implant defined apertures. The better performance was attributed to lower optical loss, as well as an increased optical confinement. While the B ion implantation was reported to have negligible detrimental effects on device performance, the implantation tests showed that Al ion implantation caused more damage and had a higher absorption coefficient. In addition to further confining the mode to reduce absorption with potentially lossy regions outside the aperture, the increased index difference also promoted multimode lasing in the BTJ devices. They had a higher turn on voltage and differential resistance than the planar tunnel junction structures with an ion implanted aperture due to the re-passivation of the p-GaN in the multiple MOCVD growths. Test structures suggested that the current confinement began to degrade above 8 V as the junction outside the aperture began to turn on. It is important to ensure that there is not any contamination outside the aperture when growing the final n-GaN current spreading layer as it could act to locally distort the band structure. In this way, depending on the charge of the

contaminant, tunneling could occur and act as a leakage pathway. Due to this, ion implantation was used far from the edge of the aperture to ensure that the chance for a leakage path to form would be reduced on the actual VCSEL devices. Thus, it is unsure if leakage paths opened at 8 V on the actual devices, and if they did how much of an effect it had on the performance.

Several other confinement schemes have been demonstrated, including an air-gap defined aperture[127], Si diffusion in to the p-GaN[128], and plasma induced damage of the p-GaN[87], but have had limited adoption.

2.4 Optical Confinement

2.4.1 Mode Structure

Several of the applications presented require, or would benefit from, a source with stable, single frequency emission. Thus, it is important to consider the effects that impact the modal wavelength and shape. For a mode to resonate in the cavity, the round-trip length must be a multiple of the wavelength in the material. Thus, only certain wavelengths meet this criterion, and these represent the different longitudinal modes in a resonator. The wavelength of each mode is defined by the optical cavity thickness, through

$$L_c = \frac{m\lambda}{2\tilde{n}} \qquad \text{Eq. 2-4}$$

where $\tilde{n}$ is the effective index of refraction for the mode in the cavity, m is an integer, and λ is the wavelength. The effective index of the cavity is found by averaging the indices in the cavity, weighted by their length relative to the total cavity length. This is similar to the calculation for the internal loss but does not take into account the confinement factor. The mode spacing can be found by taking a differential to give:

$$d\lambda = \frac{\lambda^2}{2\,\tilde{n}_g L_c} \qquad \text{Eq. 2-5}$$

$\tilde{n}_g$ is the effective group index and is given by:

$$\tilde{n}_g = \tilde{n} - \lambda \frac{d\tilde{n}}{d\lambda} \qquad \text{Eq. 2-6}$$

While all these modes represent resonances, not all of them will lase. The lasing peak will be determined by the modal overlap with the gain minus the loss. Thus, to have a desired mode lase, the gain peak must be well aligned, and the loss should be minimized at that wavelength.

In this discussion of lasing modes, it is important to examine transverse modes in addition to longitudinal. The transverse modes correspond to the different mode shapes, or intensity profiles, that an individual longitudinal mode can take. For optimal laser performance, these modes are confined to the aperture area to minimize diffraction loss. The list of confined transverse modes is determined by the lateral index profile of the device design. Typically, as the index difference between the core (aperture area) and cladding (outside aperture) increases, the number of viable transverse modes increases. Since many VCSEL designs have an index step at the edge of the aperture to introduce optical guiding, this can allow multiple possible transverse modes which may result in modally unstable multimode operation. As the index difference is decreased, eventually the case of no index step is reached where the device is considered gain-guided. This means that the index guiding occurs only when the laser is pumped and occurs due to the index dependence on carrier density and temperature. Under operation, the carrier density in the aperture area increases, increasing the refractive index. Additionally, the temperature in the aperture increases under operation, further increasing the refractive index. While both effects are small, they do provide enough of a shift to confine a lasing mode. However, both of these effects are highly dependent on pump method, pump

intensity, and device design. Optical and electrical injection could give quite different carrier and thermal profiles. As the pump power increases, the guiding effect increases, potentially introducing mode instability. Finally, current spreading and thermal management in a device can impact the spatial distribution of these effects. Thus, for good mode control, optical guiding is often necessary.

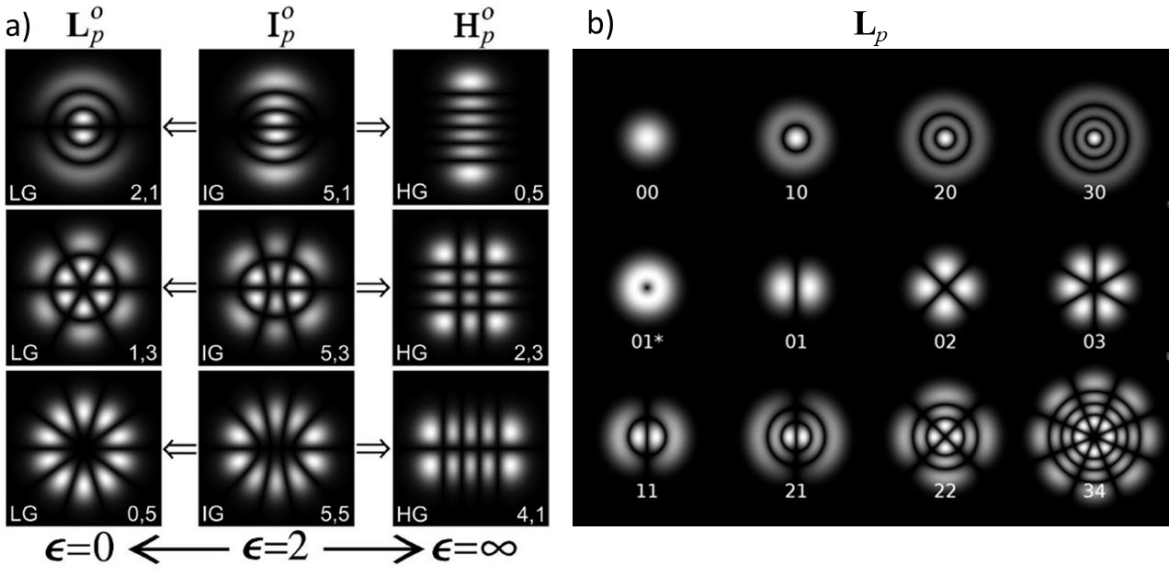

Figure 2-12. (a) Shows several LG, IG, and HG modes. Reprinted with permission from Ref [129] © The Optical Society. (b) The LG modes increase in complexity as the order increases. The $LG_{0,0}$ mode is referred to as the fundamental mode[130].

The transverse mode shapes are commonly described by Laguerre-Gaussian (LG), Hermite-Gaussian (HG), or Ince-Gaussian (IG) modes depending on the geometry of the cavity[129,131]. Laguerre-Gaussian modes are rotationally symmetric and are the most commonly observed set of modes in VCSELs. The Ince-Gaussian modes represent an elliptical geometry and serve as a continuous transition between the Laguerre-Gaussian modes and the Hermite-Gaussian modes with a rectangular geometry. Examples of these modes can be seen in Figure 2-12. In many III-N VCSELs filamentary lasing has been seen, which means that the lasing mode which is observed is not a well-defined structure described by one of the three mode categories

above.[81,106,107,113,117,126,127,132] This effect has been attributed to inhomogeneous current injection, spatial variations in the gain/loss, or local changes in the refractive index, though a detailed analysis of this has not previously been completed. As will be shown in Chapter 5, current inhomogeneity was the primary component in causing filamentation in the semipolar devices presented here.

The primary factor determining which modes lase is their individual internal losses. As the mode order increases, the total volume of the mode tends to increase as well. Consequently, it propagates through additional or different parts of the device, specifically it generally has a greater overlap with the lossy area outside the aperture. Thus, for higher order modes to lase, there needs to be sufficient index guiding to contain the modes primarily in the aperture. Alternatively, any intentional or unintentional defect in the aperture can select certain modes based on their shape relative to the perturbance. As the different transverse modes have varying lateral intensity profiles, the effective index seen by that mode is a bit different than the fundamental mode, which has the highest modal index[115]. Thus, the resulting wavelength of emission is slightly shifted to shorter wavelengths. Put another way, the phase of the light must be recovered after one round trip pass of the cavity. As the phase shift in the cavity depends on the modal intensity pattern, the resonant frequency shifts slightly with mode shape. This shift in the wavelength is generally much less than the wavelength shift between the longitudinal modes, which means that multiple transverse modes can align with the gain peak and lase at once. As many of the parameters affecting the mode change during operation, such as the temperature profile, the mode can be unstable without inclusion of controlling optical elements in the device design[133]. A final consideration for evaluating the modes that lase is spatial-hole burning. Spatial hole burning results from the spatial distribution of the carriers in

the device relative to the lasing mode, specifically when the injected carriers can't replenish the quantum wells fast enough to replace the carriers consumed through stimulated emission[134]. This can also influence the mode structure as it instigates competition between modes that have modal lobes in proximity to one another.

Thus, the mode selection is a complicated process that can be difficult to control. However, there are some ways to get the single mode emission that is necessary for some applications. One way is to increase the loss for undesired modes. In the simplest case, this just means shrinking the aperture size such that only the most compact mode, the fundamental mode, fits without significant overlap with the lossy areas outside the aperture. This could also be done by changing the mirror reflectivity across the aperture or providing focusing elements in the cavity design.

2.4.2 Mode Control

Below are two ways that have been demonstrated for controlling the beam profile. It is generally desired to have the fundamental mode as a small, circular beam with a low divergence. However, at UCSB, and elsewhere, ensuring the desired mode profile has proven difficult. Optical confinement can be achieved in many ways, however there is generally a choice between promoting the fundamental mode and total output power. Increasing the index contrast between the core (aperture) and the cladding (elsewhere) can restrict the mode's penetration into the surrounding lossy region, but it also allows higher order modes to lase. Allowing multimode lasing will generally increase the total optical power but may not be acceptable for certain applications[135]. As discussed previously, several of the current confinement schemes also provide good optical confinement, such as the dielectric defined

aperture with a convex structure that resulted in significant multimode lasing. There have been a couple demonstrations of optical elements that have successfully promoted specific modes.

Kuramoto et al. used the buried dielectric confinement method in a floral pattern, as shown in Figure 2-13, to form eight waveguides in one VCSEL which produced an in-phase supermode[90]. The mode had a low divergence angle of 2.8°, though not as low as theoretical calculations suggest. The increase in the divergence angle was attributed to an inhomogeneous emission intensity and position of the lobes across a device. Introducing the pattern did not seem to induce significant detrimental effects to the device performance relative to devices with a conventional circular aperture. While this method did not produce a single, fundamental mode VCSEL, it was able to demonstrate optical control of a stable supermode. A potential downside to this approach is that the sharp index step at the edge of the dielectric may introduce scattering loss.

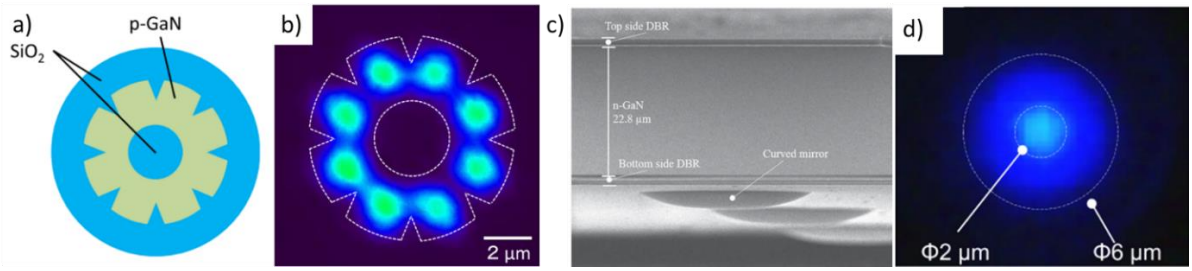

Figure 2-13 Shows examples of optical confinement with a floral pattern of dielectric current confinement (a,b). Reprinted from Ref 90, with the permission of AIP Publishing. Optical guiding using a curved back mirror (c,d)[109]. Copyright (2019) The Japan Society of Applied Physics

To counteract this possibility, Nakajima et al. used a curved mirror to provide mode control in their long (~ 20μm) cavity devices[136]. By changing the radius of curvature of the curved mirror, the beam waist formed on the planar mirror in the cavity can be controlled. They investigated the effect of the aperture size and the mirror curvature on the mode characteristics. For a set radius of curvature of 51 μm and an aperture diameter of 6 μm the fundamental mode

was dominant up to 1.5 × $I_{th.}$ As the aperture diameter was decreased down to 3 μm the higher order transverse modes disappeared. This trend was to be expected. However, they also found that the transition to higher order transverse modes could be shifted from 2 ×I_{th} to 5×I_{th} by increasing the beam size from taking up 68% of a 4 μm aperture, to taking up 91%. The multimode device showed a lower threshold current and a higher peak output power, which was suggested to be due to the higher optical confinement on the multimode device. This suggests that for larger aperture sizes, the mirror curvature could be tailored to give a beam size just smaller than the aperture to promote single mode emission at the cost of some device performance. It should be noted that the long cavities used in the study, also allowed multiple longitudinal modes in some cases which could be detrimental to applications that require single-frequency operation.

3 Methods

In this section, the fabrication process for VCSELs with a dual-dielectric DBR design exhibiting aperture definition via ion implantation or a buried tunnel junction will be presented as well as for any related test structures. The overall process for a flip-chip VCSEL can be split into two key parts: the epitaxial growth, and the processing. Before listing the details of the growth and the processing, an overview of the steps taken, and the considerations therein, are presented. The first step towards making a semipolar VCSEL began with addressing the steps of the process that are affected by the growth plane: the epi growth and the PEC etching. Thus, initially a growth recipe that produced relatively high power at the wavelength of interest was developed. Fortunately, there were students who had grown $(20\bar{2}\bar{1})$ LEDs prior to developing a VCSEL recipe. As such, I was able to cobble together some old recipes to use as a starting point for the VCSEL instead of having to make it from scratch. Unfortunately, due to drifts in the reactor conditions over time, the old recipes no longer provided optimal device performance, but they were a boon in providing a baseline from which to optimize. Additionally, an optimized high power blue EELD structure was consistently grown on another reactor, from which active region conditions could be replicated. Not only did this make growing a high-quality active region easier, but it also meant that the gain characteristics of that active region were known.

3.1 MOCVD growth

The MOCVD process begins, basically, with the ability to grow high quality LED epi. VCSEL growth is similar to that of an LED, with some additional considerations: loss must be minimized, surface roughness must be small, a sacrificial layer must be added, the structure

need be designed for high current densities, and the layer thicknesses must be precise. As the main loss associated with the epitaxial layers is the free-carrier absorption, minimizing the doping when possible addresses this issue. Ideally, an optimum is found in terms of managing the loss without significantly increasing the voltage. In addition to higher absorption, highly doped layers, particularly n-type layers, can lead to rough morphology. As the surface of the growth can have a significant impact on the amount of scattering loss in the final device, choosing appropriate growth conditions (e.g. doping, temperature, V/III ratio, carrier gas, etc.) is important for minimizing the final loss in the structure.

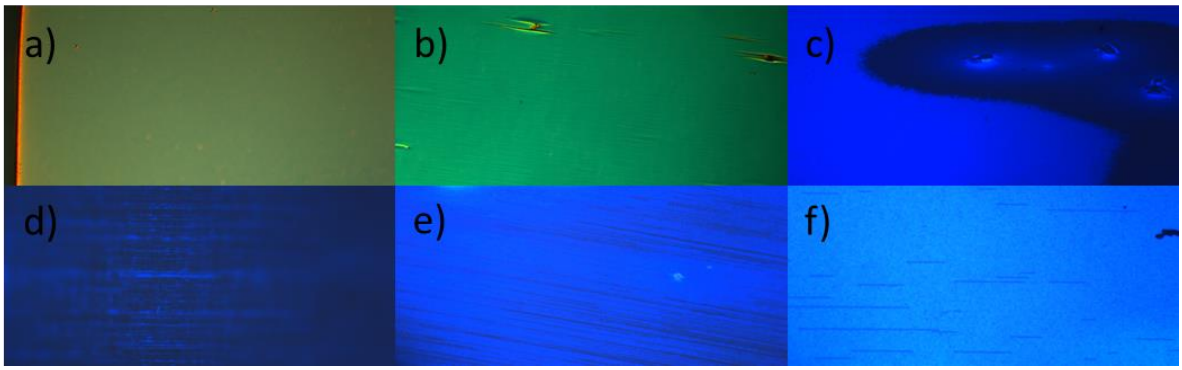

Figure 3-1 Shows DIC (a-b) and fluorescent (c-f) images of different growths. The increased growth thickness of 6 µm (b) compared to the short 500 nm (a) led to a greater number of growth defects. The fluorescent image of growth defects on a different sample (c) highlights the detrimental effects of poor-quality growth on the surrounding crystal, as well as the difficulty in dealing with inconsistent MOCVD growth. The bottom row of images shows the decrease in misfit dislocation density as the indium composition in the SL is decreases. The growth temperature increased from 875 °C (d) to 930 °C (e) to 975 °C (f). This clearly expresses the importance of controlling the total amount of indium in the structure.

For short wavelength devices, adding a sacrificial InGaN layer requires relatively little adjustment, and, depending on the rest of the structure may improve the quality of the active region[137]. However, as the wavelength gets longer, the total amount of indium incorporated into the device increases, threatening to cause relaxation. Thus, it is important to consider the sacrificial layer design with respect to the active region design. To check if a desired sacrificial

region has too much indium, a fluorescent microscope can easily show the presence of misfit dislocations as seen in Figure 3-1.

Devices operating under high current densities generally suffer from different performance degradation mechanisms than those under low currents. More precisely, the relative impact of the different mechanisms changes. For example, the ABC model suggests that the C coefficient term is likely to be more important than the A coefficient term for a laser compared to an LED due to its larger dependence on carrier density[138]. There are also additional complications that arise at the high current densities of lasers, such as spatial hole burning, that aren't considered in LEDs.

The precise layer thicknesses are needed to control the cavity standing mode of the final device such that the enhancement factor is maximized and the overlap with the highly lossy layers (e.g. tunnel junction layers) is minimized. First, this requires cavity layer design through simulation of the standing wave. This has been done using third party software, either Vertical or TFcalc. Once the desired thickness of each layer is identified, XRD calibrations are done to determine the exact growth rate immediately prior to growing the full device structures. An additional test is performed near the end of processing to find the resonance modes and determine how close the growth was to the desired structure.

3.1.1 Layer Optimization

The superlattice was the only layer that appeared in the semipolar recipe that was not present in the m-plane samples and represents the main growth layer that was optimized. The use of the SL originated with the LED recipes that were used as the base for the final VCSEL recipe. Since the superlattice is believed to improve the quality of the active region and is considered necessary for decent LED growth, it was retained in the VCSEL recipe. Unfortunately, this

was later found to introduce some thermal issues, as will be discussed later, and may not have been necessary under certain growth conditions.

To optimize the superlattice layer, the indium composition and the thickness of the individual periods were tested as shown in Figure 3-2(a-b). The indium composition was changed by maintaining a constant indium flowrate and changing the growth temperature. Figure 3-2 (a) shows that as the indium composition increased, with lower growth temperature, the wavelength of the QW emission increased and the power decreased. This was to be expected, as having a higher indium content in the base layer has been shown to increase indium uptake in QW layers[139,140]. As was shown in Figure 3-1, the misfit dislocation density increased dramatically as the growth temperature was decreased, likely leading to the reduction in output power. In a compromise between output power and achieving longer wavelengths, a superlattice growth temperature of 930 °C was chosen for future growths. Due to reactor variability, the level of misfits seen in Figure 3-1 were not observed in subsequent growths with this condition. The next variable considered was the thickness of each layer in the superlattice. Figure 3-2(b) shows that as the thickness of each layer was increased up to 3 nm, the wavelength increased, whereas the power remained relatively constant. To maximize the wavelength, 3 nm layers were chosen moving forward.

The number of superlattice periods, the TMI flowrate in the superlattice, the n-GaN growth temperature, the p^{++}GaN Mg concentration, and the QW growth temperature were also considered. However, none of those series produced clear trends, so the conditions chosen moving forward corresponded to whichever sample had the highest quicktest power. Over time, this method led to a recipe that produced high powered laser epi.

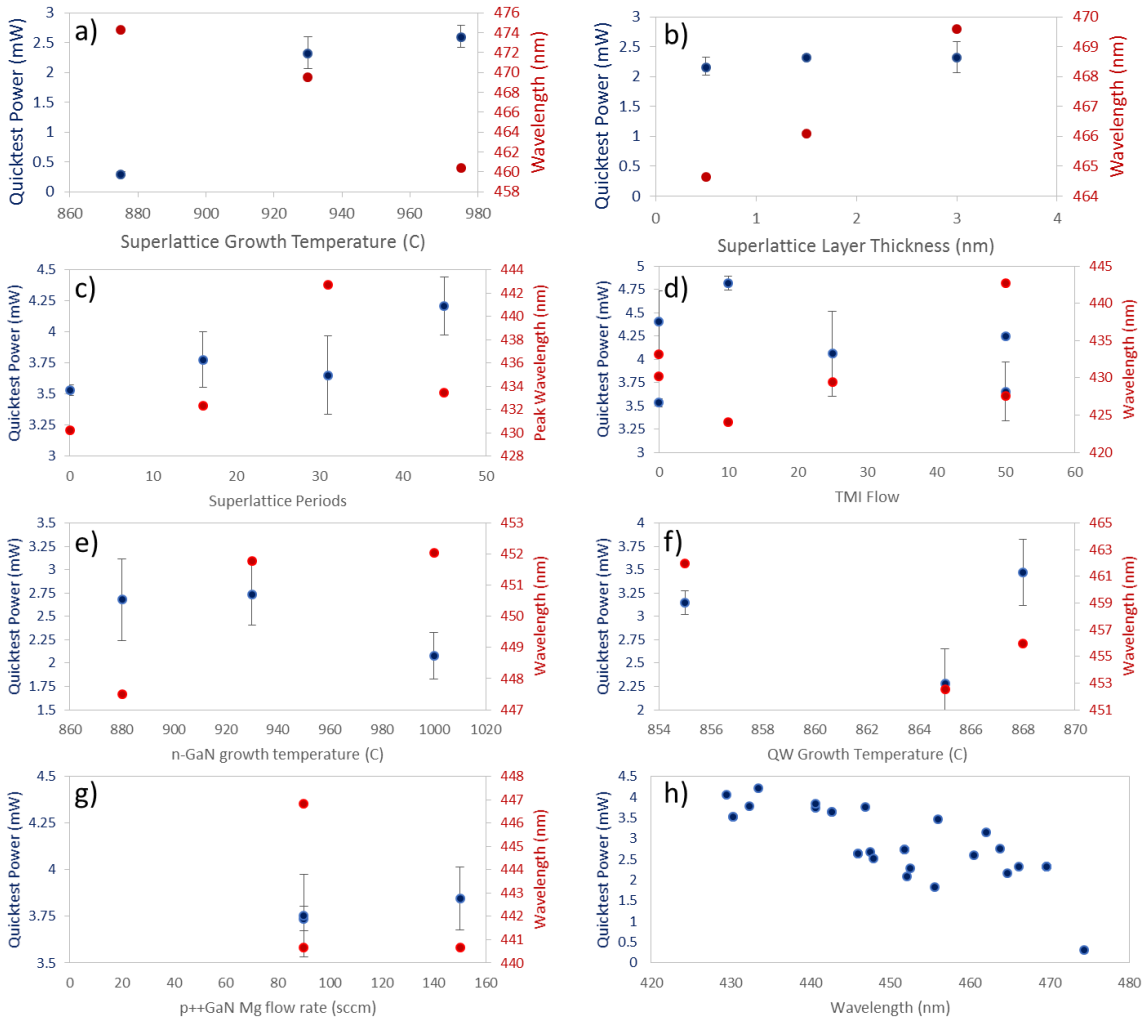

Figure 3-2. Growth optimization results showing how the output power and wavelength changed with the superlattice growth temperature (a) and the period thickness (b). Additional growth optimizations (c-g) yielded minimal results as there were no well-defined trends. The TMI flow (d) refers to the flow for the layer with the higher composition in the superlattice with tested flowrates of 50x25 sccm, 25x10 sccm, and 10x5 sccm for the high and low composition layers. Plotting the quicktest power as a function of the resulting wavelength (h) for all samples gave a vaguely negative trend, suggesting that the crystal quality began to decrease after ~440 nm.

3.2 Bonding and Substrate Removal

Before discussing the semipolar device process specifically, there is a key process step that is unique to the devices fabricated at UCSB that will be discussed: the flip chip bonding and the substrate removal using a photoelectrochemical (PEC) etching. Additionally, it is this step that seems to most severely limit the yield of devices and thus still needs further optimization. The

flip-chip bonding process can lead to significant cracking and non-uniform bonding with limited device transfer. Additionally, significant roughness can be observed after PEC etching and there can be large variations in etch performance between samples.

To remove the substrate and allow for the deposition of the p-side DBR, a PEC undercut etch is performed with 1M KOH. With recent VCSEL designs, three sacrificial QWs were etched through in a several hours. Originally, this was then followed by a top down etch in 0.001M KOH under an arc lamp illumination to remove n^+GaN and smooth the surface before DBR deposition. However, this step has been removed in favor of mechanical cleaning through swabbing in Tergitol detergent due to the large variation in etching results with doping of the n^+GaN. Removing the substrate in this manner allows for substrate recycling which is advantageous due to the high price of freestanding GaN substrates. Additional details of the two step process can be found elsewhere[62,74,132]. The multi-quantum well properties used for the sacrificial layers, such as QW/barrier width and number of QWs, are not currently optimized.

A gold-indium eutectic bond was used to bond the samples to the submount. This allows for self-planarization, is more tolerant of surface topography and particles, and requires much lower forces than thermocompression bonding. Forman et al. introduced this method at UCSB and used indium deposited on the submount and gold deposited on the devices to form the solid-liquid interdiffusion bond[141].

3.2.1 General PEC Etching

Bonding is a consistent component of most dual dielectric VCSELs, the unique component of the flip-chip process at UCSB is the PEC etching. As this etch had to be adjusted for semipolar samples it will be discussed in more detail. PEC etching uses light to generate electron-hole

pairs in the semiconductor layer of interest. Light, with an energy below the band gap of GaN, can pass through the substrate and be absorbed by the InGaN sacrificial layer. In an oxidizing solution, the holes at the surface of the absorbing layer initiate a redox reaction such that the system acts as an electrochemical cell[142]. The electrons travel to a counter metal deposited on the substrate, completing the circuit. The reaction involves the oxidative dissociation of the semiconductor, consuming the generated holes, as shown by the proposed reaction:

$$2GaN + 6h^{+} \rightarrow 2Ga^{3+} + N_2$$

The gallium ions react with the reactant in solution, often to form a gallium oxide. P-type GaN does not confine the generated holes to the surface, which significantly limits etching and allows for a high preference for etching undoped and moderately doped n-GaN layers. Highly doped n-type layers have very short photoexcited hole lifetimes and shallow band bending at the surface, thereby making it unlikely a generated hole will travel to the surface to react[143]. This can produce smooth surfaces once etching is complete when the sacrificial layer is bound by layers with low etch rates, with reported RMS roughness values near half a nanometer[144].

Two regimes have been noted in the PEC etching of GaN: diffusion-limited and non-diffusion-limited. The diffusion-limited regime is characterized by low etchant concentrations and high light intensities which produce a sublinear relationship between the light intensity and current generated. This regime produces smoother surfaces, but often lower etch rates[127,142]. It has been observed that stirring the diffusion-limited solution restores the linear relationship and often produced rougher surfaces[145]. Defects in the surface morphology can lead to roughening by locally enhancing or suppressing the etch rate. Smooth etching occurs when the diffusion-limited reaction rate is slow enough that local variations in reactivity are no longer significant. However, the diffusion limited regime has nonuniform etch rates due to boundary conditions imposed by the mask or sample geometry[146].

Numerous reactants have been proposed, such as KOH, HCl, H_2SO_4, H_3PO_4, tartaric acid/ethylene glycol mixture, and NaOH[142,147,148]. In a basic solution, the nitride and holes react with hydroxide ions to form a surface oxide:

$$2(In,Ga)N + 6h^+ + 6OH^- \rightarrow (In,Ga)_2O_3 + 3H_2O + N_2$$

The oxide then dissolves in the solution to expose a fresh surface for etching

$$(In,Ga)_2O_3 + 6OH^- \rightarrow 2(In,Ga)O_3^{-3} + 3H_2O$$

KOH and HCl are the most common reactants reported, with KOH far outweighing HCl. KOH produces a faster etching rate, but, depending on the material and concentration, it may etch slowly in the absence of light, thus other options may be better for a precise stopping depth[147,148]. KOH concentrations ranging from 0.0004 M-2.2M have been studied to determine the optimal conditions with widely varying results, likely dependent on the quality of the GaN being etched and the light intensity used[144,149]. Additional oxidizers can be used, such as $K_2S_2O_8$, for higher etch rates, smoother surfaces, and better uniformity of etching[143].

The etch rate depends on a number of parameters, such as reactant concentration, light intensity, crystal quality, orientation, and composition, dopant concentrations, temperature, device bias, and morphology[144,147]. Higher reactant concentration corresponds to higher etching rate, but lower etching quality due to moving further from the optimal diffusion-limited regime. Increasing absorption increases hole generation, which increases the etch rate[148]. Thus, using more intense light and shorter wavelength light generally leads to higher etch rates while maintaining crystal quality if one is not in a full diffusion limited regime[147]. GaN samples with high dislocation densities have been shown to etch without the need of light, leading to significant "dark" etching rates[150]. Additionally, increasing In content of the sacrificial layer, led to faster etching, likely due to increased absorption and lower material quality[144]. As with the majority of spontaneous chemical reactions, increasing the temperature increases the

etching rate. DC bias can be applied to ensure the confinement of the holes to the semiconductor-solution interface. Increasing the bias increases the etch rate, but after a certain rate is achieved, it can decrease the etch quality due to excessive bubbling. Nanostructuring of the etched nitride can increase the bandgap due to quantum confinement effects and result in a self-limiting etch mechanism that leaves very fine texturing after etching[147]. For optimal smoothness, this should be avoided.

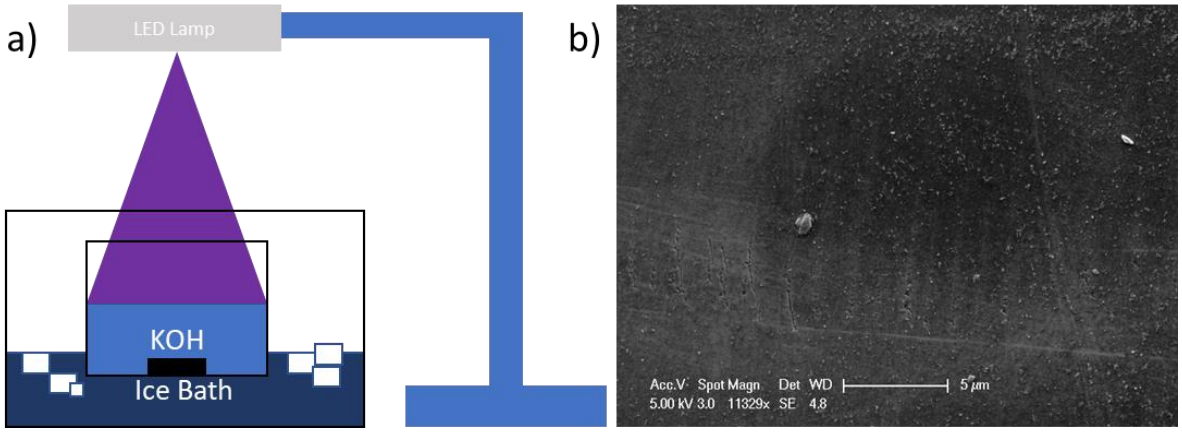

Figure 3-3 Shows a schematic of the PEC etching setup (a) and a SEM image of the surface of a sample after PEC etching but before cleaning. The "mossy" material covering the surface was projected to be a type of gallium oxide, whereas the particles were thought to be indium hydroxide[82].

For III-N VCSELs using a PEC undercut etch, the roughness of the resulting surface is of paramount importance, followed by etch selectivity and finally etching rates. The surface must be smooth to limit scattering loss and allow for lasing, thus the diffusion-limited regime of etching is desired. Additionally, only the sacrificial QWs should be etched to produce a well-defined cavity length across the VCSEL array. Lastly, the etch rate should be fast enough that all of the devices can be etched in a reasonable time for processing. To address these design parameters, initially a two-step etching process had been implemented. However, it was found that roughness encountered at the end of the etch was due to particulate matter left over from the etch. This residue was quickly removed by swabbing the samples in Tergitol detergent.

When the bonding was switched to the In/Au eutectic bonding from Au/Au bonding, the number of particulates increased due to the indium reacting with the KOH used during PEC etching.

Due to the impact of surface roughness on the scattering loss, it is very important to eliminate any sources of roughness that occur during processing. With the use of a MOCVD grown TJ, the main source of roughness is the residue or particulates left after PEC etching. The residue was thought to be a combination of Ga_2O_3 precipitated from the solution, and $In(OH)_3$ cubes that landed on the surface from the field, with swabbing presented as the optimal method of removal[77]. Alternative methods to swabbing were explored, as the mechanical force required damaged some devices. However, no chemical methods yielded comparable results. It was found that a concentrated KOH dip for 30 minutes would reliably remove the Ga_2O_3 surface contamination, though that didn't help remove the $In(OH)_3$ cubes.

To remove the $In(OH)_3$ layer, it was attempted to reduce the particles and dissolve them in solution using an acid. BHF, HCl, H_3PO_4, and H_2SO_4 were all tested at different concentrations, but all resulted in device failure in addition to removal of the particulates. BHF solution readily attacks Ti, which was the adhesion layer between the bottom of the devices and the In/Au bond. Thus, when BHF was used, the devices themselves were removed and lost in the solution. This could potentially be resolved by spinning PR and only exposing the top of the devices, but this solution was deemed too time consuming and not likely enough to succeed for pursuit. HCl, H_3PO_4, and H_2SO_4 attack In to varying degrees, so they would eliminate the integrity of the In/Au bond, removing large patches of bonding material and devices. Different times and concentrations were tried, but the times for each concentration that led to removal of the $In(OH)_3$ were comparable to the time required for bonding failure.

Potentially, changing the temperature could take advantage of the difference in activation energy associated with In and $In(OH)_3$ reactions, but this would require further studies into the energy of reaction that were considered out of the scope of this project when a viable, if tricky, method had already been identified. In conclusion, a feasible chemical method for reducing roughness was not readily found, and thus swabbing was concluded to be the optimal method for removing roughness.

3.2.2 Semipolar Considerations

Since PEC etching preferentially attacks the nitrogen face of GaN, it can produce a nice, smooth lateral etch on m-plane samples. However, as the orientation of the plane inclines towards -c, the component of the etch that is vertical increases. Thus, moving to etching of a semipolar plane had the potential to introduce additional roughness that would significantly increase the scattering loss. As discussed above, moving towards a more diffusion limited regime can help keep the etch roughness low. Reaction temperature, reactant concentration, and doping could all be changed to affect the reaction regime. The temperature could be used to change the rate of reaction relative to the diffusion rate by simple kinetics. Moving to a lower concentration of reactant could also increase the dependence on reactant diffusion. Finally, as the doping of the n-type GaN layer adjacent to the sacrificial QWs increases, the availability of holes at the surface decreases. Thus, increasing the doping, would also have likely decreased the reaction rate and decreased the unintentional etching of the n-GaN that would have occurred.

It has been reported that etching at 0 °C was able to significantly reduce the final roughness after substrate removal for EELD structures on $(20\bar{2}1)$ [151]. Thus, temperature was chosen to be the independent variable for reducing surface roughness. To test this on $(20\bar{2}\bar{1})$, mesas were

etched into epi containing sacrificial QWs, and they were flip chip bonded to sapphire submounts as would be done in the full VCSEL process. Then PEC etching was conducted in a temperature-controlled bath containing a water/ethylene glycol thermal transport fluid. The temperature ranged from room temperature to -5 °C, where it was determined the after etching roughness matched the epitaxial roughness at 300 pm by AFM as shown in Figure 3-4. The final etching of the VCSEL devices was conducted using a 1 M KOH solution under a 405 nm LED array for illumination at -5 °C to minimize roughness.

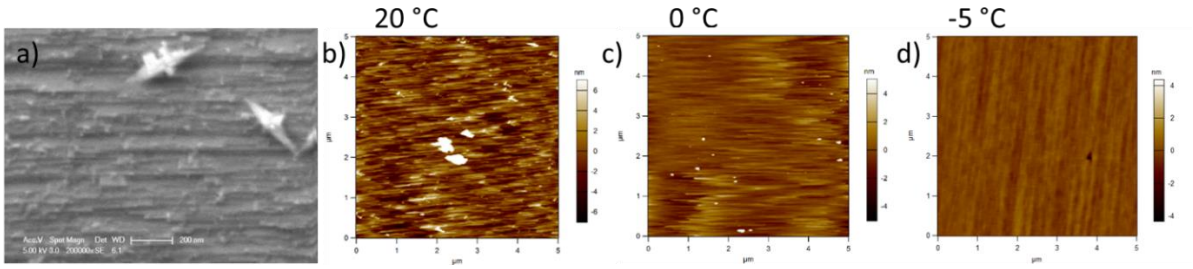

Figure 3-4. Shows the effect of the PEC etching temperature on the surface morphology on $(20\bar{2}\bar{1})$ test samples. The SEM image (a) and the AFM image (b) both depict the sample etched at 20 °C. The 5×5 µm AFM images (b-d) clearly shows that the surface morphology improves for lower etch temperatures. The measured RMS roughness values for these images are 2 nm (b), 700 pm (c), and 250 pm (d). These values varied by a couple hundred picometers across samples.

3.3 Process overview

Once the epitaxial layers are grown, the epi layers undergo a "quicktest" to gauge the quality of the growth. The power of the device is compared to previous growths to estimate the ability of the active region to provide sufficient gain. Additionally, the peak wavelength and FWHM of the spectra are found to see if they are within an acceptable range for the design wavelength. Finally, a current-voltage sweep is done to look for any leakage current that may indicate high defect formation or other epitaxial issues. If the growth is considered satisfactory, then boiling aqua regia is used to remove the indium on the samples, and processing is begun.

The two VCSEL designs, shown in Figure 3-5 achieve a dual-dielectric DBR design by flip-chip bonding the samples to a submount and removing the substrate through selective photoelectrochemical etching of a sacrificial layer. After the initial growth, a mixture of regrowths and ion implantation is used to define the aperture, depending on the structure. The tunnel junction regrowth allows the use of an n-GaN current spreading layer. Next, a DBR mirror is deposited followed by etching mesas to expose the sacrificial layer. Depositing p-side metal contacts completes the processing prior to bonding. The samples are then bonded to a submount and the substrate is removed. Contact deposition allows for measuring the resonant modes of the cavity under electrical injection to get the effective cavity length. Using the measured mode spectra, the top DBR can be deposited with modifications to counteract any discrepancy between the ideal cavity length and the measured one.

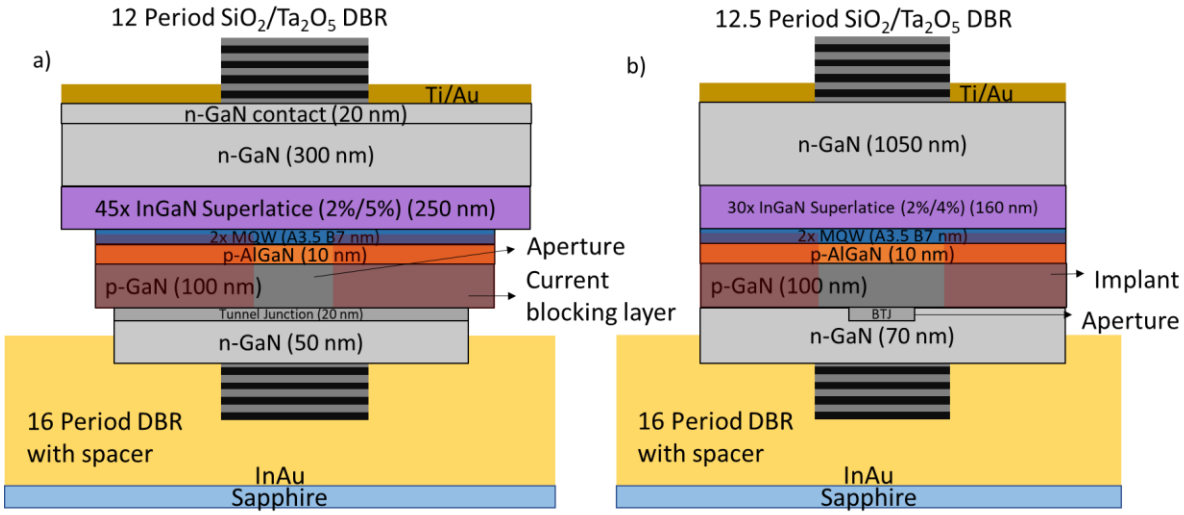

Figure 3-5 Shows the device structure of the IIA (a) and the BTJ (b) device designs. The implant present in the BTJ design is used to protect the active region during PEC etching and is placed far enough from the aperture to ensure there is no overlap with the mode.

3.4 Detailed Description

The epitaxial structure was grown using atmospheric MOCVD on freestanding $(20\bar{2}\bar{1})$ GaN substrates with the approximate thickness and doping of the layers shown in Table 3-1. The first growth went up to the p^{++}GaN layer, with some minor differences between the growth for the IIA devices and the BTJ devices. The first difference was that the IIA growth followed the sacrificial wells with an n^{+}GaN layer, whereas the BTJ samples had an AlGaN etch stop layer. The purpose of the n^{+}GaN layer was to provide a contacting layer for after the PEC etch that would have a low contact resistance. It has been reported that using a $SiCl_4$ etch prior to metal deposition can improve the contacts such that a contacting layer is not necessary[152]. Thus, for the BTJ samples an AlGaN layer that was resistant to PEC etching was grown. This layer was then be dry etched away after PEC etching with $SiCl_4$ to leave a surface ready for contacts, while providing greater control of the cavity length.

The next difference lies in the EBL. The IIA samples had a 10 nm thick EBL with a composition step at the edges of the AlGaN layer. Conversely, the BTJ sample had an abrupt composition change above the active region, was constant for 5 nm, and then graded in composition from AlGaN to GaN over the next 5 nm. This change in the EBL design was done to try and increase hole injection efficiency[153]. Finally, the total cavity length was different, with the IIA having a 5 λ cavity and the BTJ having a 9λ cavity.

After the initial growth up to the p^{++}GaN, the samples were activated by placing them in an oven at 600℃ for 15 min in an air ambient. To perform the quicktest, indium dots were rubbed onto the p-GaN surface through a shadow mask and indium was soldered to the back of the substrate. These contacts were probed, the power was measured with a large area photodetector below the sample, the current-voltage characteristics were measured with a Kiethley 2400, and

the spectra was measured with an Ocean Optics UV/Vis s2000. An initial "burn-in" was performed, where 200 mA was passed through the epi for 5s. Following this, the power and spectra were measured at 20 mA before a light-current-voltage sweep was measured. Heated aqua regia was used to remove the indium and prepare the samples for aperture definition.

Table 3-1. The full epitaxial structure grown with a total of three growths. The first growth stopped after the p^{++}GaN layer; the second growth consisted of the n^{++}GaN layer; and the third consisted of the final 70 nm of n-GaN for current spreading. The absorption coefficient values are for 450 nm light.

Layer	*IIA Thicknesses (nm)*	*BTJ Thickness (nm)*	*Doping Concentration (cm^{-3})*	*Absorption coefficient (cm^{-1})*
n^{+}GaN	5	5	5×10^{19}	30
n-GaN	50	65	2×10^{18}	1
n^{++}GaN	10	8	4×10^{20}	235
p^{++}GaN	10	10	2×10^{20}	180
p-GaN	100	100	9×10^{19}	80
p-AlGaN graded to p-GaN	-	5	3×10^{19}	30
p-AlGaN EBL	10	5	3×10^{19}	30
2x InGaN/GaN MQW	3.5/7	3.5/7	UID	
$In_{0.04}Ga_{0.96}N/In_{0.02}Ga_{0.98}N$ Superlattice	45x 3/3	30x 3/2.5	6×10^{18}	4
n-GaN	300	1050	3×10^{18}	2
n^{+}GaN	20	-	5×10^{19}	30
AlGaN Etch stop	-	5	-	-
3x InGaN/GaN Sacrificial QWs	3/7	3/7	UID	
n-GaN Buffer		~1300	1×10^{18}	

For the IIA samples, mesas were etched with reactive ion etching (RIE) to below the active region, but above the sacrificial wells. A Ti/Au hard mask of more than 300 nm of metal was deposited to protect the aperture area during ion implantation. Al ions were implanted with a dose of 10^{14} cm^{-2} and an acceleration voltage of 20kV. The does is an order of magnitude lower than that used previously for the m-plane VCSELs to limit the risk of optical absorption loss, since the lower dose was found to still provide adequate electrical isolation in the test samples. After implantation, the metal hard mask was removed with heated aqua regia; and the samples were cleaned in buffered HF for 5 minutes directly prior to the tunnel junction (TJ) regrowth.

A highly doped 10 nm n^{++}GaN tunneling layer followed by a 50 nm n-GaN current spreading layer and 5 nm n^{+}GaN contacting layer were grown by MOCVD. After growth, the p-GaN was reactivated through the sidewalls using the same conditions as before. To reduce the chance of sidewall leakage, a second mesa etch was performed with RIE several microns within the edge of the previous etch as seen in Figure 3-6 (4). The etch depth was a bit greater than the full tunnel junction regrowth thickness.

For the BTJ structure, after a 5 min BHF treatment, an 8 nm n^{++}GaN tunnel junction layer was grown by MOCVD. Alignment marks were etched in the samples by RIE. This was followed by shallowly etching 30 nm everywhere outside the apertures to remove the n^{++}GaN and p^{++}GaN. An alignment only etch was necessary because the subsequent aperture etch was not deep enough to clearly show the etched marks in the contact aligner. Despite defining the apertures with a buried tunnel junction, aluminum ion implantation with a dose of 10^{14} cm^{-3} at 20keV was also performed on these samples using the same metal masking process as above. This was done to protect the active region during PEC etching and prevent any potential current leakage through the pn-junction outside the aperture at high operating voltages. Since PEC etching takes advantage of photo-excited holes diffusing to the solid-liquid interface to promote oxidation, the heavy damage due to the implant into the active region inhibits the migration of carriers, thereby significantly decreasing the etch rate. The implant was kept 8 μm from the edge of the apertures to prevent any potential absorption from overlap of the implanted area with the optical mode. For the last growth, the n-GaN current spreading layer followed by the n^{++}GaN contacting layer were grown by MOCVD. RIE was used to define mesas which were etched to below the sacrificial layers. The p-GaN was re-activated through

the mesa sidewalls at 625 ℃ for 20 min under a N_2 atmosphere.[154] It is likely that this activation condition is not optimal and should be changed, as will be discussed later.

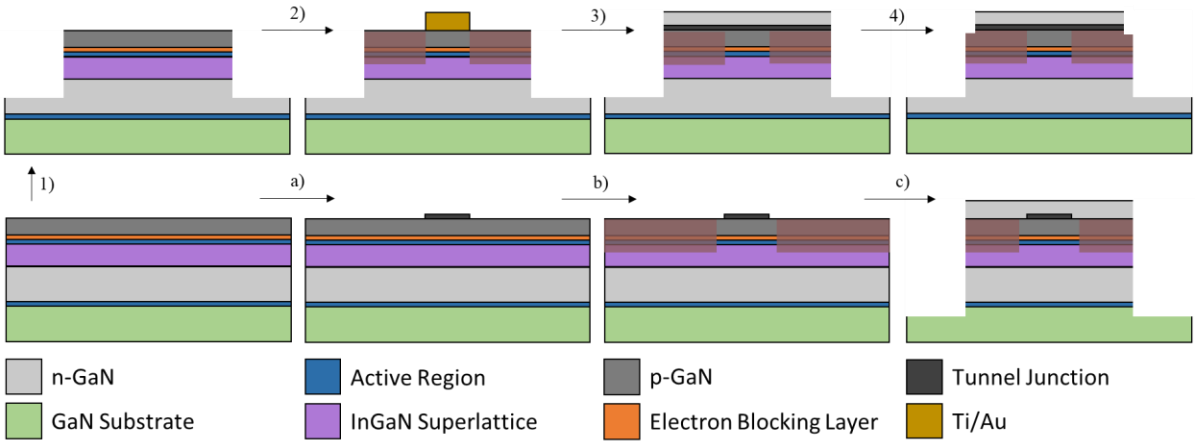

Figure 3-6. Shows the general process steps for the IIA (1-4) and the BTJ (a-c) VCSEL up to the TJ regrowth. Starting from the growth in the bottom left the IIA VCSELs underwent a mesa etch (1), ion implantation (2), a TJ regrowth (3), and a TJ etch (4). Conversely, the BTJ process starts with the TJ regrowth and etch (a), followed by ion implantation (b), and then the mesa etch (c).

For both sets of samples, Ion beam deposition (IBD) was used to deposit the 16 period SiO_2/Ta_2O_5 p-DBR with a Ta_2O_5 cavity tuning spacer. The IIA samples had a 65 nm thick spacer, whereas the BTJ DBR had a 1/3 λ Ta_2O_5 spacer. The spacer for the p-DBR was chosen to account for a difference in the cavity design wavelength and the wavelength seen in electroluminescence during quicktest. On the IIA samples a deep RIE etch was used to expose the sacrificial wells. Ti/Au was deposition on both sets of samples by e-beam in the etched trenches as the PEC cathode, and on the mesas as the anode contact.

Flip chip submounts were prepared by e-beam depositing Ti/Au on a bare sapphire wafer followed by thermally evaporating In/Au (1500 nm/ 200 nm). The Ti/Au acted as an adhesion layer for the metal to the sapphire and was necessary for further processing, while the second metal deposition of In/Au acts as the bonding layer. The sample was flip chip bonded to the

sapphire submount through solid-liquid interdiffusion bonding by contacting the metalized surfaces in a graphite fixture and being placed in an oven at 200℃ for 2 hours.

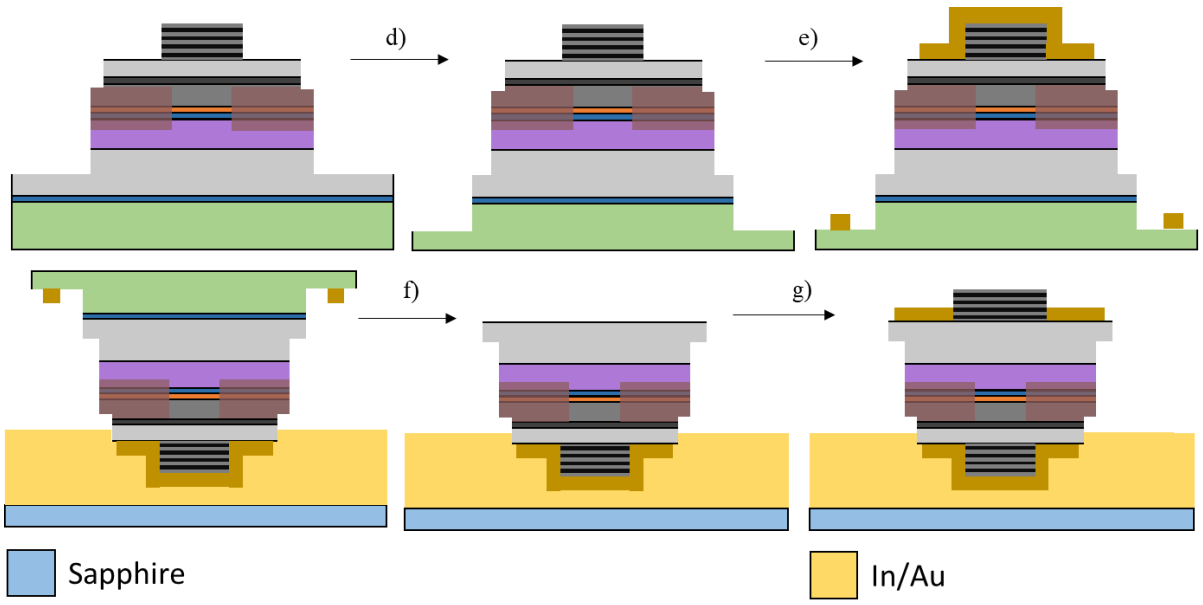

Figure 3-7. Shows the completion of the process begun in Figure 3-6. After the TJ a DBR is deposited to give the top left device. This is followed by etching down to the sacrificial layer (d) and depositing PEC electrodes (e). After flip chip bonding to the sapphire submount, the sample is PEC etched (f) and then has the top DBR and contacts deposited (g).

Unlike for m-plane, PEC etching of $(20\bar{2}\bar{1})$ samples room temperature can lead to a rough etching surface. However, by reducing the temperature of the etch, the final surface roughness can also be reduced. To optimize the surface, etching of $(20\bar{2}\bar{1})$ test samples was conducted at multiple bath temperatures. It was found that at -5 °C, the roughness became comparable to the epitaxial roughness at 400 pm RMS roughness as measured by AFM. Therefore, PEC etching of the sacrificial wells was performed in 1M KOH under a 405nm LED array at -5 °C for the IIA and the BTJ VCSELs. To remove the residue present after PEC etching, swabbing in a dilute Tergitol solution was performed followed by verifying the absence of particles in the SEM. If the samples were not clean, then they would be swabbed again. This generally took ~3-4 cycles. For the BTJ samples, RIE etching with $SiCl_4$ was used to remove the n-

AlGaN etch stop layer and improve the n-contact.[152] Once a clean GaN surface was obtained on both samples, Ti/Au n-contacts were deposited by electron-beam deposition.

Once the samples could be electrically contacted, resonance testing was conducted. A spectrometer was aligned to the top of the aperture and the spectrum was measured under pulsed and CW operation at ~1-10 kA/cm^2. The shift in the wavelength between pulsed and CW gave an indication of the thermal performance of the devices and affected the final design wavelength. The fabry-perot resonance peaks seen in the spectra were used to determine the actual cavity length by comparing to the resonance modes predicted in a TFCalc simulation. Once the actual epitaxial thickness was determined, a Ta_2O_5 spacer layer was designed to try and accommodate any discrepancies in thickness. This includes trying to align the TJ and the active region with the node and antinode of the expected lasing mode, respectively; as well as serving to align the cavity resonance with the gain spectral peak, as estimated by the peak of the room temperature spontaneous emission modified with a small red shift to account for self-heating. While the spontaneous emission and the gain spectra do not perfectly align, the spontaneous emission peak is used as a proxy to estimate the position of the gain peak. For the IIA devices a 12 period SiO_2/Ta_2O_5 n-DBR with a Ta_2O_5 spacer layer (45 nm) was deposited by IBD. Whereas for the BTJ samples, a 12.5 period Ta_2O_5/SiO_2 n-DBR was deposited.

4 Semipolar Ion Implanted Aperture VCSELs

This chapter details the process of moving from an m-plane VCSEL design, to producing the first demonstration of a semipolar III-N VCSEL on the path to reach longer wavelengths. The final devices had a 5λ cavity length, used the same IIA device design as the previous m-plane VCSELs, emitted at 445 nm, and had a peak pulsed power of 1.85 mW. Aside from the growth plane, the primary differences from the previous m-plane design were the lower ion implant dose, the MOCVD grown tunnel junction, and the shorter cavity length. As the implant and the TJ were discussed previously, only the cavity length will be discussed here.

4.1 Cavity Design

Once good quality epi and a smooth PEC etch were achievable, designing the cavity began. The cavity was originally designed to have a length of 5λ and emit at a wavelength of 435 nm for several reasons. The wavelength was chosen because it matched the measured gain curves from EELDs and matched the wavelength of the high powered quicktest samples grown during the recipe optimization process. Forman et al. showed that the cavity length had a great effect on the thermal properties of the devices and that for CW operation of m-plane VCSELs a long cavity was required[77]. However, increasing the cavity length also increases the total loss in the cavity and decreases the confinement factor. As an initial demonstration of a semipolar VCSELs was desired, CW operation was not necessary and using a shorter cavity gave a better chance of fabricating lasing devices. The final, and most important reason for choosing this design was that a large forest fire had disrupted our supply of substrates, ensuring that no new substrates would be received for several months. Thus, several of the best growth optimization samples were repurposed to make these VCSELs and this cavity was chosen because it is what was available. As the original LED optimization samples were not initially intended to be

VCSELs, the layer thicknesses were fixed, and a fully optimized design was not possible. Specifically, the distance between the active region and the TJ was set. Thus, for a given wavelength, the overlap of the standing wave with the QWs and the TJ could not be adjusted independently. To account for this and optimize the alignment of the standing mode with the layers of interest, Ta_2O_5 spacer layers were designed and deposited on both sides of the cavity during the DBR deposition steps. In designing the Ta_2O_5 spacers for these samples a compromise was made between maximizing the enhancement factor and minimizing the TJ induced loss, as seen in Figure 4-1.

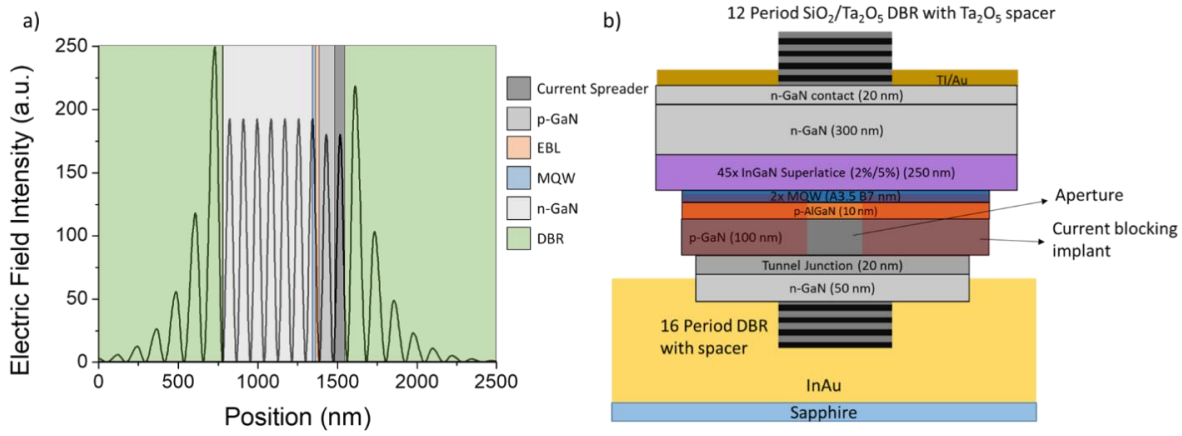

Figure 4-1. Shows the design for the IIA device. The electric field intensity (a) is overlaid with the different device layers to show that the active region aligns well with a peak of the standing wave, whereas the TJ aligns with a null. Due to the fixed distance between the layers as well as the set gain wavelength, the layers are not exactly aligned to the antinodes. The superlattice is incorporated in the "n-GaN" layer. The device layers and their thicknesses can be seen in the device schematic (b).

4.2 Device Results

The full fabrication method has been described in Chapter 3, so the focus here will be just the results. As shown in Figure 4-2, under pulsed operation with a 1000 ns pulse width and a 2.5% duty cycle, the peak power was 1.85 mW and the threshold current and voltage were 4.6 kA/cm^2 and 7 V for a device with a 12 µm diameter aperture. At threshold, the peak of the

spontaneous emission was at 435 nm, 10 nm shorter than the wavelength of the lasing mode, suggesting the presence of a misalignment between the gain spectrum and the resonance mode. This misalignment occurred due to the n-side Ta_2O_5 spacer layer being of the wrong thickness and likely resulted in a higher threshold current being required to produce the necessary gain. The reason the n-side spacer layer deposition thickness differed from the optimal thickness is not known.

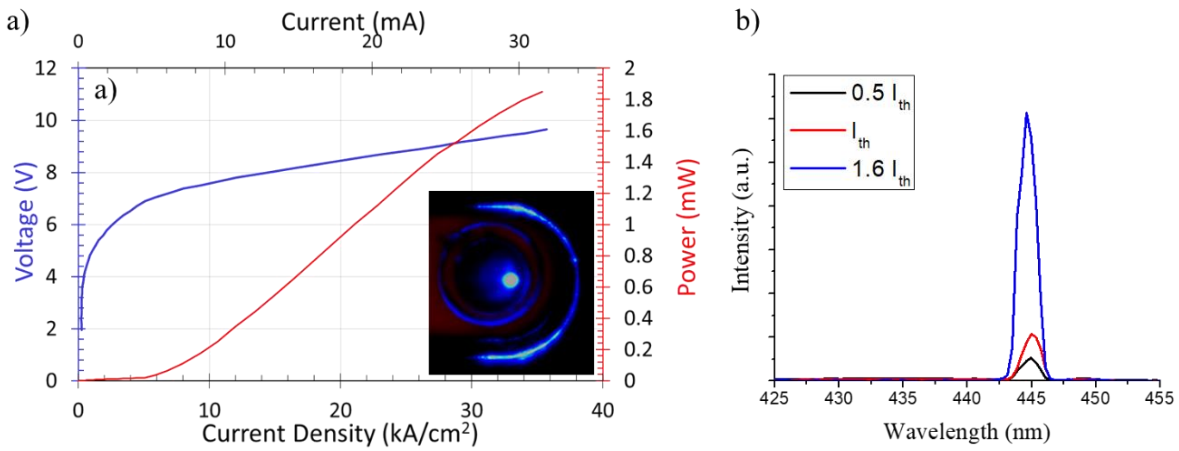

Figure 4-2 Light-current-voltage results (a) for a 12 µm aperture VCSEL under pulsed operation with a 2.5% duty cycle and a 1 µs pulse width. The inset of (a) depicts the nearfield pattern at 5% above threshold. This pattern is maintained at higher current densities. Reprinted with permission from Ref 155 © The Optical Society. The spectrum (b) is shown for different input currents. The small peak seen below threshold is a Fabry-Perot resonance mode that increased linearly with the broad spontaneous emission spectra below threshold.

It is expected that the spontaneous emission initially blue-shifts with increasing current injection due to band filling and screening of the polarization field, though the effect is significantly reduced compared to c-plane devices resulting from the reduced polarization fields across the quantum well on $(20\bar{2}\bar{1})$. The emission spectra is then expected to redshift due to self heating, though this effect is also minimal when using low duty cycle pulsed operation. Thus the net misalignment is expected to have remained relatively consistent throughout testing as will be discussed later. The differential efficiency was 2.4% for the mode at 445 nm,

which had a spectrometer limited resolution of 2 nm. The differential efficiency from one side of the device can be found with the equation:

$$\eta_{d1} = F_1 \eta_i \frac{\alpha_m}{\alpha_m + \alpha_i + \alpha_e} \qquad \text{Eq. 4-1}$$

where F_1 is the fraction of total output power emitted from the side of interest, η_i is the injection efficiency, α_m is the mirror loss, α_i is the internal loss, and α_e is the excess loss. The excess loss refers to the loss not accounted for by the mirror loss or the free carrier absorption.

4.2.1 Loss Analysis

Using a 1D transmission matrix model, the internal loss was calculated to be 10 cm^{-1} and the top and bottom mirror reflectivities were calculated to be 99.975% and 99.998%, respectively. The internal loss was calculated by multiplying the material absorption and mode overlap of each layer and summing over all layers. The absorption values used can be found in Ref. [132]. The mirror reflectivities led to an expected mirror loss of 1.2 cm^{-1} and an F_1 parameter out the top of 0.93[156]. The scattering loss due to roughness at the DBR interface is expected to be around 3 cm^{-1} (1-7 cm^{-1}) as estimated from AFM measurements on test samples[112]. Assuming an injection efficiency of 60%, as shown for semipolar $(20\bar{2}\bar{1})$ edge emitting lasers[157], the calculated differential efficiency out the top of the device would be 3.6%. Compared to the measured η_d, this suggests an additional 17 cm^{-1} of loss was not accounted for in the model.

The presence of this additional loss is likely due to multiple factors. As the lasing mode was redshifted relative to the design wavelength, the tunnel junction was likely shifted from the null of the standing wave and therefore potentially increased the internal loss. The difference in the lasing mode from the design wavelength suggested the cavity was 30 nm longer than originally thought. Assuming that difference is uniformly distributed among the epitaxial

layers and, taking into account that the standing wave is pinned at the p-side DBR interface, there is likely a 7 nm maximum displacement of the tunnel junction from the designed position. For an assumed 4 nm, and 6 nm depletion regions on the n and p-sides of the tunnel junction, respectively, the absorption loss is not expected to exceed 1 cm^{-1}. Figure 4-3(a) shows how the loss is expected to change with the shift of the TJ from the designed position assuming an absorption value of 250 cm^{-1} in the undepleted n^{++}GaN and 200 cm^{-1} in the undepleted p^{++}GaN. The fact that the loss is expected to decrease with a small shift of the TJ in the negative direction highlights that the cavity was not fully optimized and that the cavity misalignment may have helped marginally, depending on the direction of the shift. For another look at the effect of the TJ misplacement, see Ref [158].

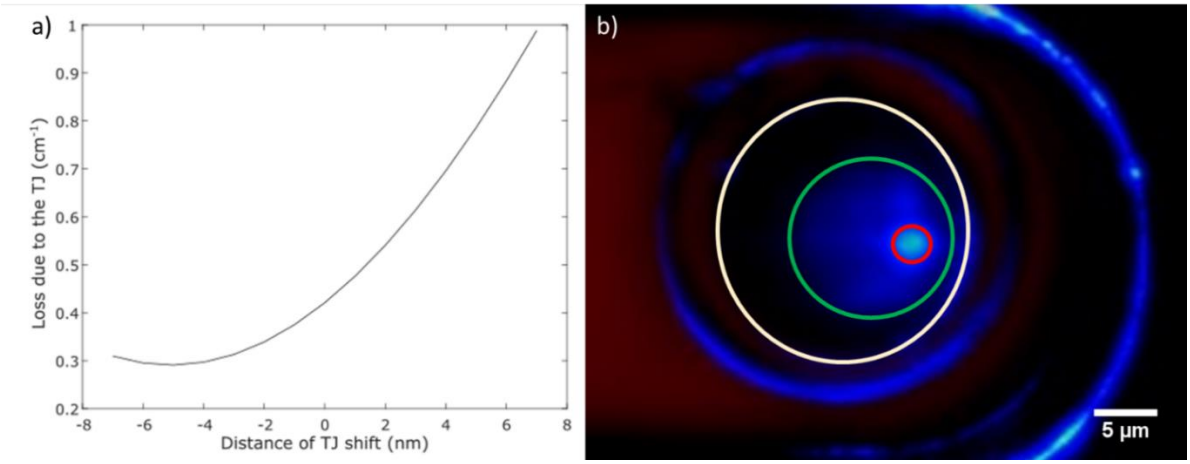

Figure 4-3. (a) The total loss due to free carrier absorption in the tunnel junction is not expected to surpass 1 cm^{-1}. Depending on where in the cavity the discrepancy in length originated, the loss due to the TJ may decrease relative to the original design. The nearfield (b) image shows that the lasing mode, circled in red, is near the edge of the unimplanted area, in green, and the metal contact, in white.

Additionally, Figure 4-3(b) shows that the lasing mode was near the edge of the aperture and, therefore, potentially overlapped with the implanted region and the contacting metal. To properly gauge the effect of the mode misalignment, the characteristics of the implanted area needed to be determined. The effective damage depth was assumed to correspond to the

effective depth of the ion penetration around the aperture. SIMS scans of a test sample gave an ion penetration depth of 55 nm from the surface for the implant at 20 keV used in these devices. This was used, in conjunction with the effective cavity length, to find the implant confinement factor. Figure 2-10 shows the absorption spectra due to ion implantation for different implant doses before and after annealing. The 10^{14} cm^{-2} dose introduced 1450 cm^{-1} of absorption at the lasing wavelength of 445 nm after annealing. This is lower than the previously standard 10^{15} cm^{-3} dose would have introduced, but still a large absorption coefficient. The loss associated with absorption outside the aperture in the IIA VCSELs, was found by determining the extent of overlap between these lossy areas with the mode. The overlap was determined by modeling the mode as a two dimensional Gaussian as a close approximation to the LP_{01} mode, and determining the percentage of the mode extending into the absorbing region, both for the implanted area and the metal as seen in Figure 4-4. Nearfield images gave the resulting $1/e^2$ spot diameter as 2.1 μm. As seen in Figure 4-3(b), it was difficult to ascertain the exact positions of the absorbing regions relative to the mode; thus, a range of potential losses was found by shifting the center of the mode 200 nm towards, and away, from the center of the non-absorbing region. Due to the nonlinearity of a Gaussian profile, there is a much greater effect on the calculated loss when the absorbing region is closer to the mode. The center of the unimplanted area was found to be 3 μm from the center of the mode, which corresponds to the implant introducing ~0.6 cm^{-1} of loss (0.3-1 cm^{-1} depending on the exact position of the edge of the implant). The lasing mode also overlapped with the metalized region, significantly increasing the absorption. The edge of the metal was estimated to be 4.2 μm from the center of the mode, which would suggest 0.0065 % of the mode overlapped with the metal. This gives 6 cm^{-1} of loss (3-12 cm^{-1} depending on the exact position of the edge of the metal) assuming

that the metal overlap only occurs over the effective penetration depth into the top mirror[159,160]. While these losses don't account for all of the excess loss, they do highlight the importance of centering the mode in the aperture. Accounting for the impact of absorption in the implant, the metal contact, and the tunnel junction leaves an additional 9 cm^{-1} to be accounted for. This loss is likely due to roughness propagating from the GaN interface into the DBR or absorption loss in the DBR. AFM on test samples, suggest that the scattering loss may have introduced 3 cm^{-1} of loss (1-7 cm^{-1} depending on the actual roughness on the real sample and the correlation length of that roughness). The loss is quite sensitive to DBR absorption, so a very small increase could cause the extra loss.

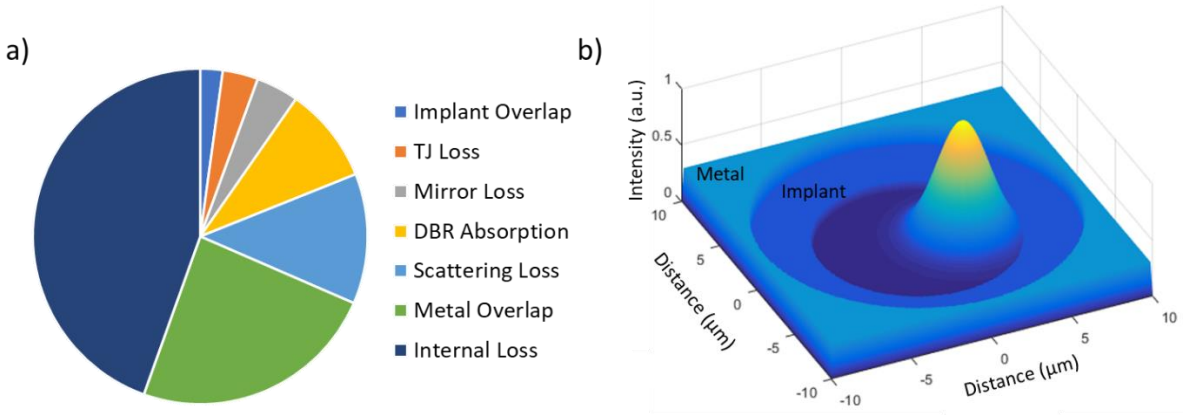

Figure 4-4. (a) Shows a breakdown of the different losses calculated for the IIA device. The segment associated with the DBR absorption merely corresponds to the amount of excess loss that was not accounted for elsewhere. The simulated 2D gaussian function (b) can be seen relative to the edge of the implanted area and the metal contact.

4.2.2 Polarization

Consistent, plane polarized light across an array had been shown for m-plane devices but had not been experimentally demonstrated yet on semipolar devices. Polarization was measured by inserting an optical polarizer between the device and an optical fiber coupled spectrometer aligned above the lasing mode. The polarization ratio (p) parallel to the a-axis is given by:

$$p = \frac{(I_{[\bar{1}2\bar{1}0]} - I_{[\bar{1}01\bar{4}]})}{(I_{[\bar{1}2\bar{1}0]} + I_{[\bar{1}01\bar{4}]})} \qquad \text{Eq. 4-2}$$

where I is the integrated intensity when the polarizer is aligned along the specified direction. $[\bar{1}01\bar{4}]$ is the projection of the c-axis along the $(20\bar{2}\bar{1})$ surface. The polarization dependence of the emission spectrum is shown in Figure 4-5 and the polarization along the a-direction is clearly seen.

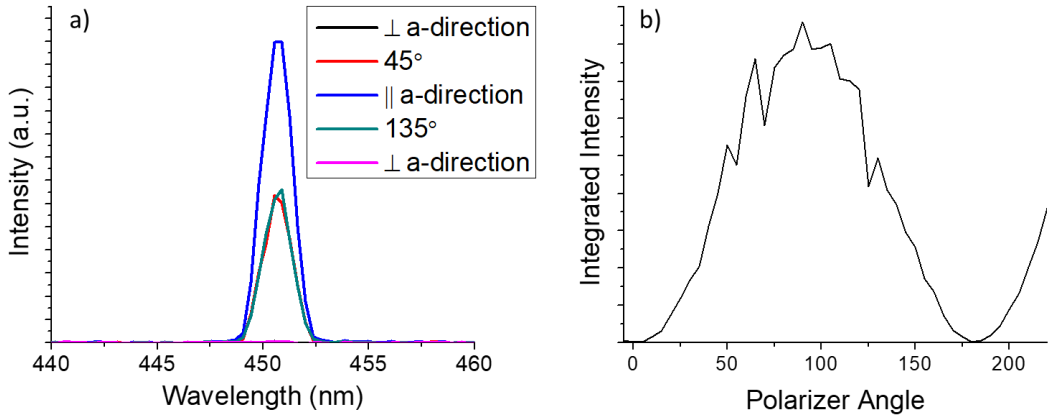

Figure 4-5. (a) Shows the spectrum of an 8 um VCSEL at different polarization angles. The polarization of maximum intensity was found to be parallel to the a-direction. The integrated intensity of the spectrum as a function of the polarization angle (b) has a bit of noise near the spectra parallel to the a-axis, but the polarization dependence is clearly seen.

4.3 Thermal Analysis

Although the threshold current and differential efficiency show improvement relative to previously reported m-plane VCSELs with a similar structure, the devices were not able to lase under CW operation. Lasing was achieved up to 50% duty cycle in the 12 μm device shown above and to a stage limited temperature of 70℃. Above threshold, the semipolar devices had a higher differential resistivity than the m-plane ones. This increased operating voltage increased the dissipated power in the device, increasing the heat generated. Additionally, the semipolar device was significantly shorter, increasing its thermal resistance to heat dissipation.

The thermal impedance of the devices was estimated from the shift in the spontaneous spectrum with changing stage temperature ($\Delta\lambda/\Delta T_{st}$) at 1% duty cycles and by changing duty cycle ($\Delta\lambda/\Delta P$) at fixed stage temperature. $\Delta\lambda/\Delta T_{st}$ and $\Delta\lambda/\Delta P$ were found to be 0.07nm/K and 125 nm/W, respectively, which give a thermal impedance of 1850 K/W. This analysis was also done on the lasing mode and gave a similar thermal impedance.

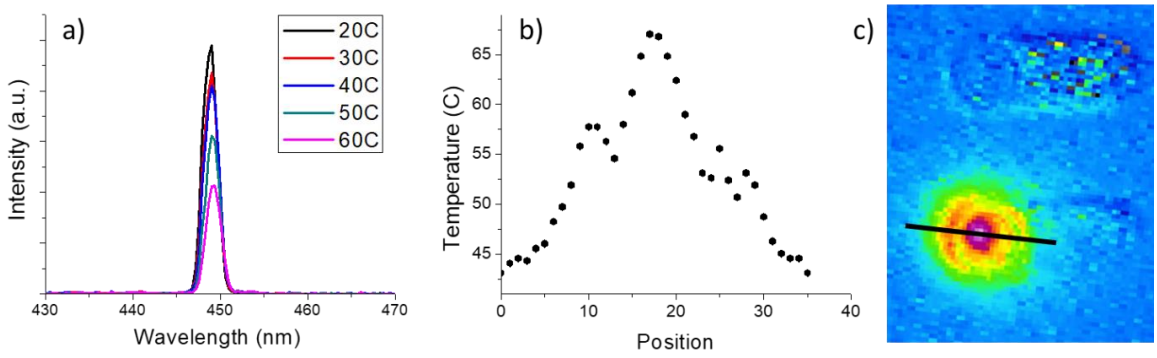

Figure 4-6. The peak of the lasing spectra (a) can be seen to redshift with increasing stage temperature. Additionally, the power of the lasing mode can be seen to decrease with the device held at a constant 6.5 mA of current. The line scan profile (b) of the thermal microscope image (c) shows a peak device temperature of 67 °C at an input current of 3.3 mA. The side peaks on the profile correspond to the edge of the DBR and supports the idea that the presence of the DBR encased cavity affected the peak temperature measured and resulted in an underestimate of the thermal impedance.

The changing operating temperature with changing input power was more directly measured using nearfield images with a thermal microscope at different CW operating conditions, as seen in Figure 4-6. There are several issues with directly measuring the temperature with a thermal microscope that limit the accuracy of the temperatures measured and need to be considered to determine their effect. Firstly, the thermal image records the emission from the entire device. Neither the GaN layers nor the DBRs are expected to significantly absorb in MWIR, so the microscope recorded a weighted average of all the layers' temperature in the stack. As the Stefan–Boltzmann Law predicts the total thermal radiation increases with temperature to the fourth power, it is expected that the hottest parts of the cavity

contributed the most to the temperature measurement. Thus, this effect is likely to lead to an underestimate of the temperature but should be close. Next, the structure contains several different materials with varying emissivities. To translate the emission intensity to temperature the effective emissivity of each point is calibrated by heating the sample to 40 °C and taking an image. However, the emissivity can change with temperature, and this change is material dependent. In the end, it is unlikely that the emissivity will change drastically over the temperature ranges seen in the VCSEL structure. Lastly, there are a number of different material layers that will cause reflections which can shift the intensity spectrum of the emitted light. While these considerations cast some doubt that the recorded temperature is precisely the actual operating temperature, it is likely that the trend in changing temperature with changing input power is not too far off from reality and can provide a reasonable lower bound. This method suggests a value of 1500 K/W for the 12 μm device presented above and was used to estimate the thermal impedance for the other aperture sizes shown in Figure 4-7.

At 50% duty cycle, the LIV curve began rolling over at 12.6 mA and 7.9 V, which would suggest a roll over temperature of 110℃, in between previously reported values of 98 C [101], and 160 C [82]. Investigating the shift in the lasing peak with changing duty cycle gave a $\Delta\lambda_{lasing}/\Delta P$ of 25 nm/W, indicating that as the input power increases for a set operating temperature the lasing mode shifts towards the gain peak at 100 nm/W. Additionally, the lasing mode shifted at 0.01 nm/K with changing stage temperature, significantly less than the spontaneous peak. In actual operation it was found that there was a negligible change in the peak separation when changing input current for the 1 μs pulses used in most of the testing. An 8 μm diameter device operated up to 75% duty cycle with a 500 ns pulse width.

4.3.1 COMSOL Modelling

COMSOL modelling compared to measured thermal values and used to evaluate several aspects of the device that were thought to be significant in producing the high thermal impedance. The effect of the presence of the bottom dielectric DBR was not intensely investigated as the poor thermal performance of dielectric DBRs is well known and there isn't much to be done about it. The first, and most visibly apparent aspect of the device, is the crack in the bonding interface as highlighted in Figure 4-7 (d). As the metal was the primary path for heat dissipation, having a poor connection to the heat sink was quite worrisome. To model the crack, a layer between the bonding metal of the device and the submount was inserted with an effective thermal conductivity intended to account for the variable contact. It was found that above a couple W/mK the thermal conductivity of this layer didn't significantly affect the total thermal impedance. This suggests that for somewhat decent contact, the crack was unlikely to present a significant thermal barrier. Using the model, it was found that the crack, with about 5% of the area contacting, only introduced about 2% of the total thermal impedance.

The next potential issue is the use of a superlattice in the epitaxial layers. Due to alloy and interface scattering, the thermal conductivity of the SL is expected to be less than GaN. As the thermal impedance is heavily dependent on the total cavity thickness, having the superlattice could have effectively shortened the cavity length in terms of available GaN for heat dissipation. Using a virtual crystal model, Tong et al. simulated the thermal conductivity of InGaN as a function of In composition[161]. For the average In composition in the superlattice of 4%, the thermal conductivity was expected to be ~80 W/mK. This represents an upper bound due to the addition of an unknown amount of interface scattering in the actual superlattice, likely decreasing the thermal conductivity compared to a bulk alloy layer. Replacing the GaN

in the cavity with the superlattice, was simulated to have led to a minimum of a 10% increase in the thermal impedance of the devices.

The other alloy that needs to be considered is the In/Au bonding metal. While, this should also be affected by alloy scattering, the composition of the metal changed throughout the bond, making its effect variable and difficult to quantify. To estimate the thermal conductivity of the In/Au alloy, the COMSOL simulation was fit to the thermal impedance measured for the actual device via the spectra method. This resulted in a metal thermal conductivity of ~60 W/mK and, while higher than originally expected, was considered reasonable. Using this value, the In/Au alloy was found to represent around 20% of the total thermal impedance and introduced a 15% increase relative to using gold. However, it is important to note that when bonding, the devices are pressed into the bonding metal, thereby increasing the thickness of the metal in the heat path. This would be difficult to achieve with gold.

Table 4-1. Summary of thermal conductivities used in the COMSOL model.

Material	*Thermal Conductivity (W/m K)*
Sapphire	35
In/Au	60
Crack	3
DBR	0.6
GaN	130
Superlattice	80

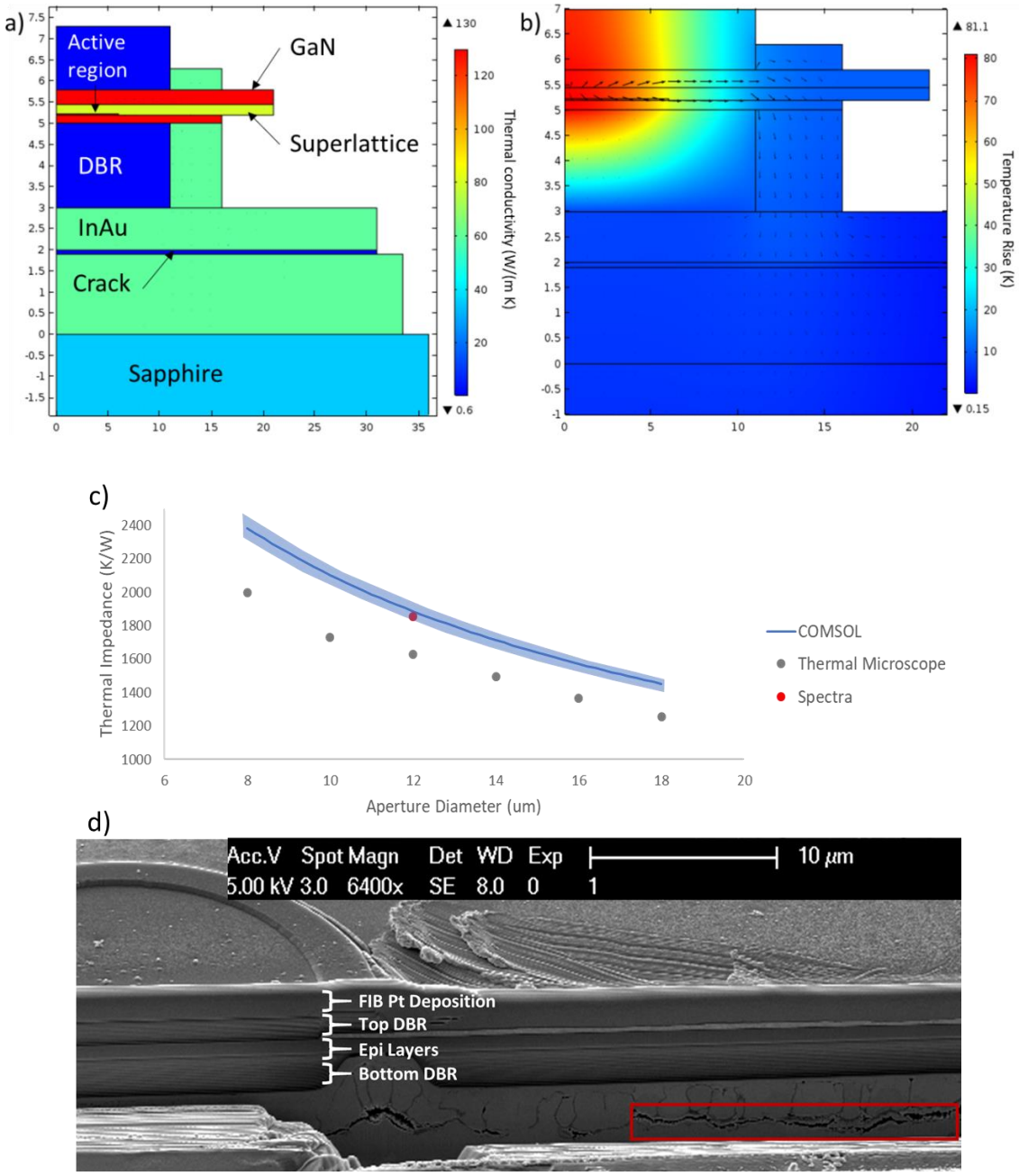

Figure 4-7. Schematic of the device in the COMSOL model (a) with the colors representing the relative thermal conductivities of the materials. The temperature profile (b) of the 12 μm device at threshold has arrows representing the heat flux in the structure. The simulated and measured effect of the aperture size on the thermal impedance (c) show a decreasing thermal impedance with increasing aperture size. The COMSOL model captures the trend in the aperture size dependence seen in the thermal microscope date, while agreeing with the higher thermal impedance seen from the spectral analysis. The blue shaded area of the plot represents a 10% increase or decrease in the thermal conductivities of the layers discussed: the superlattice, the In/Au, and the crack. The secondary ion image taken with focused ion beam microscopy (d) shows the voids formed in the bonding metal, highlighted by the red rectangle. The image suggests about 10% of the bonding interface was well connected for thermal transport. Reprinted with permission from Ref 155 © The Optical Society.

The final consideration consists of accounting for lithographic variances. The main thermal barrier is the p-side DBR, as it sits between the active region and the heat sink. That feature is defined by a lift off mask with negative resist. Using negative resist produces an undercut in the resist that is needed for effectively lifting off the thick DBR deposition. However, it also allows for some deposition if the DBR material under the "overhang" of the resist. This can effectively increase the size of the DBR relative to the mask design. Alternatively, due to mask misalignment, the aperture may be closer to the edge of the DBR than expected, allowing an easier path for heat dissipation in certain directions. To consider these effects, the effect of the p-DBR diameter on the thermal impedance was simulated. It was found that even with several micrometer variations, effect on the thermal impedance was not significant relative to the two previous concerns. Thus, this is unlikely to have had a significant impact on the thermal analysis results of the IIA device. A summary of the thermal conductivity values used in the simulation is given in Table 4-1. The sapphire and GaN thermal conductivities represent the default values used in COMSOL. The "DBR" material is based on COMSOL's default values for SiO_2 but has a thermal conductivity slightly lower than the average thermal conductivity between SiO_2 and Ta_2O_5. The slight decrease was intended to account for the large number of interfaces. Due to the low thermal conductivity of the DBR, most heat flow is through the metal and changes in the simulated DBR thermal conductivity did not have a significant effect on the simulated results.

4.4 Conclusion

In conclusion, we demonstrated a blue $(20\bar{2}\bar{1})$ semipolar VCSEL with a cavity length of 5λ, an ion implanted aperture, and a dual dielectric DBR design. The peak power under pulsed operation at a 2.5% duty cycle was 1.85 mW for a 31.5 kA/cm^2 current density. The threshold

current was 4.6 kA/cm^2 and the differential efficiency was 2.4% for the mode at 445 nm of a device with a 12 μm aperture. The lasing emission was found to be 100% plane polarized along the a-direction. Lasing was achieved up to a 50% duty cycle and the thermal impedance was estimated to be 1800 K/W.

5 Buried Tunnel Junction VCSEL

This chapter discusses the results from making a semipolar VCSEL with a buried tunnel junction as opposed to using ion implantation to define the current aperture. The BTJ device design was first demonstrated successfully with III-N VCSELs by Lee et al. on m-plane devices[126]. Those devices showed some marked improvements compared to the ion implanted aperture devices that were developed previously. This was attributed to better lateral confinement of the mode and lower optical loss. As those seemed to be the predominant issues with the IIA semipolar device, we hoped that moving to a BTJ design, shown in Figure 5-1, would also significantly improve the device performance again.

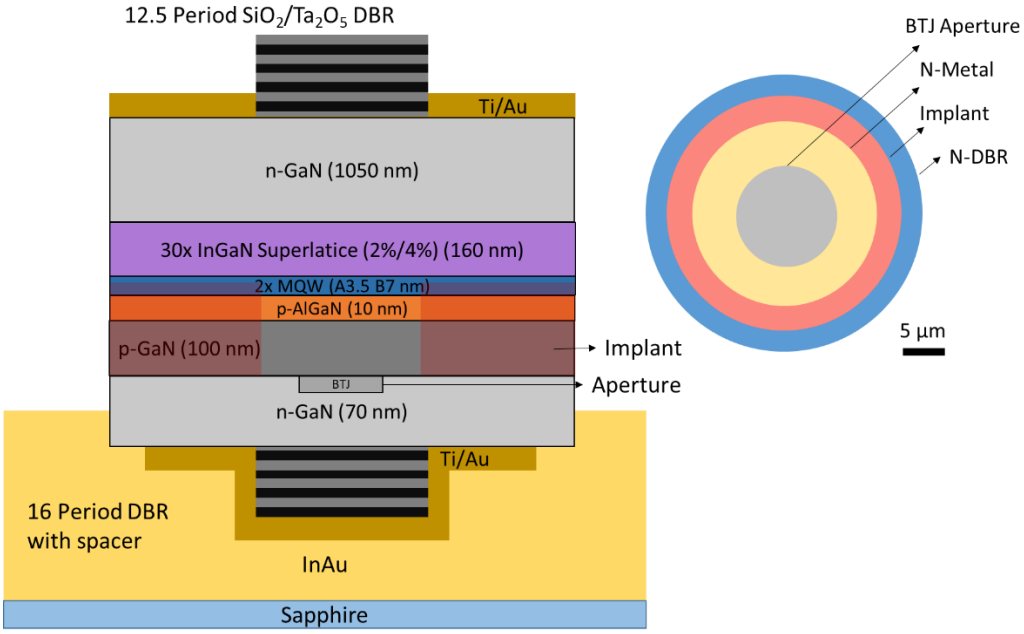

Figure 5-1 Simplified schematic of the BTJ device structure (left). Top down view showing the different device layers to scale that can be seen in some of the nearfield images shown later.

5.1 BTJ Device Results

As shown in Figure 5-2**,** the light-current-voltage (LIV) characteristics of a 12 μm VCSEL were analyzed under continuous-wave (CW) operation, and under pulsed operation with a 1 μs pulse width and a 1% duty cycle. Under CW operation, the threshold current was 2.7 mA, the differential efficiency was 4%, and the maximum output power was 256 μW for a lasing mode at 452 nm, defined with a spectrometer limited resolution of 2 nm. Under pulsed operation the threshold current was 3.4 mA, the differential efficiency was 3.1% and the maximum output power was 610 μW. This change in device performance is thought to be due to reduced alignment of the gain spectrum with the lasing mode in the absence of self-heating, where the lasing mode was redshifted by 9 nm relative to the peak of the spontaneous emission in pulsed operation. Although the spontaneous emission does not perfectly align with the gain spectra, the spontaneous emission peak was used as a proxy to estimate the position of the gain peak. The maximum output power under pulsed operation is a bit arbitrary as it just represents the hardest we pumped the device and not necessarily a device limited power. The pump conditions were limited to that point due to the high operating voltage and a fear of burning out the device. It was found that over time there was minor degradation in device performance when held under CW operation for tens of minutes. This can be seen by the slightly increased threshold current in Figure 5-8, of around ~4 mA. The mechanism for this has not yet been identified.

Thermal images taken with a QFI Infrascope at different input powers were used to estimate the thermal impedance of 1150 K/W, which was then used to estimate the active region temperature at peak output power of 90℃. This is slightly lower than the previously reported roll over temperature of 110℃ for semipolar devices with an ion implanted aperture.[155] COMSOL modeling of the device structure with the thermal conductivities used

when considering the IIA device, give a thermal impedance of 1200 K/W, an active region temperature at threshold of 52 °C, and a rollover temperature of 95 °C. This agrees fairly well with the thermal microscope images and the thermal impedance as measured by the spectra.

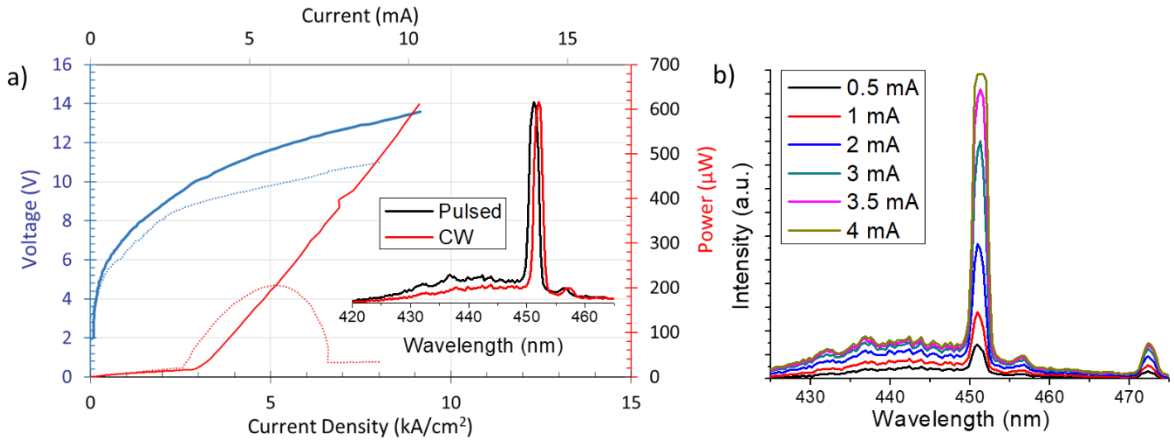

Figure 5-2. LIV (a) for pulsed (solid) and CW (dotted) operation of a 12 μm aperture VCSEL. The current density is calculated using the whole aperture area to more easily compare to other published results. For this device, the lasing area to aperture area ratio was 0.38. The inset spectrum (a) under pulsed and CW shows an approximate 1 nm redshift in the lasing mode from 451 nm to 452 nm at 3.5 mA due to heating during CW operation. The spontaneous emission redshifts by 3 nm. (b) Emission spectra as a function of injected current. It can be seen that the spontaneous emission ceases to increase with current for 3 mA and higher. This occurs in both the broad area peak, as well as the Fabry-Perot resonance at 472 nm. Conversely, the 452 peak continues to increase until saturating the detector at 4 mA. This is consistent with carrier clamping at threshold, and lasing[162].

5.1.1 BTJ Loss Analysis

Using a transmission matrix method (TMM) approach with the measured differential efficiency to estimate the sources of loss, as presented in Ref [155], there was an expected 6.5 cm^{-1} of internal loss, 0.7 cm^{-1} of mirror loss and almost 5 cm^{-1} of excess loss. The EBL design was improved for the BTJ devices by introducing a composition grade on the p-side to improve hole transport, as discussed be Mehta et al[153]. This likely improving the injection efficiency. If the assumed injection efficiency was increased to 80% from the 60% originally chosen, then the simulations suggest an additional loss of 8.5 cm^{-1}, similar to that in the ion implant structure

which could be due to loss in the DBRs and some roughness. The RMS roughness of several devices measured after substrate removal was unusually high, at over 3 nm. This rough surface would be expected to introduce significant scattering loss,[112] indicating that the observed improvement in device performance by using a BTJ could have been more significant if the roughness had been properly controlled. Since this level of loss is not observed in the loss analysis it is assumed that the AFM may have been done on uncharacteristically rough devices that don't properly represent the rest of the sample. Since the best devices on the sample are the ones that are analyzed, it is likely they are also the smoothest. However, they were likely still relatively rough compared to the optimized PEC etch test samples.

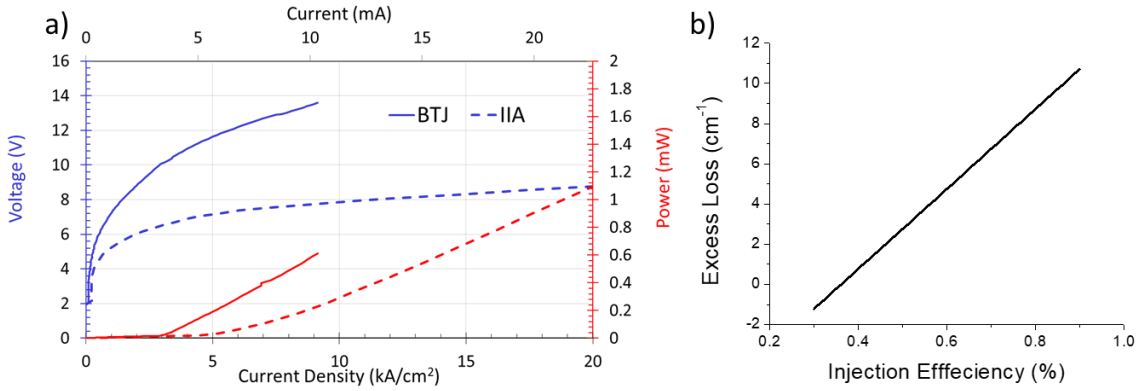

Figure 5-3. LIV (a) comparison of the BTJ devices with that of the IIA device under pulsed operation. This clearly chows the better LI characteristics and worse IV characteristics of the BTJ device. (b) shows how the assumed injection efficiency affects the calculated excess loss.

Figure 5-3 shows that the pulsed differential efficiency improved by 20% relative to previous semipolar devices with ion implant defined apertures, potentially due to a reduction of the absorption losses of the mode with absorbing regions outside the aperture in conjunction with an improvement in the injection efficiency by changing the EBL design.[155] Although the EBL was different, a change in injection efficiency doesn't fully account for the increase in the differential efficiency. Similar to previous results, the devices were 100% plane polarized along the a-direction.[77,155]

In addition to abnormally high roughness, these devices also suffered from high operating voltage that is believed to be due to incomplete activation of the buried p-type region. The sidewall activation was conducted at 625℃ for 20 min under N_2. Kuwano et al. have shown that activation at 625℃ under oxygen ambient for 30 min leads to c-plane LEDs which have only have been activated 30 μm into the mesa, and that the activation distance is proportional to the square root of the activation time.[154] Assuming a similar lateral activation rate on semipolar $(20\bar{2}\bar{1})$, the activation front would have been 25 μm from the edge of the mesa as seen in Figure 5-4, short of the edge of the aperture. Therefore, the aperture itself would not have been activated, which may explain the initial burn in that was required when testing these devices. Additionally, these devices were activated in a nitrogen ambient environment, which has been shown to be less effective than when oxygen is present.[163,164] Thus, using a longer activation time, a hotter activation temperature, and an air ambient should reduce the device voltage.

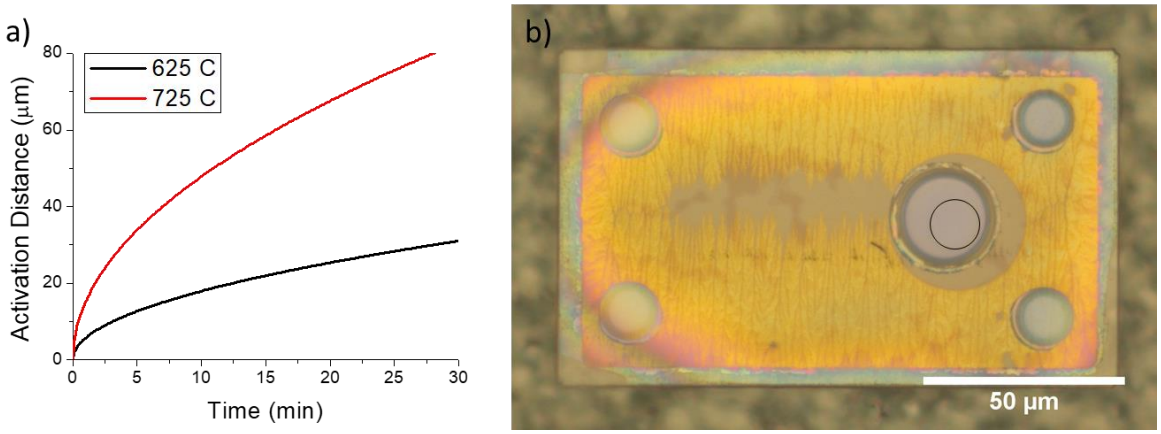

Figure 5-4. (a) Shows the activation distance as a function of annealing time for two different activation temperature, calculated from Kuwano et al.'s results[154]. (b) Shows an optical microscope image of a device after PEC etching. The aperture area has been circled in black and it is clear to see that 25 μm of activation is insufficient to activate the aperture area.

5.1.2 BTJ DBR Analysis

When analyzing samples, it is important to identify areas of suboptimal performance, and to plan for how to improve those areas in the future. A key design consideration for VCSELs lies in the compromise between threshold current density and differential efficiency. As the mirror loss is increased, the threshold gain is increased as well, thereby increasing the threshold current density. Conversely, the differential efficiency is positively related to the mirror loss. Thus, the optimal design configuration depends on the desired power output and current range. If another generation of BTJ devices is fabricated, it may be advantageous to increase the output power at the expense of the threshold current. The main parameter for changing the mirror loss is by changing the number of layer pairs in the out-coupling DBR to affect its reflectivity. Therefore, to try and increase the power of the BTJ devices, the effect of changing the number of periods in the top DBR on the output power for the BTJ and IIA samples was calculated using the reflectivity values found using TFCalc, and the gain curve found for semipolar edge emitting laser diodes with a similar active region. The effect of the number of DBR periods on the mirror loss, and thence the differential efficiency and the threshold gain was found. The threshold gain was used to find the threshold current density through

$$g_{th} = g_0 \ln(\frac{J_{th}}{J_{tr}})$$

where g_0=2187 cm^{-1} and J_{tr}= 0.47 kA/cm^2 [165]. The number of DBR periods also affects the total cavity length, changing more than just the mirror loss; however, it was found that this consideration had practically no effect on the simulated results. Thermal rollover was not considered as this simulation was intended to compare results found under pulsed injection. The power out of the devices with top DBR periods ranging from 8 to 16 was simulated up to

a current density of 30 kA/cm^2. The actual BTJ devices were only driven up to 10 kA/cm^2 due to the poor voltage characteristics of those devices which precluded surviving at higher current densities. However, the full simulated results have been presented, showing the potential improvements once the voltage is reduced.

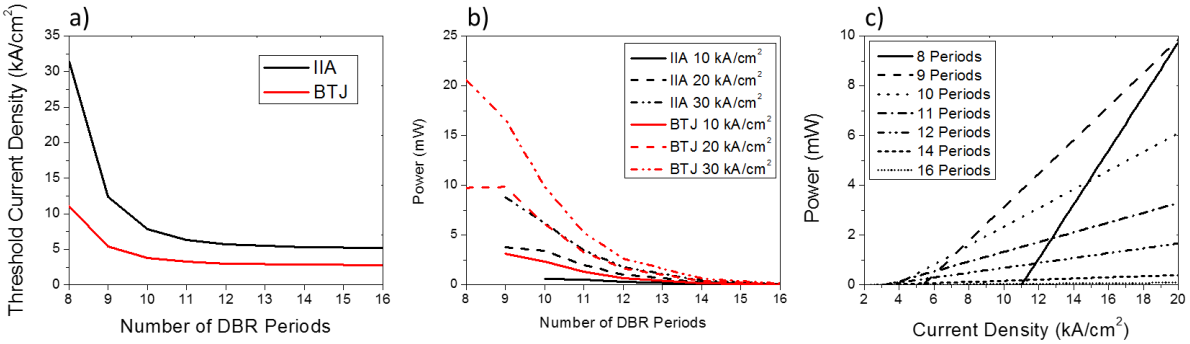

Figure 5-5. The simulated effect of changing the number of top DBR periods on the threshold current density (a) and the peak output power for different current injections (b). The simulated LI curves for the BTJ device (c), stopping at 20 kA/cm^2, show the increase in the threshold current density and differential efficiency for the devices with fewer mirror periods.

As can be seen in Figure 5-5(a), the threshold current density increases, potentially prohibitively, with fewer DBR periods for both samples. Figure 5-5(c), shows that as the number of periods is decreased the output power increases, up to a certain extent. For the BTJ devices, the output power with an 8 period DBR would be less than for a 9 period DBR at 20 kA/cm^2 due to the higher threshold current density of 8 period devices. Additionally, none of the 8-period ion implanted devices reached lasing under the current injections investigated. Moving to a 10 period DBR is expected to lead to a 270 % increase (4.4 mW) in the output power at 20 kA/cm^2 for the BTJ devices, and 220% (2.3 mW) for the IIA devices, while increasing the threshold current density by 28% and 40%, respectively.

5.1.3 Aperture Size Effects

Devices with apertures ranging from 6 μm to 16 μm were tested across the sample and the best devices for each aperture size were compared to study the effect of the aperture size on lasing

performance. Since there are many different ways for a device to be imperfect and degrade performance, but it is unlikely that a random deviation will cause the device performance to be better than it was designed to be, it was assumed that the best devices most accurately represented the device design. The best devices were defined as the devices with the lowest ratio of threshold current to differential efficiency. Upon initial inspection, as seen in Figure 5-6, the threshold current density steadily decreased with aperture size whereas the differential efficiency increase. This was not expected. For these devices, at least for the larger aperture ones where there should not have been significant edge effects; and under-pulsed operation where there significant heating was not anticipated, we would expect both lines to be independent of aperture area. As the aperture size decreases, and interactions of the mode with the edge of the aperture become more significant, then perhaps the threshold current density would increase and the differential efficiency would decrease due to higher losses. However, most of these devices have relatively large apertures so the edge effects were not anticipated to be significant.

An inherent assumption in finding the threshold current density is that the current is being uniformly injected into the aperture and only into the aperture. That assumption has been shown to be false a number of times in different indium phosphide based VCSELs[166,167]. To try and address this possible discrepancy, the current density was calculated using the extreme case of only having current injection into the area of the lasing modes. Thus, the current injection area is defined by the lasing area. Therefore, the threshold current densities were calculated using the lasing area. The lasing area was found from nearfield images and was defined as the area of each lasing spot over which the intensity was greater than $1/e^2$ of the spot peak, summed over all lasing spots within the aperture.

As seen in Figure 5-6(c), under the non-uniform current injection assumption the threshold current density was found to remain constant for aperture sizes greater than 8 µm. While, the 6 and 8 µm aperture sizes are still larger than what would be expected to have significant edge effects, there were few devices of those size that lased. Thus, the reliability of those points, especially the 6µm one is questionable.

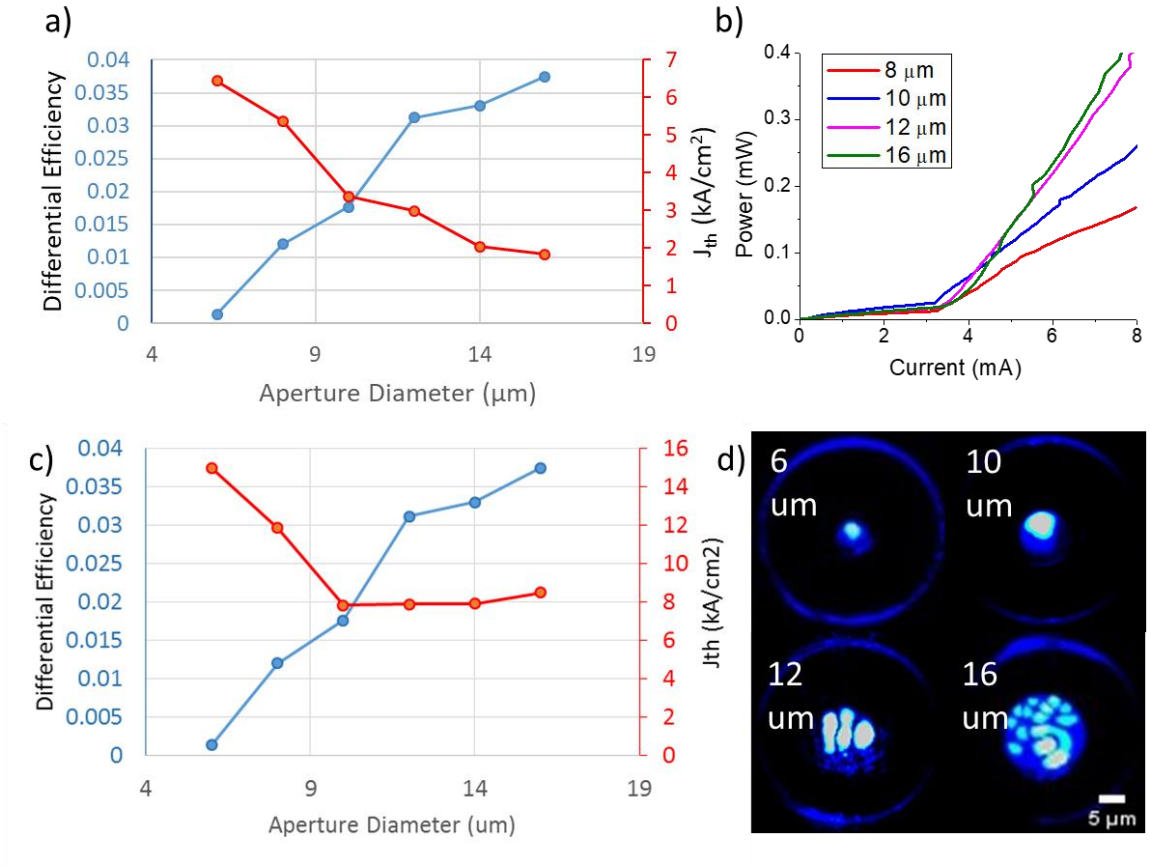

Figure 5-6. (a,c) Effects of aperture size on threshold current density and differential efficiency. The threshold current density is calculated using the aperture area (a) or the sum of lasing areas defined by $1/e^2$ of the respective peak intensities (c). (b) Shows the LI curves for several different aperture sizes. The nearfield images of a 6 µm, 10 µm, 12 µm, and 16 µm device (d) show examples of the filamentary lasing that is observed. These devices were operated under pulsed operation with a 1% duty cycle and a 1 µs pulse width. The same nearfield patterns were observed under CW operation. These patterns were not consistent between devices of a similar aperture size, though the presence of filamentary lasing was nearly universally present on all devices tested with larger apertures[162].

Unlike the threshold current density, the differential efficiency increased steadily with aperture size, as seen in Figure 5-6(a). The trend in the aperture size dependence of the differential efficiency was analyzed, but no conclusions were reached. However, the concept of injection efficiency relies on the assumption of uniform current injection. So, applying this concept to these devices is likely invalid, and may also be for most nitride VCSELs. Furthermore, it is difficult to accurately measure η_i, even in edge emitting laser diodes. In VCSELs, the task becomes much harder as the difficulty of reliably altering cavity length without introducing other issues is increased. Therefore, we have relied on η_i measurements from edge emitting lasers with a similar active region structure to estimate the injection efficiency for the VCSELs. Since the validity of the injection efficiency term in these VCSELs depends on the extent of current crowding, the aperture size is likely to change η_i, even for a constant active region design. As seen in Figure 5-7 (a), the ratio of lasing area to aperture area remained relatively constant up to the 10 μm, and then began to decrease. Assuming the "useful current" goes through the lasing area, it follows that the injection efficiency should decrease with decreasing ratio of lasing area to aperture size. This would suggest that the differential efficiency should increase with an increasing ratio, which is not observed in Figure 5-7 (b). As the current density per lasing area remains constant for the devices with apertures larger than 10 μm, it is expected that the injection efficiency at the lasing spots remains constant. This would suggest that the differential efficiency of each lasing area would be constant. However, as shown in Figure 5-7 (c) the efficiency increases with increasing lasing area.

Several other possible explanations were explored quantitatively, as follows. The edge of the BTJ introduces a height difference that propagates through the DBR, introducing lower mirror reflectivity at the periphery of the DBR due to layer thickness variation. Thus, the

percentage of the mode within 1 μm of the aperture edge was found for the different aperture dimensions as in Ref [155], and no trend was observed. The BTJ leads to an index step at the edge of the aperture that provides optical guiding but may also introduce unwanted losses. The difference in the cavity height between the aperture and the rest of the optical mode results in a modal wavelength shift between the two regions. In effect, the portion of the mode that extends beyond the aperture is not resonated outside the aperture, leading to loss. Thus, there is likely an optimum BTJ etch depth to promote optical guiding, while minimizing additional losses. No trend was observed when estimating the percentage of the mode that would be found outside the aperture, based on the measured light distribution. No trends were found in forward leakage currents or in the alignment of the lasing mode with the spontaneous emission. The mechanism for the steady increase in differential efficiency with both aperture size and lasing area is not understood at this time.

The nearfield images depicted in Figure 5-6(d) are representative devices from differing aperture sizes showing that as the aperture size increased the degree of filamentation did as well. Filamentation was observed in all aperture sizes but the 6 μm, though the proportion of devices that exhibited this behavior decreased with aperture size and allowed single mode emission in some cases. Thus, while the smaller aperture sizes showed degraded device performance and were not able to center the mode in the aperture, they were able to inhibit filamentation of the lasing mode and have single mode emission. Thus, if the smaller apertures are small enough to inhibit higher order modes, then they may indeed introduce greater edge effects than originally expected.

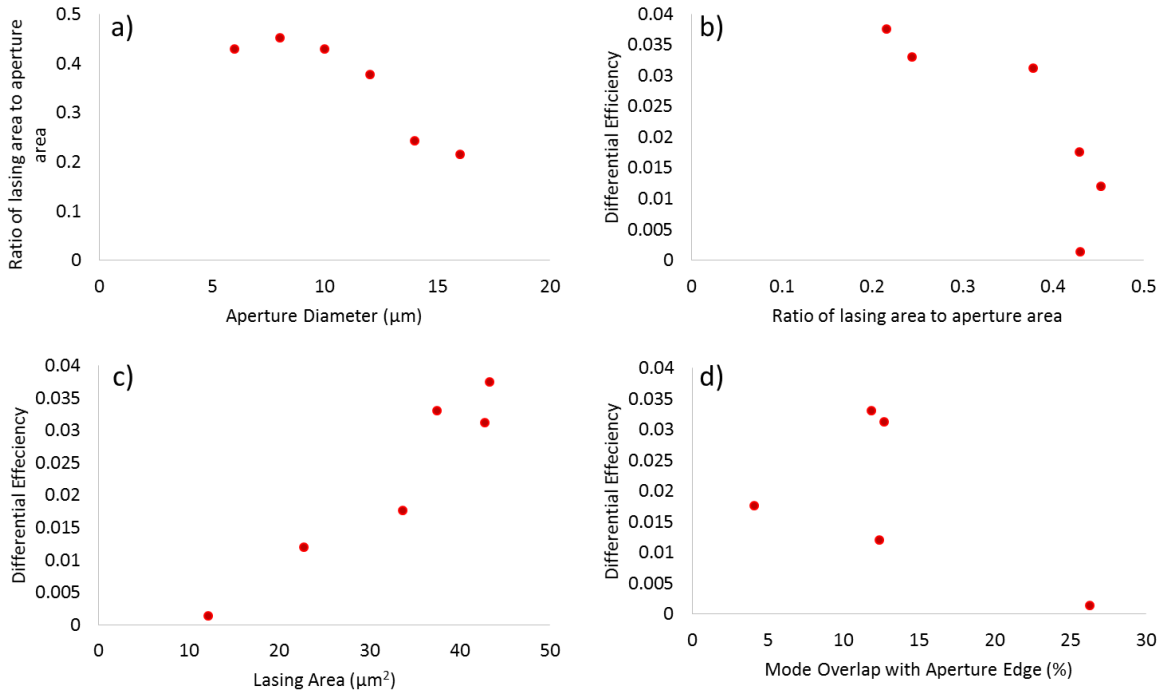

Figure 5-7. Shows the different attempts of understanding the trend in the differential efficiency. (a) depicts the ratio of the lasing area to the aperture area for each aperture diameter. The measured differential efficiency compared to the ratio of lasing area to aperture area unexpectedly decreased (b). The differential efficiency increased with the lasing area (c) and had little trend relative to the mode overlap with the aperture edge (d).

To consider why the smaller apertures rarely displayed filamentation, even when they are larger than the modes themselves the percentage of the aperture that was filled with a lasing mode was measured. For the aperture sizes of 6, 8, and 10 μm the percentage of the aperture filled with the lasing mode was ~40-45% from the calculated as the $1/e^2$ area. Determining which modes end up lasing is quite complex due to the variety of factors affecting the situation. In devices with perfect current spreading, both LP and HG modes can lase simultaneously, creating supermodes. However, in a real device, which modes actually lase depends on the degree of index guiding, as well as the gain and loss for each individual mode. This, in turn, depends on current spreading, proximity to aperture loss variation or mirror nonuniformity, and local contact or junction voltage. In general, smaller apertures increase the loss for filamentary or higher order modes with lobes near the edge. In the case of random current

nonuniformity, this issue can be more pronounced. For current hotspots that are randomly spaced across a sample, there is a higher probability of having multiple hotspots in the larger apertures. For two modes of 2 um diameter each to be clearly resolved, there needs to be ~4.5 um across of possible lasing area, so that the modes can be distinguished. Both of these modes also need to have similar levels of loss, so both of them need to be a minimum distance from the edge of the aperture. Filamentation was seen in diameters down to 8 μm, though the proportion of devices that exhibited this behavior decreased with aperture size. It is possible that with more devices to test, eventually a 6 μm aperture with filamentation would also be seen. It is also possible that multiple modes lased, but that they were close enough to not be clearly resolved.

5.2 Mode Profiles

When calculating the effect of aperture size on threshold current density above, it was postulated that the decrease in J_{th} was not a physical effect, but rather the outcome of an invalid injection uniformity assumption inherent in the calculation. To investigate this, nearfield images of the spontaneous emission were compared to images from a thermal imaging microscope at the same injection, as shown in Figure 5-8. The spontaneous emission profile is not uniform but has higher intensity of light being emitted from certain spots near the top of the aperture. The bright spots are not observed at very low current densities but do appear before lasing. This inhomogeneity in the emission profile suggests there may be non-uniform injection in certain areas of the aperture. The position of the lasing modes was found to correspond to the bright areas of the spontaneous emission, which, if depicting an area with higher current injection, would preferentially reach threshold gain. Additionally, thermal imaging, equipped with a silicon IR lens which blocks all visible light, shows higher

temperatures of operation roughly corresponding to the bright spots in the spontaneous emission, further supporting the idea of inhomogeneous current injection. Due to the 2 μm spatial resolution of the thermal microscope, and the high thermal conductivity of GaN, the thermal features are ill defined but recognizable.

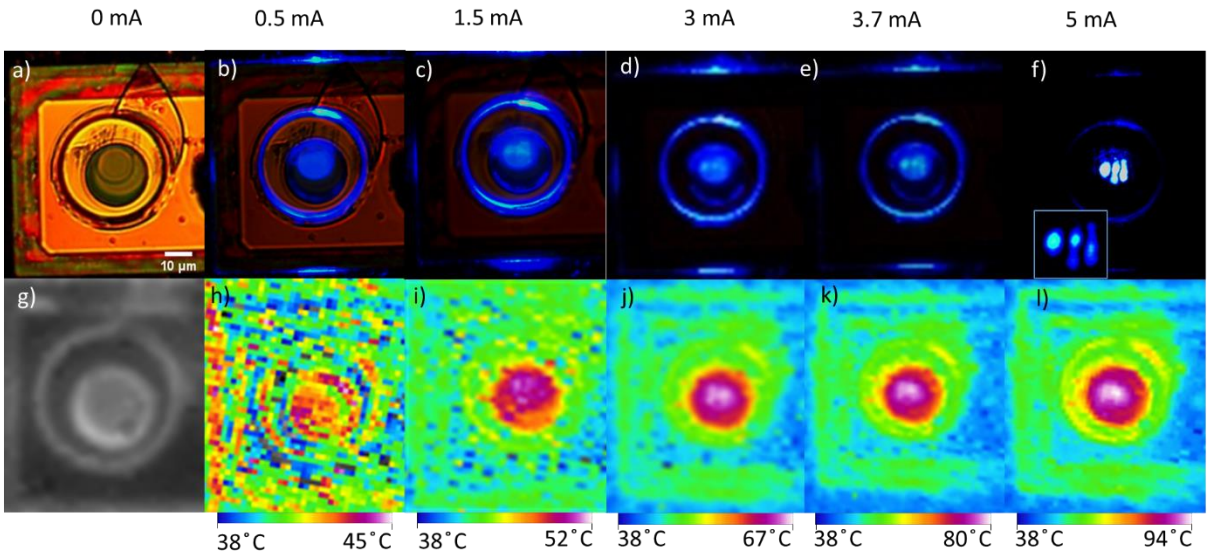

Figure 5-8. Nearfield images taken with an optical (a-f) and MWIR (g-l) camera at different drive currents of a 12 μm aperture device. The visible images were taken under pulsed operation, while the thermal images were taken under CW operation. Visible images of the devices under CW operation showed the same intensity non-uniformity[162]. © 2019 WILEY-VCH Verlag GmbH & Co. KGaA, Weinheim

As the injection current increased, the intensity contrast across the aperture, both thermally and optically, increased, suggesting a feedback mechanism to increase the current non-uniformity with increasing current. This progression in the emission intensity profiles, both visible and MWIR, suggests that the filamentary lasing that was observed is simply due to local current hot-spots providing higher carrier injection. Occasionally higher order cylindrical modes or supermodes of higher order modes were observed, as evidenced by several lasing spots turning on simultaneously, sometimes with other spots turning on at lower or higher current. This suggests that while current inhomogeneity was the dominant effect here, complex

mode structure arising from an interplay between index and gain guiding can also contribute, as has been previously reported.[90,127]

To further ensure that the observed variation in the optical nearfield images was due to current nonuniformity electron beam induced current (EBIC) images of a test device with a 20 um aperture and no top DBR were taken under forward bias, as shown in Figure 5-9. The test device had a structure similar to Ref [155]. EBIC uses a high energy electron beam to generate electron-hole pairs (EHP). If an electric field is present, then the carriers separate and a current is induced. Typically, the electric field is supplied by a junction, thereby allowing the actual depletion region to be mapped. In this case, an external bias of 2.8 V was applied across the device, sufficient to begin inducing a current. The generated electrons then travel to the active region and recombine with the injected holes from the anodic contact. The current variation across the aperture suggests a varying resistance, potentially due to inhomogeneity in the tunnel junction contact or the active region.

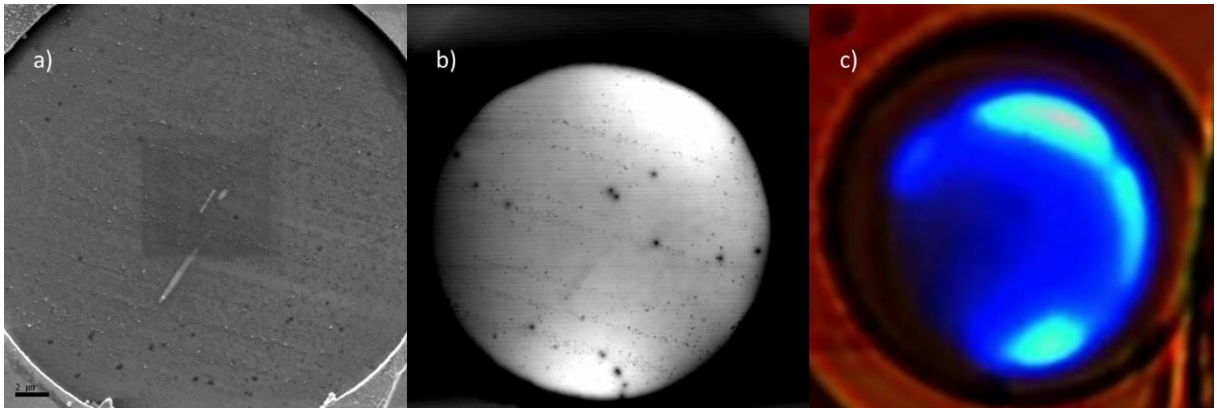

Figure 5-9. Secondary electron SEM image (a) of a 20 um aperture device at 5kV and 1.6 nA. The white lines in the aperture are carbon deposits due to the electron beam. The electron beam induced current image (b) shows inhomogeneous current across the aperture with an applied 2.8 V of forward bias. The current is well confined to the BTJ area. The large black dots likely correspond to dislocations and would represent a dislocation density of ~5×10^6 cm^{-2} which is reasonable for the freestanding substrates that were used. The small dots are due to surface contamination. The nearfield image (c) shows preferential emission from select areas of the aperture that correspond to the areas of higher current in the EBIC image.

At 2.8 V, 1 μA would be expected to flow under standard operation of the device. Using a 5kV beam, and assuming each EHP generation requires 3.4 eV, each incident electron generates over 1400 EHPs. Thus, for a beam current of 1.6 nA, if all generated EHPs contributed to an induced current explanation, over 2.3 μA would be induced. Therefore, the current generated from the electron beam is likely similar to that induced by the applied forward bias. The current signal roughly correlates to the nearfield intensity, supporting the idea that the variation in the spontaneous emission is due to current inhomogeneity.

5.2.1 Index guiding

For weakly guided modes, as is often observed in VCSELs, the effective index method can be used to find the refractive index difference between the core region below the aperture and the cladding region outside it by considering the difference in the resonant wavelengths between the two regions,

$$\frac{\Delta n_{eff}}{n_{eff}} = \frac{\Delta \lambda}{\lambda} = \frac{\Delta L}{L} \qquad \text{Eq. 5-1}$$

where Δn_{eff} is the effective index difference, n_{eff} is the effective index of the core, $\Delta\lambda$ is the resonant wavelength difference, λ is the resonant wavelength of the core, ΔL is the step height between the core and the cladding, and L is the effective cavity length[168]. The effect of optical guiding on the mode profile can be seen by comparing the modes observed in this work with two prior examples. When using a planar tunnel junction structure with an ion implant aperture and little optical guiding, Lee et al. observed filamentary lasing with little evidence of conventional higher order modes.[113] In a BTJ structure, the BTJ etch creates a cavity length difference between the aperture and the etched region, causing a difference in resonant wavelength. Therefore, the semipolar BTJ devices exhibited additional optical guiding and,

while still exhibiting filamentary lasing, showed more mode structure reminiscent of higher order modes than the planar tunnel junction structure. Finally, Lee et al. demonstrated m-plane BTJ VCSELs with complex optical modes that were at least well centered in the aperture and possessing symmetry related to conventional high order modes, shown in Figure 5-10.[126] The etch step in the m-plane devices, at 40 nm, was larger than the 30 nm etch for the semipolar samples. Additionally, the 6λ cavity of the m-plane devices was shorter than the 9λ of the semipolar. This gives a guiding effective index difference of 0.069 for the m-plane devices and 0.035 for the semipolar devices, showing that the index guiding for the m-plane samples was significantly higher. This is likely why the m-plane samples showed a greater prevalence of high order Hermite-Gaussian, Ince-Gaussian, or Lagurre-Gaussian mode structures. For both sets of devices, the degree of filamentation increased with aperture size. As both a more significant optical guiding and a thicker n-GaN current spreading layer produced more well defined modes, the claim that both injection uniformity and degree of optical guiding impact the modal distribution was supported.

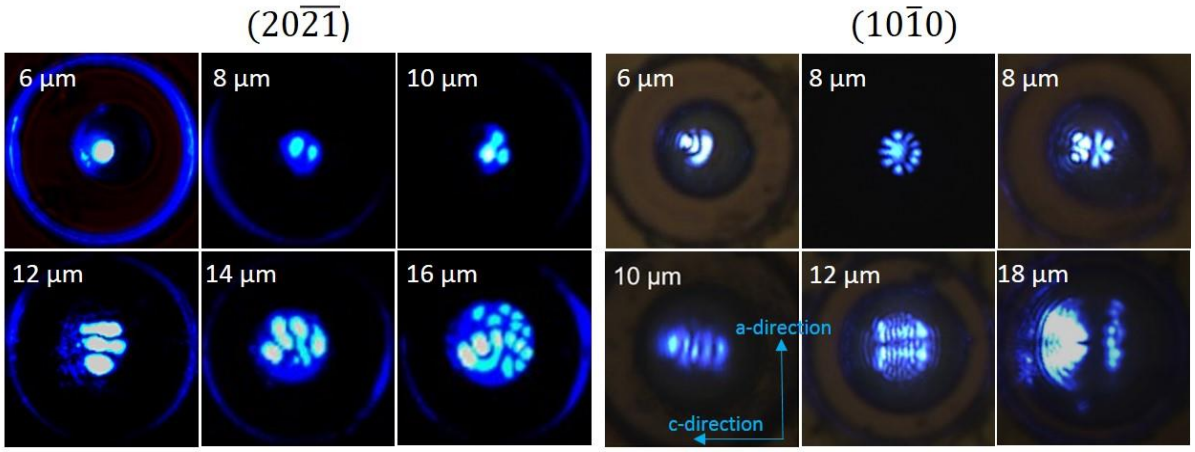

Figure 5-10. The modes displayed by the VCSEL with a lower index guided structure (left) generally showed less symmetry than those seen in the devices with a larger effective index step (right).

5.2.2 Burn-In

A final consideration for these devices is their stability during operation. Both the semipolar and the m-plane devices exhibited burn-in effects, where the electrical and/or optical properties changed over the first few cycles of operation. The semipolar VCSELs showed an improvement in electrical performance, with a 10% reduction of forward voltage after the first CW sweep, indicating that the temperature increase may have led to increased activation or opened up additional current pathways. This burn-in was required for pulsed operation.

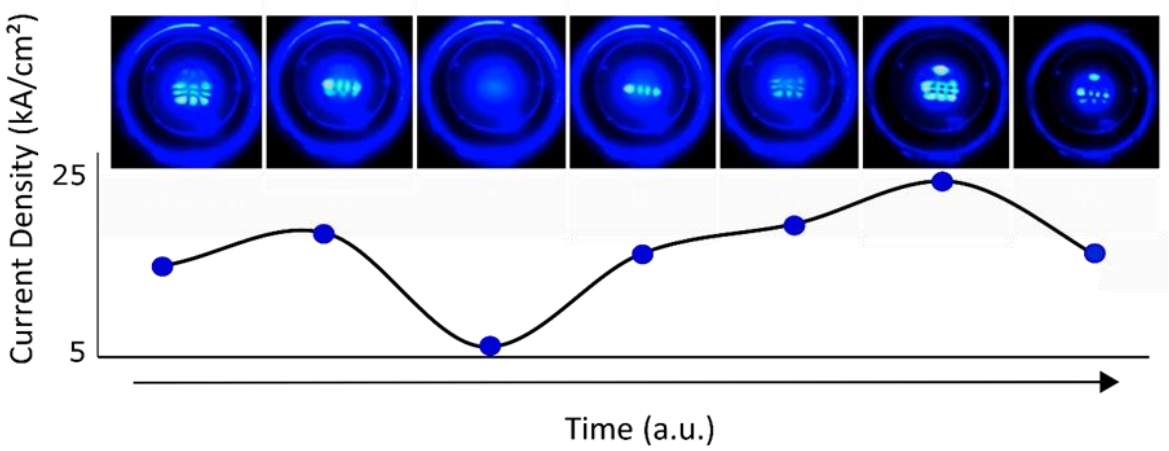

Figure 5-11. The nearfield images of an m-plane BTJ show how the mode shape changed as the current was increased over two sweeps.

Figure 5-11 depicts the changes in the lasing mode over the first two sweeps of an m-plane BTJ device. Initially a 3x3 mode was observed until the current was increased and a 1x4 mode appeared. When the current was decreased to below threshold, and then increased again, the 1x4 mode was the first to appear followed by the 3x3 mode. When the current was increased even more, an additional lasing spot appeared at the top of the aperture which stayed even when the current was decreased again. That final mode shape was seen in all further testing. The switching of the 3x3 and 1x4 modes is not understood at this time, though the appearance of the single spot is consistent with a new current path being burned in during operation that provides an area of locally higher current injection.

5.2.3 Current Nonuniformity

Since the source of the filamentation has been identified as inhomogeneous current injection, it would be advantageous to determine the source of the current injection issues. As the nearfield images did showed lasing modes in random locations, without significant preference for a certain position in the aperture, it can be concluded that the issue is not likely insufficient current spreading. If that were the case, then lasing only near the edge of the aperture would be expected. Since filamentary lasing has been seen on VCSELs with ITO [75,81,105,127], it seems unlikely that the current inhomogeneity is due to the n^{++}GaN layer in the tunnel junction, but is rather due to the top p-type layer or interfacial effects between the p-GaN and the current spreading layer.

The magnesium concentration used for the tunnel junction, and some ITO contacting layers, is higher than previously reported concentrations that induced Mg clustering[169,170], potentially inducing potential variations across the surface leading to non-uniform current injection. The high magnesium concentration was chosen to minimize the tunnel junction voltage drop and may represent a design tradeoff between device voltage and current uniformity. While the filamentary lasing may be solved by going to smaller aperture sizes, non-uniform current injection may lead to large device variability across a wafer. Preliminary studies by N. Palmquist using kelvin probe microscopy to measure the surface potential of a p^{++}GaN surface show potential variations not correlated with surface features as shown in Figure 5-12. Both the potential fluctuations inherent in the p-GaN and those due to surface contamination can affect the contact to the current spreader and lead to preferential current paths. However, a more rigorous study still needs to be done before any solid conclusions can be reached.

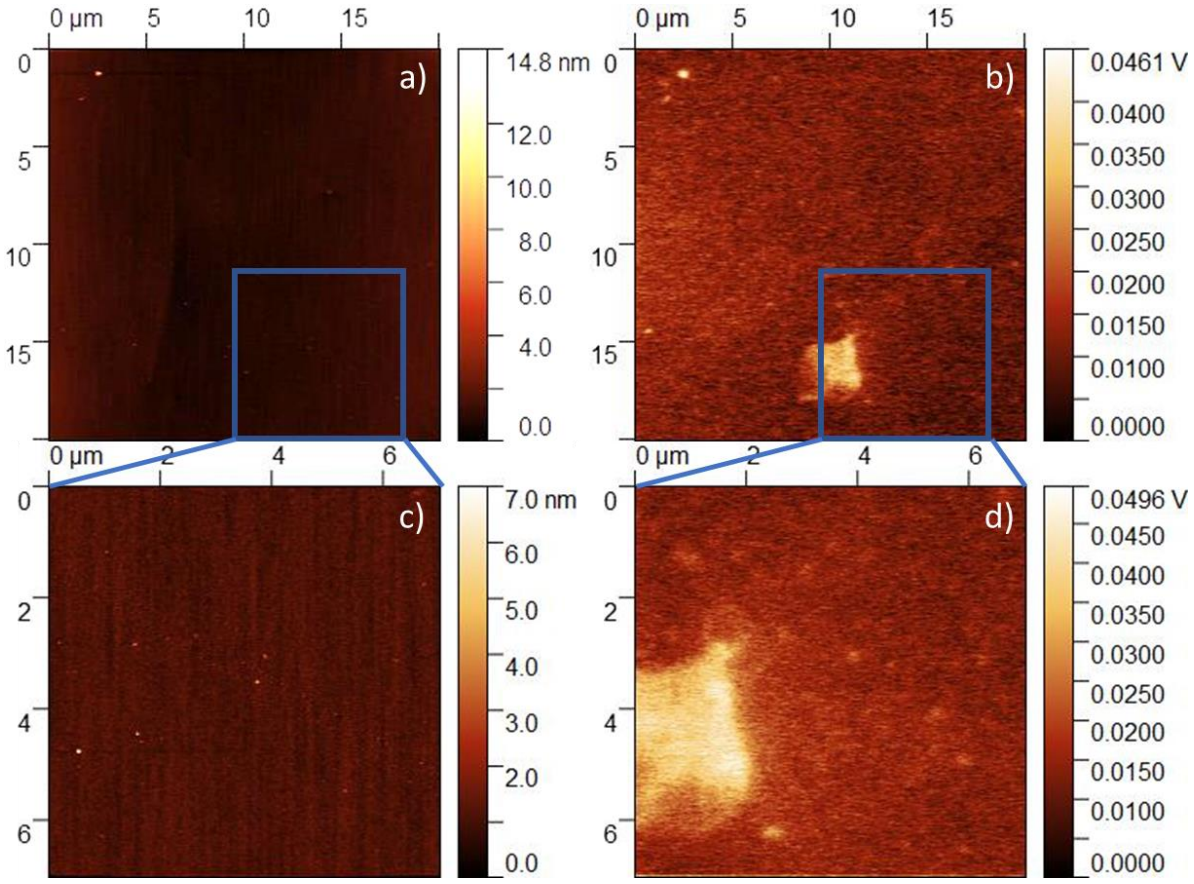

Figure 5-12. Kelvin probe atomic force microscopy images of the height trace (a,c) and the potential map (b,d) courtesy of N. Palmquist. The potential variations is shown by the bright and spots and could account for the difference in current between regions, assuming a uniform voltage drop. The particles on the sample surface shown in the height trace correspond so some of the potential variations, although not all. This suggests that there may be some combination of sample contamination before the current spreader deposition and issues with the p-GaN itself that lead to the current nonuniformity.

5.3 Conclusion

Overall, this prevalence of filamentation seen in the larger aperture devices seems to be largely influenced by an interaction of current nonuniformity and the index guiding of the cavity itself. This produces some combination of higher order modes or fundamental modes that are displaced from the center of the aperture. Since filamentary lasing has been seen on VCSELs with ITO,[75,81,105,127] it seems unlikely that the current inhomogeneity is due to the n^{++}GaN layer in the tunnel junction, but is rather due to the top p-type layer or interfacial effects between the p-GaN and the current spreading layer. Further research is needed to determine the root cause

of the current inhomogeneity. While the filamentary lasing may be circumvented by going to smaller aperture sizes, non-uniform current injection may lead to large device variability across a wafer or in an array.

6 Moving Forward

Initially, we wished to produce VCSELs that maintained many of the advantages that were inherent on m-plane but allowed for greater wavelength range. This led to the development of blue $(20\overline{2}1)$ semipolar devices. After optimizing the growth recipe and addressing the additional processing complexities associated with semipolar planes, the devices were fabricated with a similar design to that of the previous m-plane devices. The primary differences, aside from those associated with the crystal plane, were that the TJ was grown by MOCVD to reduce the roughness; the implant had a lower dose to limit potential optical losses; and the cavity length was shortened to increase the modal gain and decrease diffraction loss. This device showed significant improvements in performance compared to previous m-plane samples, though it didn't reach its full potential. There were several factors that contributed to increasing the loss in the physical devices compared to the model cavity. One important factor was the misalignment of the mode introducing significant optical loss. While these devices answered the initial question on pushing the wavelength farther, they also led to a new question, one of mode control.

BTJ devices structures have been used to great benefit in other material systems and provided a method for increasing the optical guiding by introducing a step height induced effective index contrast. Devices fabricated with this method were found to be lacking the additional optical absorption that was seen on the IIA samples, even when the mode was misaligned. Additionally, the ability to control the amount of index guiding in conjunction with multiple characterization methods enabled the identification of the odd mode behavior to be due to a combination of inhomogeneous current injection and index guiding. Although this device design provides a method for confining the mode, it is only one of many possibilities;

and although the source of the filamentation has been identified, the reason for the current crowding has not. Thus, answers only beget new questions and there is always more to learn.

There are multiple ways to progress this project, though I shall present three possibilities here and list a couple extraneous options at the end. The first approach would be to focus on trying to improve device performance. The BTJ devices showed promise but had a number of issues that limited their maximum output power and differential efficiency. The first issue to address would be the high operating voltage that likely led to significant heating of the devices and limited how hard they could be pumped. Likely this would require some combination of improving the activation parameters as well as improving the TJ regrowth and potentially optimizing the contact doping to limit the added voltage. This could be done by adding a thin InGaN layer at the TJ to increase the tunneling probability. Alternatively, MBE could be used to regrow the TJ. This was an issue for m-plane devices due to the roughness of the MBE regrowth. However, this is not an issue for $(20\overline{2}1)$.

In addition to reducing the voltage, improving the thermal performance of the device should increase the maximum output power achievable. This could be done by adding an optically transparent thermal spreading layer between the cavity and the p-DBR. Initial COMSOL simulations suggest that graphene would give minor improvement, but a thicker layer, such as diamond, could give significant improvements. This would also allow the device epi to be quite thin, potentially reducing the total loss in the cavity. A thin growth structure has the added advantages of being cheaper to produce, and potentially allows for the sacrificial wells to be close enough to the QWs such that a superlattice is no longer required. As the BTJ samples were measured to be unusually rough after PEC etching, processing a batch with improved morphology may improve performance. A final method that would improve the power through

the differential efficiency would be to experimentally vary the number of DBR periods of the top DBR and compare to the simulations presented above.

The next direction for future research would be to determine the source of the inhomogeneous current injection. To examine this, KP AFM could be done on some samples to map the potential variations in the p-GaN. Next, a TJ, ITO, and/or thin metal contact could be deposited to form a current spreading layer. The nearfield images of these devices could be compared to the potential maps to see the level of correlation. Once compared, EDX-TEM or APT could be performed to try and determine the source of the potential variations.

The third option would be to develop optical elements that would promote certain modes despite any current inhomogeneity. One potential way of addressing the poor mode control would be to include a separate optical aperture, instead of just relying on the gain guiding or index step of the current aperture. An optical aperture provides an enhanced index contrast between inside and outside the aperture. A proposed method to implement this in the current VCSEL design would be to deposit an AlN layer beneath the top DBR and perform a partial wet, lateral etch to introduce the index difference. The AlN would need to be optically transparent but could be amorphous and deposited by IBD and etched in concentrated KOH. Alternatively, using a curved mirror can allow for efficient mode control, as demonstrated by Sony.

Bringing these three paths together led to the idea of wafer bonding a sapphire cavity to the GaN epi and forming mirrors on either side. This would require the use of a curved mirror, but would allow for better thermal control, lower total loss, and better mode control. A design for this idea is presented further in Appendix A.4.

Finally, some additional ideas that could be helpful for future development or would just be interesting to know: measure the modulation speed of some semipolar VCSELs; use a higher resolution spectrometer to determine the number of separate frequencies lasing simultaneously and therefore how many modes are present during filamentation; measure the optical loss in the DBRs; attempt to further the wavelength through the use of a relaxed nanoporous DBR.

In the end, there have been numerous advances in multiple research groups recently leading to large improvements in performance. However, there are still large swaths of the design space that have not been explored prompting numerous paths for future development.

APPENDIX

A.1 Laser Physics and Modeling

A basic laser consists of a length of space confined by two mirrors to create a cavity, within which some length of the cavity contains an active material that provides gain when energy is injected[156]. This energy it typically administered with an external light source, or through electrical injection. Upon injection the light generated in the cavity is initially all spontaneous emission that is randomly emitted. However, as the intensity of light in the cavity increases, more and more stimulated emission occurs. This is characterized by one photon stimulating the emission of another photon such that both photons have the same phase, wavelength, polarization and direction. For photons travelling in most directions, this effect is minimal; however, this effect suggests that light which is reflecting between the mirrors could build with each pass. If the cavity is a multiple of the wavelength of emission in the cavity, then the light can constructively interfere and resonate. As the density of such photons bouncing back and forth between the mirrors increases, it will reach a threshold and start lasing. This threshold is characterized by several considerations. The first of which is that the *gain* from the stimulated emission of the active region is able to counterbalance the *losses* in the cavity due to light escaping, absorption in the cavity, scattering of the light, etc. Next, a population inversion occurs to the electrons in the active material. This means that the active region is being pumped hard enough that there are more electrons in an excited energy states than the lower. For semiconductor lasers that means there are more electrons in the conduction band than the valence band. A third consideration is that carrier clamping occurs, whereby the steady state carrier density in the active region does not increase with increasing drive current. This section

will cover some of the basic ideas and equations for describing lasers, with a focus on VCSEL considerations.

A.1.1 Laser Equations

To account for the fact that in most lasers, and certainly in electrically injected VCSELs, the active region does not take up the entire cavity, the average gain in the cavity is found through the definition of an enhancement factor, Γ. While, the active region itself may provide a material gain, g, at a certain injected power, the modal gain, Γg, must counterbalance the losses in the cavity to lase. The confinement factor can be split into three components

$$\Gamma = \Gamma_{xy}\Gamma_z\Gamma_{enh} \qquad \text{Eq. 0-1}$$

where Γ_{xy} is the transverse confinement factor, Γ_z is the axial confinement factor, and Γ_{enh} is the enhancement factor. Γ_{xy} takes into account the overlap of the mode with the aperture and is generally assumed to be near one for VCSELs. Γ_z considers the thickness of the active area relative to the entire cavity and is calculated by

$$\Gamma_z = \frac{L_a}{L_c} \qquad \text{Eq. 0-2}$$

where L_a is the length of the active material along the axial direction, and L_c is the length of the entire cavity.

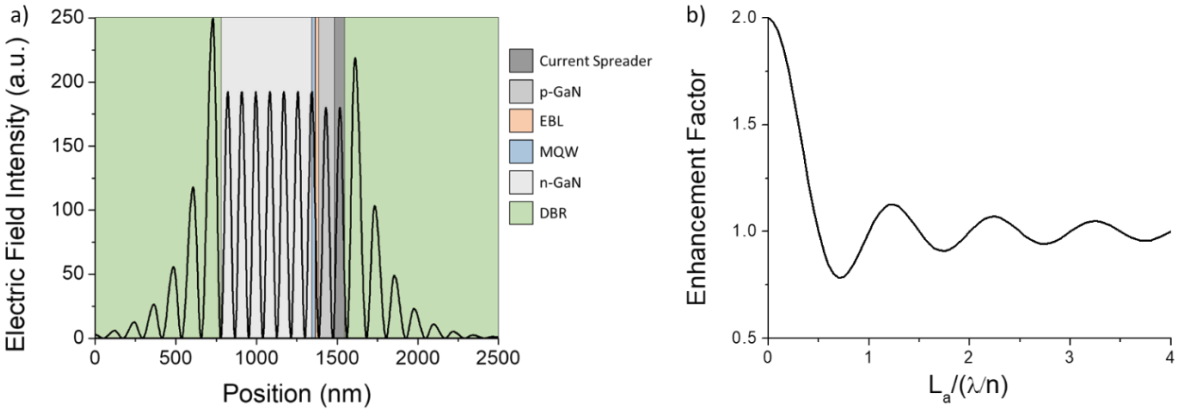

Figure 0-1 Shows an example of the electric standing wave in a cavity (a) and how the enhancement factor changes with layer size (b)

Finally, the enhancement factor accounts for the position of the gain medium relative to the standing wave of the electric field in the cavity and can be found by[156]:

$$\Gamma_{enh} = \frac{\int_{L_a} |E(z)|^2 \, dz}{\Gamma_z \int_{L_c} |E(z)|^2 \, dz} \approx 1 + \frac{\sin(\beta L_a)}{\beta L_a} \qquad \text{Eq. 0-3}$$

where E is the electric field standing wave and β is the effective propagation constant of the mode, which is given by $2\pi n/\lambda$. The approximate solution is only valid if the center of the layer of interest aligns with the center of a standing wave peak. As seen in Figure 0-1 the maximum value this can take is two for a perfect alignment of an infinitely small active region aligned to the standing wave antinode. To minimize the material gain that is required for lasing, it is desired to maximize the enhancement factor of the active region.

The condition for the round trip gain to equal the loss in a cavity with mirror reflectivities of R_1 and R_2 is expressed by[168]:

$$R_1 R_2 e^{2\Gamma_{enh} g_{th} L_a - 2\alpha_i L_c} = 1 \qquad \text{Eq. 0-4}$$

The internal loss, α_i, due to absorption is found by:

$$\alpha_i = \frac{\sum_l \alpha_l L_l \Gamma_{xy,l} \Gamma_{enh,l}}{L_c} \qquad \text{Eq. 0-5}$$

where the summation is over all layers in the cavity and the enhancement factor for each layer weights the losses by their overlap with the standing wave. Thus, it is advantageous to align layers with high absorptivity, with the null of the standing wave to minimize the total loss in the cavity. In a real device, α_i is adjusted to include scattering loss, diffraction loss, and any other sort of loss that is not mirror loss. In Chapter 4 this adjustment is termed the excess loss. Rearranging Eq. 0-4 gives that the modal gain is equal to the sum of the internal loss and the mirror loss, α_m.

$$\Gamma g_{th} = \alpha_i + \frac{1}{L_c} \ln\left(\frac{1}{\sqrt{R_1 R_2}}\right) = \alpha_i + \alpha_m \qquad \text{Eq. 0-6}$$

In a device where the confinement factor is low, such as a VCSEL, it is important to minimize losses. The internal loss can be minimized by using layers with low optical absorption and aligning the more absorbing layers with the null of the optical standing wave. Despite its positive impact on differential efficiency and output power, the mirror loss also needs to be small to allow for lasing. This necessitates the use of highly reflective mirrors, often distributed Bragg reflectors (DBRs), on both sides of a VCSEL for it to work.

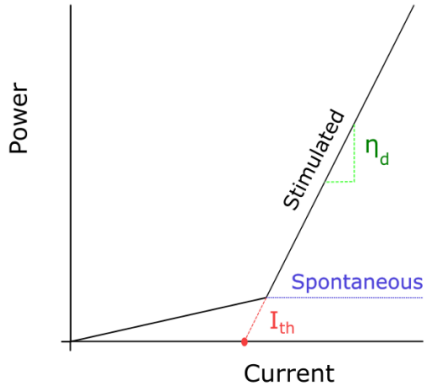

Figure 0-2 A simplified LI curve shows the "kink" at threshold.

To determine the threshold current density for an electrically injected device, a couple more relations are needed. First of all, the peak of the gain spectra can be approximated as being proportional to the natural log of the carrier density in the active region[168]. The threshold current density, J_{th}, is related to the threshold carrier density, n_{th}, by[156]:

$$J_{th} = \frac{qL_a}{\eta_i \tau_r} n_{th} \qquad \text{Eq. 0-7}$$

where q is the elementary charge, η_i is the injection efficiency, and τ_r is the recombination lifetime. The recombination lifetime is given by

$$\frac{1}{\tau_r} = -\frac{1}{n}\frac{dn}{dt} = A + Bn + Cn^2 \qquad \text{Eq. 0-8}$$

for the non-radiative surface or trap-assisted recombination coefficient, A, radiative bimolecular recombination, B, and Auger recombination coefficient, C. The A and C coefficients describe the non-radiative processes that affect the lifetime in the active region. If the B coefficient dominates at threshold,

$$J_{th} \approx B\frac{qL_a}{\eta_i} n_{th}^2 \qquad \text{Eq. 0-9}$$

Using the relationship between the carrier density and the gain, we get:

$$J = J_{tr} e^{\frac{g}{g_o}} \qquad \text{Eq. 0-10}$$

with a material dependent constant g_o, and the transparency current density J_{tr}. Transparency occurs when the active region net gain is zero. It is generally very difficult to measure the J_{tr} and g_o for a VCSEL active region. Thus, they are measured with edge emitting lasers, and then the values are assumed to apply to VCSELs with a similar structure.

Once lasing has been identified, several properties of the device can then be measured. A typical laser power-current (LI) curve is shown in Figure 0-2, where it is easy to see the difference in slope at the transition to lasing. The curve corresponding to the lasing emission can be given by

$$P = n_i \left(\frac{a_m}{a_i + a_m} \right) \frac{h\nu}{q} (I - I_{th}) = n_d \frac{h\nu}{q} (I - I_{th}) \qquad \text{Eq. 0-11}$$

where P is the output power, η_d is the differential efficiency, h is Plank's constant, ν is the frequency of the lasing emission, I is the current, and I_{th} is the threshold current. This equation provides the basis for the experimental determination of the threshold current and the differential efficiency by applying a linear fit to the LI data just above threshold. However, often only the power out of one side of the device is of interest. Thus, a parameter, F, is used to denote the percentage of output power from a certain side of the device. The proportion of the power that is emitted by one mirror can be found by:

$$F_1 = \frac{t_1^2}{\left(1 - r_1^2\right) + \frac{r_1}{r_2}\left(1 - r_2^2\right)} \qquad \text{Eq. 0-12}$$

where $r_1$is the reflectivity of the mirror of interest, r_2 is the other mirror reflectivity, and t_1^2 $=1-r_1^2$ for a lossless mirror. The reflectivity of the mirrors can be calculated using the transmission matrix method, as discussed below.

A.1.2 TMM Calculations

Many of the parameters describing a VCSEL depend on the electric field in the cavity. To model the cavity structure a transmission-matrix method can be used to calculate the effect of different cavity designs on parameters of interest. Here the focus will be on calculating the

cavity gain and losses. To begin, consider light incident on some element that will allow some amount of transmission and cause some level of reflection.

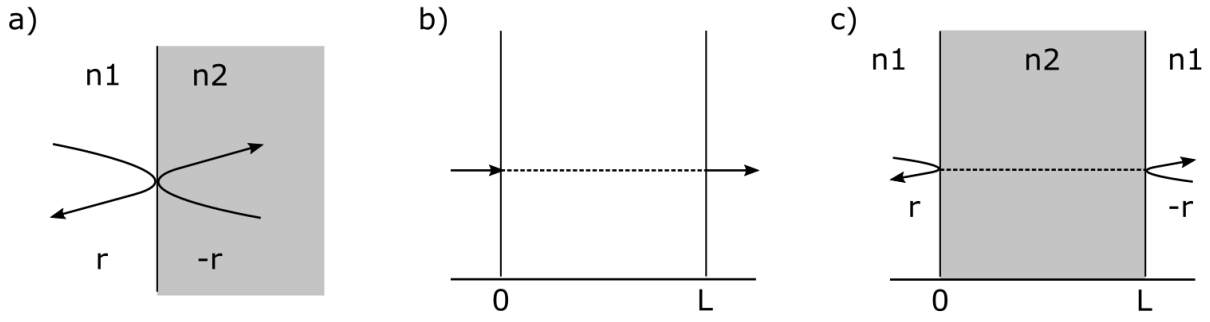

Figure 0-3 Shows the geometry that forms the reflection matrix (a) and the propagation matrix (b), that lead to the full layer matric (c).

The interaction can be described by a transmission matrix, T[156],

$$\begin{bmatrix} A_1 \\ B_1 \end{bmatrix} = \begin{bmatrix} T_{11} & T_{12} \\ T_{21} & T_{22} \end{bmatrix} \begin{bmatrix} A_2 \\ B_2 \end{bmatrix} \qquad \text{Eq. 0-13}$$

where A describes the light propagating to the right, and B corresponds to waves propagating to the left.

If the element that the light interacts with is a simple interface between two different media with refractive indices of n_1 and n_2, as seen in Figure 0-3(a), then the **T** matrix of the interface can be written in terms of the reflection coefficient, r, and the transmission coefficient, t.

$$T_I = \frac{1}{t} \begin{bmatrix} 1 & r \\ r & 1 \end{bmatrix} \qquad \text{Eq. 0-14}$$

The reflection coefficient is given by the relative difference in the refractive indices for a normal incident plane wave

$$r = \frac{n_1 - n_2}{n_1 + n_2} \qquad \text{Eq. 0-15}$$

Using power conservation, it can be seen that

$$r^2 + t^2 = 1 \qquad \text{Eq. 0-16}$$

Therefore, the following relation can be written for the transmission coefficient at an interface

$$t = \sqrt{1-r^2} = \frac{2\sqrt{n_1 n_2}}{n_1 + n_2} \qquad \text{Eq. 0-17}$$

Another common interaction element would be the continuous transmission of light through a medium, as shown in Figure 0-3(b). The **T** matrix for this is given by

$$T_L = \begin{bmatrix} e^{i\tilde{\beta}L} & 0 \\ 0 & e^{-i\tilde{\beta}L} \end{bmatrix} \qquad \text{Eq. 0-18}$$

where L is the length of the transmission section, and $\tilde{\beta} = \beta + i\beta_i$ is the complex propagation constant. The benefit of describing interactions with **T** matrices is that they can be used to describe a complex system by sequentially multiplying the **T** matrices of individual segments. Thus, for a system which can be broken down into j components of repeating interfaces and continuous transmission, the system **T** can be found by:

$$T_{final} = \prod T_j \qquad \text{Eq. 0-19}$$

As an example, a system containing an interface followed by a transmission section, as shown in Figure 0-3(c), can be described by the product of the two aforementioned matrices and give:

$$T = \frac{1}{t}\begin{bmatrix} e^{i\tilde{\beta}L} & re^{-i\tilde{\beta}L} \\ re^{i\tilde{\beta}L} & e^{-i\tilde{\beta}L} \end{bmatrix} \qquad \text{Eq. 0-20}$$

To find the power reflectivity, R, of the entire structure[171],

$$R = \left| \frac{T_{21}}{T_{11}} \right|^2 \qquad \text{Eq. 0-21}$$

can be used over a range of wavelengths to produce calculated plots similar to Figure 2-3 (a). This method gives the mirror reflectivity values to be used in Eq. 0-12

Given a structure with j layers total, the electric field in a layer, k, of the structure can be found by dividing the structure into two subsets, one on either side of layer k, such that to total system transfer matrix is:

$$T_{total} = T_k^{'} T_{L,k} T_k^{"} \qquad \text{Eq. 0-22}$$

where T_k' is the **T** matrix for all layers up to k, including the k/(k-1) interface, and T_k'' is the **T** matrix for all layers after k, including the k/(k+1) interface. $T_{L,k}$ is the continuous transmission matrix for layer k.

$$T' = \left(\prod_{n=1}^{k-1} T_{I,n} T_{L,n} \right) T_{I,k} \qquad \text{Eq. 0-23}$$

$$T'' = \left(\prod_{n=k+1}^{j} T_{I,n} T_{L,n} \right) T_{I,j+1} \qquad \text{Eq. 0-24}$$

The full derivation can be found in Ref [171], where it is shown that the electric field in the layer k, with a length L_k, varies with position, x, as described by:

$$E_k(x) = \frac{T_{k11}^{"} e^{-i\tilde{\beta}(L_k - x)} + T_{k21}^{"} e^{i\tilde{\beta}(L_k - x)}}{T_{k11}^{'} T_{k11}^{"} e^{-i\tilde{\beta} L_k} + T_{k12}^{'} T_{k21}^{"} e^{i\tilde{\beta} L_k}} \qquad \text{Eq. 0-25}$$

6.1.1.1 DBR Mirror effective length

Now that we have laid the framework of the TMM, we can look at VCSEL mirrors. The DBR mirrors used with many VCSELs are made up of successive layers with high and low refractive indices. Thus, they are a periodic set of interfaces and transmission segments that build up reflections to collectively produce a mirror with a high reflectivity.

To simplify the consideration of the DBRs in a full VCSEL simulation, they can be modelled as a discrete reflection set at an effective distance from the cavity. This means that

the total cavity length in the device is longer than just the region between the DBRs, but shorter than the whole device. For optimal performance, each layer of the DBR would be quarter-wave thick. Often the actual devices are intentionally or unintentionally detuned such that the lasing mode is not exactly aligned with the center of the DBR reflectivity. However, that detuning encountered in III-N based VCSELs is often not intentionally significant, so most of the following equations will apply for devices operating at or near the Bragg condition of the DBRs. An average period length, Λ, can be defined based on the refractive indices of the two layers[156],

$$\Lambda = \frac{\lambda}{4}\left(\frac{1}{n_1}+\frac{1}{n_2}\right) \qquad \text{Eq. 0-26}$$

To determine the effective penetration depth, L_{eff}, into the DBR, the actual number of DBR periods, m, can be converted into an effective number of DBR periods, m_{eff}.

$$m_{eff} = \frac{\tanh\left(m\ln\left(\frac{n_2}{n_1}\right)\right)}{\tanh\left(\ln\left(\frac{n_2}{n_1}\right)\right)} \qquad \text{Eq. 0-27}$$

This can then be used, in conjunction with the reflectivity of the interface between the two DBR materials, r, to find the effective penetration depth into a DBR.

$$L_{eff} = \frac{1}{2}m_{eff}\Lambda\left[\frac{1}{1+r^2}-\frac{1}{2m_{eff}}\right] \qquad \text{Eq. 0-28}$$

In a device, this length can be calculated for each DBR to add to the epitaxial layer thicknesses, L_{epi}, to determine the total cavity length that is used in the laser modelling equations.

$$L_c = L_{epi} + L_{eff,1} + L_{eff,2}$$ Eq. 0-29

A.2 IIA Process Follower

160203 VCSEL Process Flow - IIA,PECA,BTJ+TJ or ITO		
Authors: Jared Kearns, Charles Forman, and John Leonard		
General Prep	PR Bench	Prep PRs and check experation date
		SPR220-3.0
		SPR220-7.0
		nLOF2020
		nLOF2035
Calibration (Day 1)	MOCVD	Grow xrd and emission wavelength callibrations for all relevant layers in the device
Calibration (Day 2)	XRD	Analyze XRD callibaration samples using ~30 min 2-theta/omega scans (6-8hrs XRD time)
		Fit the XRD data by simulating the structure and adjusting the parameters by hand, until a good fit is obtained
	Quicktest	Deposit In dots by rubbing through a shadowmask and soldering back contacts. Conduct LIV testing to find the wavelength, power, and voltage
	Computer	Adjust the growth times and QW temperatures on the layers of interest in all the recipes. λEL>λFP is not desirable (i.e. λEL<λFP or λEL=λFP is prefered). λsacrificial>405nm is required for PEC etching. λsacrificial>420nm is required for observation under Fluorescence microscope and for usinf the 420 nm lamp
Growth (Day 3)	MOCVD	Grow the desired VCSEL Series
Begin Processing (Day 4)	Furnace	600C, Air, 15min
	Quicktest	Measure Quicktest data for the VCSELs. Save all spectrum and IV data. Regrow if power or voltage is bad
Remove Indium	Acid Bench	3:1 HCl:HNO3 Aqua Regia, 3x 10min, mix new batch each iteration, wait 5min for boiling, 120C on hotplate. End with DI+Tergitol clean, N2 dry. Inspect and do again if needed
Mesa 1 Litho	Solvent Bench	Sonicate on high: 3min Ace, 3min Iso, 3 min DI, 4x DI Dump&Rinse, N2 dry
	PR Bench	Dehydration bake, 2min 110oC, let cool 30sec
		Spin HMDS Program 5 (3000rpm, 30s)
		Spin **SPR220-3.0** Program 5 (3000rpm 30s)
		edge-bead removal from short edges
		Soft bake, 115oC 90s
	Contact Aligner	Expose **"Mesa 1"**, 7.5mW/cm2, **25s,** No Filter, Black chuck, **Hard contact**
	Develop Bench	**Post expsure bake 115°C 60s**
		Develop in AZ300MIF **60s**
		4x DI rinse flowing, N2 dry

	Microscope	Inspect, develop more if necessary
	PEII	O2 plasma descum, 300 mT, 100 W, 30sec
Mesa 1 Etch	RIE5	Load bare carrier wafer
		Standard O2, BCl3/Cl2 preclean (Kearns_01 (~10min pump down, 10min O2 clean))
		Load samples onto carrier wafer, no oil
		Dan_05 (120 nm/min) (etch past active QW but stop >200 nm above SacQWs)BCL3 (10sccm, 10mT, 100W, 2min), Cl2 (10sccm, 5mT, 200W, 5 min)
	Solvent Bench	Preheat 1165 Stripper for 10 min, 80 C
		Sonicate on High at 80C for 10min. Rinse 4x DI, N2 dry, inspect, do acidic piranha if necessary to remove etch residue
Aperture hardmask Litho	Solvent Bench	Sonicate on high: 3min Ace, 3min Iso, 3 min DI, 4x DI Dump&Rinse, N2 dry
	PR Bench	Dehydration bake, 2min 110oC, let cool 30sec
		Spin HMDS Program 5 (3000rpm, 30s)
		Spin **nLOF2020** Program 5 (3000rpm 30s)
		edge-bead removal from short edges
		Soft bake, 110oC 90s
		Expose **"Aperture"**, **10s**,7.5mW/cm2, No Filter, Black chuck, **Hard contact**
		Post exposure bake 110oC 60s
		Develop in AZ300-MIF **50s**
		4x DI rinse flowing, N2 dry
	Microscope	Inspect, develop more if necessary
Hardmask Deposition	**Ebeam 3**	Deposit Ti/Au 200A (1A/s)/ 2000A (1A/s→100A,3A/sec→500A, 6A/sec→2000A)
	Solvent Bench	Preheat 1165 Stripper for 10 min, 80 C
		Soak 80C for 15 min. Spray with pipette, Rinse DI, N2 dry
	Microscope	Inspect, liftoff more if necessary
Define Aperture	Leonard Kroko, Inc	Ship samples to Leonard Kroko
		wafer size: ~1cm2
		Ion: Al, Dose: 10^14 ions/cm2, Energy: 20 keV, Normal incidence
		~3-4 day turn-around
	Acid Bench	3:1 HCl:HN03 Aqua Regia, 3x 10min, mix new batch each iteration, wait 5min for boiling, 120°C on hotplate. End with DI clean, N2 dry
	3D Microscope	Inspect, strip more if necessary
Intracavity Contact: TJ	HF Bench	5 min BHF
	MOCVD	TJ re-growth. Model the structure in VERTICAL to get correct thickness.
	AFM (optional)	Measure intracavity contact RMS roughness (5um x 5um scan)
TJ Etch Litho	Solvent Bench	Sonicate on high: 3min Ace, 3min Iso, 3 min DI, 4x DI Dump&Rinse, N2 dry

	PR Bench	Dehydration bake, 2min 110oC, let cool 1min
		Spin **SPR220-3.0** Program 5 (3000rpm 30s)
		edge-bead removal from short edges
		Soft bake, 115C 90s
		Expose "**Intracavity-Dielectric**", **25s**,7.5mW/cm2, No Filter, Black chuck, hard contact
		Post exposure bake 115oC 60s
		Develop in AZ300-MIF 60s undercut
		4x DI rinse flowing, N2 dry
	Microscope	Inspect, develop more if necessary
	PEII	O2 plasma descum, 300 mT, 100 W, 30sec
TJ Etch	**RIE5**	Load bare carrier wafer
		Standard O2, BCl3/Cl2 preclean (Kearns_01 (~10min pump down, 10min O2 clean))
		Load samples onto carrier wafer, no oil
		Dan_05 (120 nm/min) (Etch through p++GaN not through Sac QWs. BCL3 (10sccm, 10mT, 100W, 2min), Cl2 (10sccm, 5mT, 200W, 2.5 min) Change CL2 etching time
	MOCVD Lab	Activate again, 675C 20 min, **step still needs to be optimized**
	Solvent Bench	Preheat 1165 Stripper for 10 min, 80 C
		Sonicate on High at 80C for 10min. Rinse 4x DI, N2 dry
	3D Microscope	Inspect, strip more if necessary, do acidic piranha if necessary to remove etch residue
p-DBR Litho	Solvent Bench	Sonicate on high: 3min Ace, 3min Iso, 3 min DI, 4x DI Dump&Rinse, N2 dry
	PR Bench	Dehydration bake, 2min 110oC, let cool 1min
		Spin **LOL 2000**, 2000 rpm, 10 krpm/s, 30s (~250 nm thick)
		Softbake, 170 °C, 5min, let cool 2 min
		Spin **nLOF2035** Program 5 (3000rpm 30s)
		edge-bead removal from short edges
		Softbake, 110oC 90s
	Contact Aligner	Expose **"p-DBR"**, 7.5mW/cm2, **10s**, No Filter**,** Black chuck, **Hard contact**
	PR Bench	**Post exposure bake 110C 60s**
	Develop Bench	Develop in AZ300MIF **50s+10s** undercut
		2min DI rinse flowing, N2 dry
	Microscope	Inspect, develop more if necessary
	PEII	O2 plasma descum, 300 mT, 100 W, 30sec
p-DBR Dep	IBD	Calibration Sample(s) using DSP sapphire ans Si, Ellipsometer/Filmetrics, JL_FP_1i5pTa2O5… ,JL_12_FP_1i5pSiO2…
		Deposit 16 periods SiO2/Ta2O5, Co-load a DSP sapphire 1/4 wafer
	FT-10R	Measure and Model reflectance on SSP sapphire sample
	Solvent Bench	Preheat 1165 Stripper for 10min, 80oC
		Sonicate on low at 80C for 10min. Rinse 4x DI, N2 dry

	3D Microscope	Inspect, liftoff more if necessary
Mesa2 Etch Litho	Solvent Bench	Sonicate on low: 3min Ace, 3min Iso, 3 min DI, 4x DI Dump&Rinse, N2 dry
	PR Bench	pre-heat hot-plate to 50C
		Dehydration Bake, 2min 110oC, let cool 1min
		Spin HMDS Program 5 (3000rpm, 30s) **(Use DSP Sapphire Corrals)**
		Spin **SPR 220-7.0** Program 5 (3000rpm 30s) (~7µm)
		edge-bead removal from short edges
		Soft bake, 115C 120s
	Contact Aligner	Expose **"Mesa2",** 7.5mW/cm2, No Filter, Black chuck, **Hard contact, 60s**
	PR Bench	**wait 45 min before bake. Bake 50C 60s, 115C 60s**
	Develop Bench	Develop in AZ300-MIF, **70s**
		4x DI rinse, N2 dry
	Microscope	Inspect, develop more if necessary
	PEII	O2 plasma descum, 300 mT, 100 W, 30sec
Mesa2 Etch	RIE5	Load bare carrier wafer
		Standard O2 preclean (Kearns_01 (~20min pump down, 10min O2 clean, BCl3 Coat))
		Load samples onto carrier wafer, no oil
		Dan_05 BCL3 (10sccm, 10mT, 100W, 2min), Cl2 (10sccm, 5mT, 200W) **,** etch below sacrificial wells
		Soak sample in DI for 2min, N2 dry
	Solvent Bench	Preheat 1165 Stripper for 10min, 80C
		Sonicate on low at 80C for 10min. Rinse 4x DI, N2 dry
	3D Microscope	Inspect, strip more if necessary, do acidic piranha if necessary to remove etch residue
Intracavity contact metal and PEC cathode Litho	Solvent Bench	Spray with pipette (no sonicate) Ace, Iso, DI, 4x DI Dump&Rinse, N2 dry
	PR Bench	Dehydration bake, 2min 110oC, let cool 1min
		Spin HMDS Program 5 (3000rpm, 30s)
		Spin **nLOF2020** Program 5 (3000rpm 30s)
		Scrape off edge-bead from short edges
		Softbake, 110C 90s
	Contact Aligner	Expose **"Intracavity Metal, PEC Cathode**", 7.5mW/cm2, **10s**, No Filter, Black chuck, **Hard contact**
	PR Bench	**Post exposure bake 110C 60s**
	Develop Bench	Develop in AZ300MIF **50s**
		4x DI rinse, N2 dry
	Microscope	Inspect, develop more if necessary
	PEII	O2 plasma descum, 300 mT, 100 W, 30sec
Intracavity Contact metal and	Ebeam 4 or 3, or Sputter	Deposit Ti/Au (200A/10,000A), co- load flip chip submount
		Preheat 1165 Stripper for 10min, 80C

PEC cathode Dep	Solvent Bench	Soak 80C for 15 min. Spray with pipette, Rinse DI, N2 dry
	3D microscope	Inspect, liftoff more if necessary
Flip-chip Substrate Only: Metal Dep	Solvent Bench	Sonicate on low: 3min Ace, 3min Iso, 3 min DI, 4x DI Dump&Rinse, N2 dry
	Thermal Evaporator II	Load In and Au pellets into three boats (Boat 1: Au, Boats 2,3: In)
		Use springs to hold submounts
		Deposit 1700 nm of In followed by 200 nm of Au
Flip-Chip Thermo-compression Bond	Scribing bench	Cleave off the areas of chip where edge bead removal occurred
	PEII	O2 plasma descum, 300 mT, 100 W, 30sec
	Flip Chip Bond	Flip chip bond wafer to submount with In-Au Thermocompression bonding. Contact at 280C for 30s inFinetech, or at 200C for 2 hr in graphite holder in furnace in the packaging lab
PEC Lift-off	Packaging Lab	PEC etch to remove substrate 405 nm LED Array, or 420 nm array depending on SacQWs 1M KOH, -5C, or ~0.1M at 10(?)C - still to be optimized at low conc ~15 hrs
	Develop Bench	3x (Swab gently in DI+Tergitol, 3x rinse in DI)
	SEM	Inspect, swab more if necessary
	AFM	Measure RMS roughness in the aperture
n-contact litho	Solvent Bench	Spray with pipette (no sonicate) Ace, Iso, DI, 4x DI Dump&Rinse, N2 dry
	PR Bench	Dehydration bake, 2min 110oC, let cool 1min
		Spin HMDS Program 5 (3000rpm, 30s)
		Spin **nLOF2035** Program 5 (3000rpm 30s)
		Scrape off edge-bead from short edges
		Softbake, 110C 90s
	Contact Aligner	Expose "**n-contact**", 7.5mW/cm2, **10s**, No Filter, Black chuck, **Hard contact**
	PR Bench	**Post exposure bake 110C 60s**
	Develop Bench	Develop in AZ300MIF **50s**
		4x DI rinse, N2 dry
	Microscope	Inspect, develop more if necessary
	PEII	O2 plasma descum, 300 mT, 100 W, 30sec
n-contact etch	RIE5	Load bare carrier wafer
		Standard O2, BCl3/SiCl4 preclean (Yonkee_01 (~10min pump down, 10min O2 clean))
		Load samples onto carrier wafer, no oil
		~5nm SiCl4 etch
n-contact Dep	**E-beam 3**	Load samples using clips
		Deposit Ti (20nm), Au (350nm))
		Preheat 1165 Stripper for 10min, 80C

Cavity Resonance Check	Solvent Bench	Soak 80C for 15 min. Spray with pipette, Rinse DI, N2 dry
	3D microscope	Inspect, liftoff more if necessary
	Laser Testing Station	Measure spectra at ~5kA/cm2
		Check cavity resonance
	Vertical	If resonance is off, model in vertical/TFCalc/Matlab code adding a Ta2O5 n-side spacer to re-align the resonance with the peak gain. **Make sure you do the vertical simulation without the n-DBR as well, since this layer will increase the cavity length**
n-DBR Litho	Solvent Bench	Spray with pipette (no sonicate) Ace, Iso, DI, 4x DI Dump&Rinse, N2 dry
	PR Bench	Dehydration bake, 2min 110C, let cool 1min
		Spin **LOL 2000**, 2 krpm, 10 krpm/s, 30s (~250 nm thick)
		Edge Bead removal, Clean backside with EBR 100
		Softbake, 170 °C, 5min, let cool 2 min
		Spin **nLOF2035** Program 5 (3000rpm 30s)
		Edge Bead removal, Clean backside with EBR 100
		Softbake, 110C 90s
	Contact Aligner	Expose "N-DBR", 7.5mW/cm2, **10s**, No Filter, Black chuck, hard contact.
	PR Bench	**Post exposure bake 110oC 60s**
	Develop Bench	Develop in AZ300MIF **50s**
		4x DI rinse, N2 dry
	Microscope	Inspect, develop more if necessary
	PEII	O2 plasma descum, 300 mT, 100 W, 30sec
DBR Dep	IBD	Calibration Sample(s) using DSP sapphire ans Si, Ellipsometer/Filmetrics, JL_FP_1i5pTa2O5… ,JL_12_FP_1i5pSiO2…
		Deposit 12 periods SiO2/Ta2O5 n-DBR on VCSEL and DSP sapphire 1/4 wafer
DBR Liftoff	Solvent Bench	Preheat 1165 Stripper for 10min, 80oC
		Soak 80C for 15 min. Spray with pipette, Rinse DI, N2 dry
	3D Microscope	Inspect, liftoff more if necessary
LIV Test		Congrats, you made a VCSEL or at least a complicated micro LED!

A.3 BTJ Process Follower

181029 VCSEL Process Flow - BTJ Aperture		
Authors: SeungGeun and Jared Kearns		
Mask file name: 180426_IIA_VCSEL		
General Prep	PR Bench	Prep PRs and check experation date
		SPR220-3.0
		SPR220-7.0
		nLOF2020
		nLOF2035
Calibration (Day 1)	MOCVD	Grow xrd and emission wavelength callibrations for all relevant layers in the device
Calibration (Day 2)	XRD	Analyze XRD callibaration samples using ~30 min 2-theta/omega scans (6-8hrs XRD time)
		Fit the XRD data by simulating the structure and adjusting the parameters by hand, until a good fit is obtained
	Quicktest	Deposit In dots and In solder back contact
	Computer	Adjust the growth times and QW temperatures on the layers of interest in all the recipes. λEL>λFP is not desirable (i.e. λEL<λFP or λEL=λFP is prefered). λsacrificial>405nm is required for PEC etching. λsacrificial>420nm is required for observation under Fluorescence microscope
Growth (Day 3)	MOCVD	Grow the desired VCSEL Series
Begin Processing (Day 4)	Furnace	600C, Air, 15min
	Quicktest	Deposit In dots and In solder back contact. Measure Quicktest data for the VCSELs. Save all spectrum and IV data. Regrow if power or voltage is bad
Remove Indium	Acid Bench	3:1 HCl:HNO3 Aqua Regia, 3x 10min, mix new batch each iteration, wait 5min for boiling, 120C on hotplate. End with DI clean, N2 dry, inspect and repeat if necessary
TJ regrowth	Acid Bench	BHF 5 min (To remove Mg film) & DI rinse
	MOCVD	Grow 10nm n++GaN
Alignment Litho	Solvent Bench	Sonicate on high: 3min Ace, 3min Iso, 3min DI, 4x DI Rinse&drain, N2 dry
	PR Bench	Dehydration bake, 2min 110oC, let cool 30sec
		Spin HMDS Program 5 (3000rpm, 30s)
		Spin **nLOF2035** Program 5 (3000rpm 30s)
		edge-bead removal from short edges
		Soft bake, 110oC 90s

	Contact Aligner	Expose **"1.Alignment"**, **10s**,7.5mW/cm2, No Filter, Black chuck, **Hard contact** 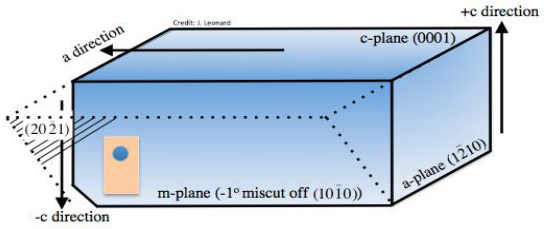
	Develop Bench	Post exposure bake 110oC 60s
		Develop in AZ300-MIF **50s**
		4x DI rinse&drain, N2 dry
	Microscope	Inspect, develop more if necessary
Alignment Etch	RIE5	Load bare carrier wafer
		Standard O2, BCl3/Cl2 preclean (Dan_01 (~10min pump down, 10min O2 clean))
		Load samples onto carrier wafer, no oil
		Dan_05 (120 nm/min) BCL3 (10sccm, 10mT, 100W, 2min), Cl2 (10sccm, 5mT, 200W, 5 min), etch~ 5 min
	Solvent Bench	Preheat AZ NMP Stripper for 10 min, 80 C
		Sonicate on low AZ NMP at 80C for 10min. Rinse 4x DI Rinse&Dump, N2 dry
Aperture Litho	Solvent Bench	Sonicate on high: 3min Ace, 3min Iso, 3min DI, 4x DI Rinse&drain, N2 dry
	PR Bench	Dehydration bake, 2min 110oC, let cool 30sec
		Spin HMDS Program 5 (3000rpm, 30s)
		Spin **SPR220-3.0** Program 5 (3000rpm 30s)
		edge-bead removal from short edges
		Soft bake, 115oC 90s
	Contact Aligner	Expose **"2.IONIMPLANT APERTURE"**, 7.5mW/cm2, **25s,** No Filter, Black chuck, **Hard contact**
	Develop Bench	**Post expsure bake 115°C 60s**
		Develop in AZ300MIF **50s**
		4x DI rinse&drain, N2 dry
	Microscope	Inspect, develop more if necessary
	PEII	O2 plasma descum, 300 mT, 100 W, 30sec ~ It may be better to skip this step, TBD
Aperture Etch	RIE5	Load bare carrier wafer
		Standard O2, BCl3/Cl2 preclean (Dan_01 (~10min pump down, 10min O2 clean))
		Load samples onto carrier wafer, no oil
		SLEE_02 (110 nm/min) (etch past p++ & n++GaN, about 30-40 nm), Cl2 (10sccm, 5mT, 200W) **(Can also use the low power etch)**
	Solvent Bench	Preheat AZ NMP Stripper for 10 min, 80 C
		Sonicate on low AZ NMP at 80C for 10min. Rinse 4x DI Rinse&Dump, N2 dry

	Acid Bench	acidic piranha
	AFM	Measure aperture height and roughness
Ion Implant hardmask Litho	Solvent Bench	Sonicate on high: 3min Ace, 3min Iso, 3min DI, 4x DI Rinse&drain, N2 dry
	PR Bench	Dehydration bake, 2min 110oC, let cool 30sec
		Spin HMDS Program 5 (3000rpm, 30s)
		Spin **nLOF2020** Program 5 (3000rpm 30s)
		edge-bead removal from short edges
		Soft bake, 110oC 90s
		Expose **"8.IONIMPLANT (BTJ)"**, **10s**,7.5mW/cm2, No Filter, Black chuck, **Hard contact**
		Post exposure bake 110oC 60s
		Develop in AZ300-MIF **50s**
		4x DI rinse&drain, N2 dry
	Microscope	Inspect, develop more if necessary
	PEII	O2 plasma descum, 300 mT, 100 W, 30sec
Ion Implant hardmask Litho	**Ebeam 3**	Deposit Ti/Au 200A (1A/s)/ 5000A (1A/s→100A,3A/sec→500A, 6A/sec→2000A)
	Solvent Bench	Preheat AZ NMP Stripper for 10 min, 80 C
		Sonicate on low AZ NMP at 80C for 10min. Rinse 4x DI Rinse&Dump, N2 dry
Ion Implant	Microscope	Inspect, liftoff more if necessary
	Leonard Kroko, Inc	Ship samples to Leonard Kroko
		wafer size: ~1cm2
		Ion: Al, Dose: 10^15 ions/cm2, Energy: 20 keV, Normal incidence
		~3-4 day turn-around
	Acid Bench	3:1 HCl:HN03 Aqua Regia, 3x 10min, mix new batch each iteration, wait 5min for boiling, 120°C on hotplate. End with DI+Tergitol clean, N2 dry
n-GaN Current Spreading Growth	3D Microscope	Inspect, strip more if necessary, do piranha if necessary
	UV Ozone	20 min (Oxidize Si on surface) (Right before regrowth)
	Acid Bench	BHF 5 min (Remove SiO2) & DI rinse
	MOCVD	Grow n-GaN (Model the structure to get correct thickness for the quicktest wavelength. Minimize the required gain, while maximizing enhancement factor)
Mesa Litho	AFM (optional)	Measure intracavity contact RMS roughness and aperture height
	Solvent Bench	Sonicate on high: 3min Ace, 3min Iso, 3min DI, 4x DI Rinse&drain, N2 dry
	PR Bench	Dehydration bake, 2min 110oC, let cool 30sec
		Spin HMDS Program 5 (3000rpm, 30s)

		Spin **SPR220-3.0 Program 3 (2000rpm 45s (?))** (use SPR 220-7.0 for thick cavity)
		Soft bake, 115oC 90s
	Contact Aligner	Expose **"3.MESA"**, 7.5mW/cm2, **25s,** No Filter, Black chuck, **Hard contact**
	Develop Bench	**Post expsure bake 115°C 60s**
		Develop in AZ300MIF **60s**
		4x DI rinse&drain, N2 dry
	Microscope	Inspect, develop more if necessary
	PEII	O2 plasma descum, 300 mT, 100 W, 30sec
Mesa Etch	Dektak	Measure PR thickness
	RIE5	Load bare carrier wafer
		Standard O2, BCl3/Cl2 preclean (Kearns_01 (~10min pump down, 10min O2 clean))
		Load samples onto carrier wafer, no oil
		Dan_05 (120 nm/min) (etch past sacrificial QW, PR should be thicker than etching depth) BCL3 (10sccm, 10mT, 100W, 2min), Cl2 (10sccm, 5mT, 200W)
	Solvent Bench	Preheat 1165 Stripper for 10 min, 80 C
p-DBR Litho		Sonicate on low AZ NMP at 80C for 10min. Rinse 4x DI Rinse&Dump, N2 dry
	Solvent Bench	Sonicate on high: 3min Ace, 3min Iso, 3min DI, 4x DI Rinse&drain, N2 dry
	PR Bench	Dehydration bake, 2min 110oC, let cool 1min
		Spin HMDS Program 5 (3000rpm, 30s)
		Spin **nLOF2035** Program 5 (3000rpm 30s)
		edge-bead removal from short edges
		Softbake, 110oC 90s
	Contact Aligner	Expose **"4.p-DBR"**, 7.5mW/cm2, **10s**, No Filter**,** Black chuck, **Hard contact**
	PR Bench	**Post exposure bake 110C 60s**
	Develop Bench	Develop in AZ300MIF **50s**
		4x DI rinse&drain, N2 dry
	PEII	O2 plasma descum, 300 mT, 100 W, 30sec
p-DBR Dep	Microscope	Inspect, develop more if necessary
	IBD	Calibration Sample(s) using DSP sapphire and Si, Ellipsometer/Filmetrics, JL_FP_1i5pTa2O5… ,JL_12_FP_1i5pSiO2…
		Deposit 16 periods SiO2/Ta2O5, Co-load a DSP sapphire 1/4 wafer
	Filmmetrics	Measure and Model reflectance on sapphire sample
	Solvent Bench	Preheat AZ NMP Stripper for 10min, 80oC
		Sonicate on low AZ NMP at 80C for 10min. Rinse 4x DI Rinse&Dump, N2 dry
Intracavity contact	3D Microscope	Inspect, liftoff more if necessary

metal and PEC cathode Litho	Solvent Bench	Spray with pipette **(don't sonicate**) 3min Ace, 3min Iso, 3min DI, 4x DI Dump&Rinse, N2 dry
	PR Bench	Dehydration bake, 2min 110oC, let cool 1min
		Spin HMDS Program 5 (3000rpm, 30s)
		Spin **nLOF2035** Program 5 (3000rpm 30s)
		Scrape off edge-bead from short edges
		Softbake, 110C 90s
	Contact Aligner	Expose **"5.INTRACAVITY METAL**", 7.5mW/cm2, **10s**, No Filter, Black chuck, **Hard contact**
	PR Bench	**Post exposure bake 110C 60s**
	Develop Bench	Develop in AZ300MIF **50s**
		4x DI rinse&drain, N2 dry
	Microscope	Inspect, develop more if necessary
Intracavity Contact metal and PEC cathode Dep	PEII	O2 plasma descum, 300 mT, 100 W, 30sec
	Solvent Bench	Preheat AZ NMP Stripper for 10min, 80C
	Ebeam 3 or Ebeam 4 or Sputter 4	**Ebeam 3:** Deposit Ti/Au (300A/10,000A) **Angled chuck** **Ebeam 4:** Deposit Ti/Au (300A/10,000A) **planetary angle&rotate.** **Sputter 4/5:** Load samples using clips (Optional, load flip-chip substrates as well) Adjust Ti and Au gun angle to "20" Run J_Leonard Ti-Au Dep (Ar palsma clean, Ti (10nm), Au (500nm)) Co-load flip-chip submount
	Solvent Bench	Preheat AZ NMP Stripper for 10min, 80C
		Sonicate on low AZ NMP at 80C for 10min. Rinse 4x DI Rinse&Dump, N2 dry
Flip-chip Substrate Only: Metal Dep	3D microscope	Inspect, liftoff more if necessary
	Thermal Evaporator II	Load In and Au pellets into three boats (Boat 1: Au, Boats 2,3: In)
		Use springs to hold submounts
		Deposit 1700 nm of in followed by 200 nm of Au
Flip-Chip Bond	Scribing bench	Cleave off the areas of chip where edge bead removal occurred (scribe the backside then nick the edge of the chip)
		Label back of flip-chip substrates
	Solvent Bench	Sonicate (only submount) Spray (actual samples) on low 3min Ace, 3min Iso, 3 min DI, 3xDI Dump&Rinse, N2 dry
	Finetech Flip Chip Bonder	Flip chip bond wafer to submount with In-Au Thermocompression bonding. Contact at 280C for 30s
	Or Furnace	Clamp sample to submount in graphite carrier, finger tight
		Anneal 200^{o}C 2hr
PEC Lift-off	Packaging Lab	PEC etch to remove substrate, temp control bath will take ~2hr to cool down 405 nm LED Array, or 420 nm LED array 1M KOH, -5C in temperature control bath 4 ~ 24 hour

	Microscope	Inspect, etch more if necessary
	Develop Bench	Swab in tergitol, light strokes, follow by DI rinse
	SEM	Inspect, repeat swab if necessary
	AFM	Measure roughness of mesa
n-contact litho	Solvent Bench	Spray with pipette **(don't sonicate**) 3min Ace, 3min Iso, 3min DI, 4x DI Dump&Rinse, N2 dry
	PR Bench	Dehydration bake, 2min 110oC, let cool 1min
		Spin **LOL 2000**, 2000 rpm, 10 krpm/s, 30s (~250 nm thick)
		Softbake, 170 °C, 5min, let cool 2 min
		Spin **nLOF2035** Program 5 (3000rpm 30s)
		edge-bead removal from short edges
		Softbake, 110oC 90s
	Contact Aligner	Expose "**6.N-CONTACT**", 7.5mW/cm2, **10s**, No Filter, Black chuck, **Hard contact**
	PR Bench	**Post exposure bake 110C 60s**
	Develop Bench	Develop in AZ300MIF **50s**
		4x DI Drain&rinse, N2 dry
	Microscope	Inspect, develop more if necessary
	PEII	O2 plasma descum, 300 mT, 100 W, 30sec
n-contact Dep	**E-beam 3**	Load samples using clips
		Deposit Ti (20nm), Au (500nm))
	Solvent Bench	Preheat AZ NMP Stripper for 10min, 80C
		Treat in AZ NMP at 80C for 3min. **Don't sonicate** Scratch where there aren't devices. Spray with pipette from the scratch. Treat in AZ NMP at 80C for 5min. Repeat Spray and AZ NMP step. Rinse 4x DI, N2 dry
	3D microscope	Inspect, liftoff more if necessary
Cavity Resonance Check	Laser Testing Station	Record spectra vs current at each corner and middle of sample
		Check cavity resonance
	Vertical	If resonance is off, model in vertical adding a Ta2O5 n-side spacer to re-align the resonance with the peak gain. **Make sure you do the vertical simulation without the n-DBR as well, since this layer will increase the cavity length**
n-DBR Litho	Solvent Bench	Spray with pipette **(don't sonicate**) 3min Ace, 3min Iso, 3min DI, 4x DI Dump&Rinse, N2 dry
	PR Bench	Dehydration bake, 2min 110C, let cool 1min
		Spin **LOL 2000**, 2 krpm, 10 krpm/s, 30s (~250 nm thick)
		Edge Bead removal, Clean backside with EBR 100
		Softbake, 170 °C, 5min, let cool 2 min
		Spin **nLOF2035** Program 5 (3000rpm 30s)
		Edge Bead removal, Clean backside with EBR 100

		Softbake, 110C 90s
	Contact Aligner	Expose "**7.N-DBR**", 7.5mW/cm2, **10s**, No Filter, Black chuck, hard contact.
	PR Bench	**Post exposure bake 110oC 60s**
	Develop Bench	Develop in AZ300MIF **50s**
		4x DI rinse&Drain, N2 dry
	Microscope	Inspect, develop more if necessary
	PEII	O2 plasma descum, 300 mT, 100 W, 30sec
DBR Dep	IBD	Calibration Sample(s) using DSP sapphire and Si, Ellipsometer/Filmetrics, JL_FP_1i5pTa2O5… ,JL_12_FP_1i5pSiO2…
		Deposit 12 periods SiO2/Ta2O5 n-DBR on VCSEL and DSP sapphire 1/4 wafer
DBR Liftoff	Solvent Bench	Preheat AZ NMP Stripper for 10min, 80oC
		Treat in AZ NMP at 80C for 5min. Spray with pipette. Repeat AZ NMP and spray step. Rinse 4x I Rinse&Drain, N2 dry
	3D Microscope	Inspect, liftoff more if necessary
LIV Test		Congrats, you made a VCSEL or a fancy microLED!

A.4 Sapphire VCSEL Design

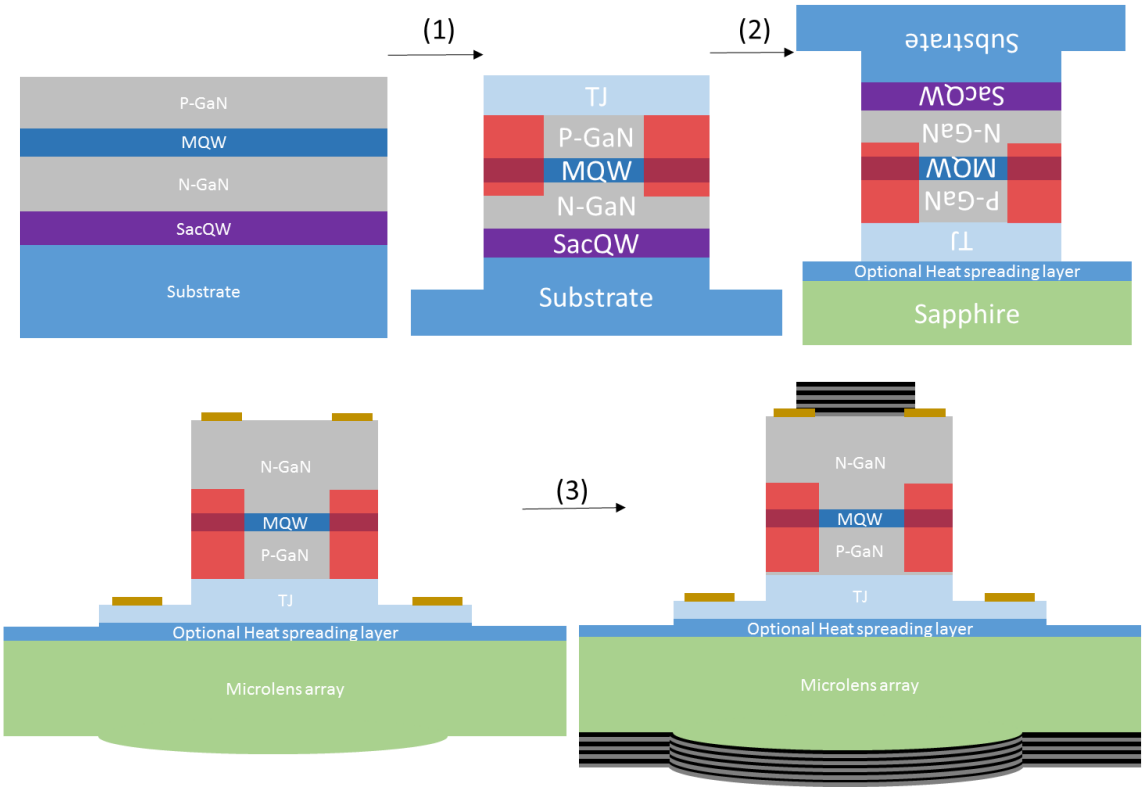

Figure A4-1_. Depicts the process flow of making a VCSEL with a sapphire cavity. After the epi growth, the sample is ion implanted, undergoes a TJ regrowth, and has mesas etched (1). Then the devices are wafer bonded to a thin sapphire wafer (~100 µm or less) (2). The GaN substrate is then removed via PEC etching, lens structures are etched in the sapphire, a second mesa etch is performed, and contacts are deposited. Finally, DBRs are deposited on both sides of the cavity to finish the device (3).

191004 VCSEL Process Flow - IIA, Sapphire Cavity		
Authors: Jared		
Mask file name: lens_VCSEL		
	PR Bench	Prep PRs and check experation date
		SPR220-3.0
		nLOF2020
		nLOF2035
Calibration (Day 1)	MOCVD	Grow xrd and emission wavelength callibrations for all relevant layers in the device
Calibration (Day 2)	XRD	Analyze XRD callibaration samples using ~35 min 2-theta/omega scans (6-8hrs XRD time)

		Fit the XRD data by simulating the structure and adjusting the parameters by hand, until a good fit is obtained
	Quicktest	Deposit In dots and In solder back contact
	Computer	Adjust the growth times and QW temperatures on the layers of interest in all the recipes. λEL>λFP is not desirable (i.e. λEL<λFP or λEL=λFP is prefered). λsacrificial>405nm is required for PEC etching. λsacrificial>420nm is required for observation under Fluorescence microscope
Growth (Day 3)	MOCVD	Grow the desired VCSEL Series
Begin Processing (Day 4)	Furnace	600C, Air, 15min
	Quicktest	Deposit In dots and In solder back contact. Measure Quicktest data for the VCSELs. Save all spectrum and IV data. Regrow if power or voltage is bad
Remove Indium	Acid Bench	3:1 HCl:HNO3 Aqua Regia, 3x 10min, mix new batch each iteration, wait 5min for boiling, 120C on hotplate. End with DI+Tergitol clean, N2 dry
Mesa Litho	AFM (optional)	Measure intracavity contact RMS roughness
	Solvent Bench	Sonicate on high: 2min Ace, 2min Iso, 3x 30s DI Rinse, N2 dry
	PR Bench	Dehydration bake, 2min 110oC, let cool 30sec
		Spin HMDS Program 5 (3000rpm, 30s)
		Spin **SPR220-3.0 Program 3 (2000rpm 45s (?))** (use SPR 220-7.0 for thick cavity)
		Edge Bead removal, Clean backside with EBR 100
		Soft bake, 115oC 90s (120s for SPR 220 7.0)
	Contact Aligner	Expose **"MESA"**, 7.5mW/cm2, **25s,** No Filter, Black chuck, **Hard contact**
		Wait 10 min (or 45 min if using SPR 220 - 7.0)
	Develop Bench	**Post expsure bake 115°C 60s** (50C 60s, 115C 60s fro SPR 220 - 7.0)
		Develop in AZ300MIF **60s** (70 s for SPR 220 - 7.0)
		30 sec DI rinse flowing, N2 dry
	Microscope	Inspect, develop more if necessary
	PEII	O2 plasma descum, 300 mT, 100 W, 30sec
Mesa Etch	RIE5	Load bare carrier wafer
		Standard O2, BCl3/Cl2 preclean (Kearns_01 (~10min pump down, 10min O2 clean))
		Load samples onto carrier wafer, no oil
		Dan_05 (120 nm/min) (etch past sacrificial QW, ~ 3um, PR should be thicker than etching depth) BCL3 (10sccm, 10mT, 100W, 2min), Cl2 (10sccm, 5mT, 200W)
	Solvent Bench	Preheat 1165 Stripper for 10 min, 80 C

	Solvent Bench	Sonicate on low: 3min Ace, 3min Iso, 3x 30s DI Rinse, N2 dry
Ion Implant hardmask Litho	PR Bench	Dehydration bake, 2min 110oC, let cool 30sec
		Spin HMDS Program 5 (3000rpm, 30s)
		Spin **nLOF2035** Program 5 (3000rpm 30s)
		Soft bake, 110oC 90s
		Expose **"Ion Implant"**, **10s**,7.5mW/cm2, No Filter, Black chuck, **Hard contact**
		Post exposure bake 110oC 60s
		Develop in AZ300-MIF **50s**
		2min DI rinse flowing, N2 dry
	Microscope	Inspect, develop more if necessary
	Ebeam 3	Deposit Ti/Au 200A (1A/s)/3000A (1A/s→100A,3A/sec→500A, 6A/sec→3000A)
Ion Implant hardmask Litho	Solvent Bench	Preheat AZ NMP Stripper for 10 min, 80 C
		Sonicate on Low AZ NMP at 80C for 10min. Rinse 3x 30s DI+Tergitol Dump, N2 dry
	Microscope	Inspect, liftoff more if necessary
Ion Implant	Leonard Kroko, Inc	Ship samples to Leonard Kroko
		wafer size: ~1cm2
		Ion: Al, Dose: 10^14 ions/cm2, Energy: 20 keV, Normal incidence
		~3-4 day turn-around
	Acid Bench	3:1 HCl:HN03 Aqua Regia, 3x 10min, mix new batch each iteration, wait 5min for boiling, 120°C on hotplate. End with DI+Tergitol clean, N2 dry
TJ regrowth Growth	3D Microscope	Inspect, strip more if necessary
	UV Ozone	20 min (Oxidize Si on surface) (Right before regrowth) 2x
	Acid Bench	BHF 5 min (Remove SiO2) & DI rinse 2x
	MOCVD	Grow TJ
Flip Chip Bonding	Solvent Bench	Tergitol Swab, Sonicate on high 3min Ace, 3min Iso, 3 min DI, Rinse, N2 dry
	EVG	N2 plasma activation. Program: Exsitu_0.8
	Tystar Tube 3	Clamp sample to submount in graphite carrier, finger tight
		Anneal 615^{o}C 4 hr with dryvar recipe
PEC Metal Dep	Solvent Bench	Sonicate on low 3min Ace, 3min Iso, 3min DI, Rinse, N2 dry
	Ebeam 3	Deposit Ti/Au 10A (0.5A/s)/50A (0.5A/s)

PEC Lift-off	Packaging Lab	PEC etch to remove substrate, temp control bath will take ~2hr to cool down 405 nm LED Array, 1M KOH, -5C in temperature control bath
	Microscope	Inspect, etch more if necessary
	Develop Bench	Swab in tergitol, light strokes, follow by DI rinse
	SEM	Inspect, repeat swab if necessary
	AFM	Measure roughness of mesa
Lens Litho	Solvent Bench	Sonicate on low: 3min Ace, 3min Iso, 3min DI, Rinse, N2 dry
	PR Bench	Dehydration bake, 2min 110oC, let cool 30sec
		Spin HMDS Program 5 (3000rpm, 30s)
		Spin **SPR220-3.0 Program 5 (~2.7 um)**
		Edge Bead removal, Clean backside with EBR 100
		Soft bake, 115oC 90s (120s for SPR 220 7.0)
	Contact Aligner	Expose **"Lens"**, 7.5mW/cm2, **25s,** No Filter, Black chuck, **Hard contact**
		Wait 10 min
	Develop Bench	**Post expsure bake 115°C 60s**
		Develop in AZ300MIF **60s**
		30 sec DI rinse flowing, N2 dry
	Microscope	Inspect, develop more if necessary
	Solvent Bench	Thermal reflow lens at 150C for 90 sec
Lens Etch	ICP1	place reflow sample on carrier wafer
		recipe111 (BCl3 RF 900W, bias 400W, 0.3 Pa, 40 min)
		run CF4 cleaning recipe for 20 min
	Solvent Bench	put sample in heat NMP for 20 min, 80 C w/ sonication high
Mesa 2 Litho	AFM (optional)	Measure intracavity contact RMS roughness
	Solvent Bench	Sonicate on high: 2min Ace, 2min Iso, 3x 30s DI Rinse, N2 dry
	PR Bench	Dehydration bake, 2min 110oC, let cool 30sec
		Spin HMDS Program 5 (3000rpm, 30s)
		Spin **SPR220-3.0 Program 3**
		Edge Bead removal, Clean backside with EBR 100
		Soft bake, 115oC 90s (120s for SPR 220 7.0)
	Contact Aligner	Expose **"INNER MESA"**, 7.5mW/cm2, **25s,** No Filter, Black chuck, **Hard contact**
		Wait 10 min (or 45 min if using SPR 220 - 7.0)
	Develop Bench	**Post expsure bake 115°C 60s** (50C 60s, 115C 60s fro SPR 220 - 7.0)

		Develop in AZ300MIF **60s** (70 s for SPR 220 - 7.0)
		30 sec DI rinse flowing, N2 dry
	Microscope	Inspect, develop more if necessary
	PEII	O2 plasma descum, 300 mT, 100 W, 30sec
Mesa 2 Etch	RIE5	Load bare carrier wafer
		Standard O2, BCl3/Cl2 preclean (Kearns_01 (~10min pump down, 10min O2 clean))
		Load samples onto carrier wafer, no oil
		Dan_05 (120 nm/min) (to n-current spreading layer, not through) BCL3 (10sccm, 10mT, 100W, 2min), Cl2 (10sccm, 5mT, 200W)
	Solvent Bench	Preheat 1165 Stripper for 10 min, 80 C, remove PR
n-contact litho	Solvent Bench	Spray with pipette (no sonicate) 2min Ace, 2min Iso, 3x 30s DI+Tergitol Dump&Rinse, N2 dry
	PR Bench	Spin **LOL 2000**, 2000 rpm, 10 krpm/s, 30s (~250 nm thick)
		Softbake, 170 °C, 5min, let cool 2 min
		Spin **nLOF2035** Program 5 (3000rpm 30s)
		edge-bead removal from short edges
		Softbake, 110oC 90s
	Contact Aligner	Expose "**CONTACT**", 7.5mW/cm2, **10s**, No Filter, Black chuck, **Hard contact**
	PR Bench	**Post exposure bake 110C 60s**
	Develop Bench	Develop in AZ300MIF **50s**
		2min DI rinse flowing, N2 dry
	Microscope	Inspect, develop more if necessary
	PEII	O2 plasma descum, 300 mT, 100 W, 30sec
n-contact etch	RIE5	Load bare carrier wafer
		Standard O2, BCl3/SiCl4 preclean (Yonkee_01 (~10min pump down, 10min O2 clean))
		Load samples onto carrier wafer, no oil
		SLEE_05 10sec (~5nm) SiCl4 (270W)
n-contact Dep	**E-beam 3**	Load samples using clips
		Deposit Ti (20nm), Au (500nm))
	Solvent Bench	Preheat AZ NMP Stripper for 10min, 80C
		Preheat AZ NMP Stripper for 10min, 80C
		Treat in AZ NMP at 80C for 3min. **Don't sonicate** Scratch where there aren't devices. Spray with pipette from the scratch. Treat in AZ NMP at 80C for 5min. Repeat Spray and AZ NMP step. Rinse 3x 30s DI, N2 dry

	3D microscope	Inspect, liftoff more if necessary
n-DBR Litho	Solvent Bench	2min Ace, 2min Iso, 3x 30s DI Rinse, N2 dry
	PR Bench	Dehydration bake, 2min 110C, let cool 1min
		Spin **LOL 2000**, 2 krpm, 10 krpm/s, 30s (~250 nm thick)
		Edge Bead removal, Clean backside with EBR 100
		Softbake, 170 °C, 5min, let cool 2 min
		Spin **nLOF2035** Program 5 (3000rpm 30s)
		Edge Bead removal, Clean backside with EBR 100
		Softbake, 110C 90s
	Contact Aligner	Expose "**N-DBR**", 7.5mW/cm2, **10s**, No Filter, Black chuck, hard contact.
	PR Bench	**Post exposure bake 110oC 60s**
	Develop Bench	Develop in AZ300MIF **50s**
		2min DI rinse flowing, N2 dry
	Microscope	Inspect, develop more if necessary
	UV Ozone	20min (~6A/min)
DBR Dep	IBD	Calibration Sample(s) using DSP sapphire, Ellipsometer/Filmetrics, JL_FP_1i5pTa2O5… ,JL_12_FP_1i5pSiO2…
		Deposit 12 periods SiO2/Ta2O5 n-DBR on VCSEL and DSP sapphire 1/4 wafer on one side, and deposit16 p SiO2/Ta2O5 on the other side
DBR Liftoff	Solvent Bench	Preheat AZ NMP Stripper for 10min, 80oC
		Treat in AZ NMP at 80C for 5min. Spray with pipette. Repeat AZ NMP and spray step. Rinse 3x 30s DI Rinse, N2 dry
	3D Microscope	Inspect, liftoff more if necessary
	Solvent Bench	no ultrasonic: 3min Ace, 3min Iso, 3x 30s DI Rinse, N2 dry
LIV Test		Congrats, you made a VCSEL!

References

[1] Iga, K., “Surface-emitting laser-its birth and generation of new optoelectronics field,” IEEE J. Sel. Top. Quantum Electron. **6**(6), 1201–1215 (2000).

[2] Michalzik, R. and Ebeling, K. J., “Operating Principles of VCSELs.”

[3] “VCSEL Market by Type (Single-Mode, Multimode), Material (GaAs, InP, Others), Wavelength, Application (Sensing, Data Communication), Industry (Consumer Electronics, Automotive, Data Center, Commercial & Industrial), and Geography - Global Forecast to 2025.”, <https://www.researchandmarkets.com/reports/5023122/vcsel-market-by-type-single-mode-multimode?utm_code=2hm9w9&utm_medium=GN> (27 May 2020).

[4] “VCSEL (Vertical-Cavity Surface-Emitting Laser) Market Report 2018 - Global Forecast to 2023.”, <https://www.globenewswire.com/news-release/2018/08/08/1548697/0/en/VCSEL-Vertical-Cavity-Surface-Emitting-Laser-Market-Report-2018-Global-Forecast-to-2023.html> (14 May 2020).

[5] Tatum, J. A., Landry, G. D., Gazula, D., Wade, J. K. and Westbergh, P., “VCSEL-based optical transceivers for future data center applications,” 2018 Opt. Fiber Commun. Conf. Expo. OFC 2018 - Proc., 1–3 (2018).

[6] Kanakis, Iliadis, Soenen, Moeneclaey, Argyris, Kalavrouziotis, Spiga, Bakopoulos and Avramopoulos., “High-Speed VCSEL-Based Transceiver for 200 GbE Short-Reach Intra-Datacenter Optical Interconnects,” Appl. Sci. **9**(12), 2488 (2019).

[7] Jang, K. W., Yoo, W. J., Shin, S. H., Han, K. T., Lee, B., Pyeon, C. H., Misawa, T., Ji, Y. H., Cho, S. and Park, B. G., “Development of a fiber-optic Cerenkov radiation sensor to verify spent fuel: Characterization of the Cerenkov radiation generated from an optical fiber,” J. Korean Phys. Soc. **61**(10), 1704–1708 (2012).

[8] “Optical Fiber Attenuation – Fosco Connect.”, <https://www.fiberoptics4sale.com/blogs/archive-posts/95052294-optical-fiber-attenuation> (14 July 2020).

[9] Liao, C. L., Ho, C. L., Chang, Y. F., Wu, C. H. and Wu, M. C., “High-Speed light-emitting diodes emitting at 500 nm with 463-mhz modulation bandwidth,” IEEE Electron Device Lett. **35**(5), 563–565 (2014).

[10] “Why Apple chose digital lidar | Ouster.”, <https://ouster.com/blog/why-apple-chose-digital-lidar/> (27 May 2020).

[11] Mor, Z. and Morgenstein, B., “Overlapping pattern projector” (2016).

[12] Jaffe, J. S., “Underwater Optical Imaging: The Past, the Present, and the Prospects,” IEEE J. Ocean. Eng. **40**(3), 683–700 (2015).

[13] “Will take Android brands two years to catch up with Face ID, say key parts manufacturers - 9to5Mac.”, <https://9to5mac.com/2018/03/20/apple-face-id-two-year-lead/> (10 June 2020).

[14] “Image Sensors World: TechInsights Finds Sony ToF Sensor Inside iPad Pro LiDAR, iFixit Tests LiDAR Operation.”, <http://image-sensors-world.blogspot.com/2020/03/techinsights-finds-sony-tof-sensor.html> (10 June 2020).

[15] “How Apple’s iPhone X TrueDepth Camera Works - ExtremeTech.”,

<https://www.extremetech.com/mobile/255771-apple-iphone-x-truedepth-camera-works> (27 May 2020).

[16] “Apple’s Face ID [The iPhone X’s facial recognition tech] explained | Computerworld.”, <https://www.computerworld.com/article/3235140/apples-face-id-the-iphone-xs-facial-recognition-tech-explained.html> (27 May 2020).

[17] Extance, A., “Faces light up over VCSEL prospects,” SPIE Newsroom (2018).

[18] Serkland, D. K., Peake, G. M., Geib, K. M., Lutwak, R., Garvey, R. M., Varghese, M. and Mescher, M., “VCSELs for atomic clocks,” Vertical-Cavity Surface-Emitting Lasers X **6132**(February 2006), 613208 (2006).

[19] Schweber, B., “Chip-scale atomic clock approaches performance of modules | EE Times,” <https://www.eetimes.com/chip-scale-atomic-clock-approaches-performance-of-modules/#> (22 January 2020).

[20] Ahmed, M., Magalhães, D. V., Bebeachibuli, A., Müller, S. T., Alves, R. F., Ortega, T. A., Weiner, J. and Bagnato, V. S., “The Brazilian time and frequency atomic standards program,” An. Acad. Bras. Cienc. **80**(2), 217–252 (2008).

[21] Najda, S. P., Perlin, P., Leszczyński, M., Stanczyk, S., Clark, C. C., Slight, T. J., Macarthur, J., Prade, L. and McKnight, L. J., “GaN laser diodes for quantum sensors and optical atomic clocks,” Quantum Inf. Sci. Sensing, Comput. XII **11391**, M. Hayduk and E. Donkor, Eds., 10, SPIE (2020).

[22] Shen, C., Ooi, E.-N., Sun, X., Ooi, B. S. and Ng, T. K., “Study on laser-based white light sources,” Light. Devices, Mater. Appl. **10940**, M. Strassburg, J. K. Kim, and M. R. Krames, Eds., 52, SPIE (2019).

[23] Pourhashemi, A., Farrell, R. M., Hardy, M. T., Hsu, P. S., Kelchner, K. M., Speck, J. S., Denbaars, S. P. and Nakamura, S., “Pulsed high-power AlGaN-cladding-free blue laser diodes on semipolar (20$\bar{2}$1) GaN substrates,” Appl. Phys. Lett. **103**(15), 151112 (2013).

[24] “Laser Lighting: White-light lasers challenge LEDs in directional lighting applications | Laser Focus World.”, <https://www.laserfocusworld.com/lasers-sources/article/16548296/laser-lighting-whitelight-lasers-challenge-leds-in-directional-lighting-applications> (10 June 2020).

[25] Carey, J. A. and Rudy, P., “Intelligent Lighting Designs Enabled by Laser Light,” LED Prof. Rev., 66–70 (2017).

[26] Hanafi, A., “New High-brightness laser-based white light source for vehicular lighting systems (and Other Applications),” Opt. InfoBase Conf. Pap., AIW3B.1, OSA - The Optical Society (2016).

[27] Kuramoto, M., Kobayashi, S., Akagi, T., Tazawa, K., Tanaka, K., Nakata, K. and Saito, T., “Watt-class blue vertical-cavity surface-emitting laser arrays,” Appl. Phys. Express **12**(9), 091004 (2019).

[28] “OSRAM Blaue Laser Diode 1.6 W in TO56 Bauform.”, .

[29] Haas, H., Chen, C. and O’Brien, D., “A guide to wireless networking by light,” Prog. Quantum Electron. **55**, 88–111 (2017).

[30] Lee, C., Islim, M. S., Videv, S., Sparks, A., Shah, B., Rudy, P., McLaurin, M., Haas, H. and Raring, J., “Advanced LiFi technology: Laser light,” Light. Devices, Mater. Appl. XXIV

11302, M. Strassburg, J. K. Kim, and M. R. Krames, Eds., 38, SPIE (2020).

[31] Peach, M., "Wide-area Li-Fi network generating interest," <https://optics.org/news/6/11/30> (10 June 2020).

[32] "United States Frequency Allocation Chart | National Telecommunications and Information Administration.", <https://www.ntia.doc.gov/page/2011/united-states-frequency-allocation-chart> (10 June 2020).

[33] Shen, C., Guo, Y., Oubei, H. M., Ng, T. K., Liu, G., Park, K.-H., Ho, K.-T., Alouini, M.-S. and Ooi, B. S., "20-meter underwater wireless optical communication link with 15 Gbps data rate," Opt. Express **24**(22), 25502 (2016).

[34] Islim, M. S., Ferreira, R. X., He, X., Xie, E., Videv, S., Viola, S., Watson, S., Bamiedakis, N., Penty, R. V., White, I. H., Kelly, A. E., Gu, E., Haas, H. and Dawson, M. D., "Towards 10 Gb/s orthogonal frequency division multiplexing-based visible light communication using a GaN violet micro-LED," Photonics Res. **5**(2), A35 (2017).

[35] "LEDs Are Just a Holding Place: Get Ready for Laser LiFi.", <https://spie.org/news/leds-are-just-a-holding-place_get-ready-for-laser-lifi-?SSO=1> (28 May 2020).

[36] "Will Apple, Facebook or Microsoft be the future of augmented reality? | 1BusinessWorld.", <https://1businessworld.com/2020/02/business/will-apple-facebook-or-microsoft-be-the-future-of-augmented-reality/> (28 May 2020).

[37] "MicroLED on the Cusp | Radiant Vision Systems.", <https://www.radiantvisionsystems.com/blog/microled-cusp> (28 May 2020).

[38] "Microsoft's HoloLens 2: a $3500 mixed reality headset for the factory - The Verge.", <https://www.theverge.com/2019/2/24/18235460/microsoft-hololens-2-price-specs-mixed-reality-ar-vr-business-work-features-mwc-2019> (28 May 2020).

[39] "Exclusive: Intel's new Vaunt smart glasses actually look good - The Verge.", <https://www.theverge.com/2018/2/5/16966530/intel-vaunt-smart-glasses-announced-ar-video> (28 May 2020).

[40] "HoloLens 2—Pricing and Options | Microsoft HoloLens.", <https://www.microsoft.com/en-us/hololens/buy> (10 June 2020).

[41] "Lasers Are Not Magic | Doc-Ok.org.", <http://doc-ok.org/?p=1386> (10 June 2020).

[42] Jewell, J. L. and Olbright, G. R., "VERTICAL-CAVITY SURFACE EMITTING LASER ASSAY DISPLAY SYSTEM," 5,325,386 (1994).

[43] John Robbins, S., "MEMS laser scanner having enlarged FOV" (2013).

[44] Murison, M., "Intel Vaunt smart glasses locked up for good? | Internet of Business," <https://internetofbusiness.com/intel-vault-smart-glasses-cancelled/> (27 September 2018).

[45] Olwal, A. and Kress, B., "1D Eyewear: Peripheral, Hidden LEDs and Near-Eye Holographic Displays for Unobtrusive Augmentation," Proc. 2018 ACM Int. Symp. Wearable Comput.(Figure 1), 184–187 (2018).

[46] "Tobii Spotlight's foveated rendering can cut VR graphics load by 57% | VentureBeat.", <https://venturebeat.com/2019/07/30/tobii-spotlight-uses-foveated-rendering-to-cut-vr-graphics-load-by-57/> (10 June 2020).

[47] Sangu, S., Shimokawa, T. and Tanaka, S., "Ultracompact eye and pupil tracking device using VCSEL arrays and position sensitive detector," Opt. Archit. Displays Sens. Augment. Virtual, Mix. Real. (AR, VR, MR) **11310**, B. C. Kress and C. Peroz, Eds., 50, SPIE (2020).

[48] "Foveated Rendering Is Essential To Consumer VR's 2nd Generation.", <https://uploadvr.com/foveated-rendering-matters/> (28 May 2020).

[49] Sarkar, N., O'Hanlon, B., Rohani, A., Strathearn, D., Lee, G., Olfat, M. and Mansour, R. R., "A resonant eye-tracking microsystem for velocity estimation of saccades and foveated rendering," Proc. IEEE Int. Conf. Micro Electro Mech. Syst., 304–307, Institute of Electrical and Electronics Engineers Inc. (2017).

[50] Maruska, H. P. and Rhines, W. C., "A modern perspective on the history of semiconductor nitride blue light sources," Solid. State. Electron. **111**, 32–41 (2015).

[51] Monavarian, M., Rashidi, A. and Feezell, D., "A Decade of Nonpolar and Semipolar III-Nitrides: A Review of Successes and Challenges," Phys. status solidi **216**(1), 1800628 (2018).

[52] Yang, F. H., "Modern metal-organic chemical vapor deposition (MOCVD) reactors and growing nitride-based materials," [Nitride Semiconductor Light-Emitting Diodes (LEDs): Materials, Technologies and Applications], Elsevier Ltd., 27–65 (2013).

[53] Vlamidir, D., T. Paul, C., Steven P., D., Michael S., S., Michael G., S. and George, W., "High-Temperature Electronics in Europe," 1–180 (2000).

[54] Zhang, Z., Fang, H., Yao, Q., Yan, H. and Gan, Z., "Species transport and chemical reaction in a MOCVD reactor and their influence on the GaN growth uniformity," J. Cryst. Growth **454**, 87–95 (2016).

[55] Zhang, Z., Liu, Z. and Fang, H., "Influences of growth parameters on the reaction pathway during GaN synthesis," J. Cryst. Growth **482**, 44–55 (2018).

[56] Mihopoulos, T., "Reaction and Transport Processes in OMCVD : Selective and Group III-Nitride Growth" (1999).

[57] Koukitu, A., Takahashi, N. and Seki, H., "Thermodynamic study on metalorganic vapor-phase epitaxial growth of group III nitrides," Japanese J. Appl. Physics, Part 2 Lett. **36**(9 A/B), L1136 (1997).

[58] Koleske, D. D., Wickenden, A. E., Henry, R. L. and Twigg, M. E., "Influence of MOVPE growth conditions on carbon and silicon concentrations in GaN," J. Cryst. Growth **242**(1–2), 55–69 (2002).

[59] Ishibashi, A., Takeishi, H., Mannoh, M., Yabuuchi, Y. and Ban, Y., "Residual impurities in GaN/Al2O3 grown by metalorganic vapor phase epitaxy," J. Electron. Mater. **25**(5), 799–803 (1996).

[60] Qin, H., Luan, X., Feng, C., Yang, D. and Zhang, G., "Mechanical, thermodynamic and electronic properties of wurtzite and zinc-blende GaN crystals," Materials (Basel). **10**(12) (2017).

[61] Zhu, D. and Humphreys, C. J., "Solid-state lighting based on light emitting diode technology," [Optics in Our Time], Springer International Publishing, 87–118 (2016).

[62] Leonard, J. T., "III-Nitride Vertical-Cavity Surface-Emitting Lasers Growth, Fabrication, and Design of Dual Dielectric DBR Nonpolar VCSELs" (2016).

[63] Däubler, J., Passow, T., Aidam, R., Köhler, K., Kirste, L., Kunzer, M. and Wagner, J., "Long wavelength emitting GaInN quantum wells on metamorphic GaInN buffer layers with enlarged in-plane lattice parameter," Appl. Phys. Lett. **105**(11) (2014).

[64] Chichibu, S. F., Uedono, A., Onuma, T., Haskell, B. A., Chakraborty, A., Koyama, T., Fini, P. T., Keller, S., Denbaars, S. P., Speck, J. S., Mishra, U. K., Nakamura, S., Yamaguchi, S., Kamiyama, S., Amano, H., Akasaki, I., Han, J. and Sota, T., "Origin of defect-insensitive emission probability in In-containing (Al,In,Ga)N alloy semiconductors," Nat. Mater. **5**(10), 810–816 (2006).

[65] Speck, J. S. and Chichibu, S. F., "Nonpolar and Semipolar Group III Nitride-Based Materials," MRS Bull **34**, 304–309 (2009).

[66] Romanov, A. E., Baker, T. J., Nakamura, S. and Speck, J. S., "Strain-induced polarization in wurtzite III-nitride semipolar layers," J. Appl. Phys. **100**(2) (2006).

[67] Feezell, D. F., Speck, J. S., Denbaars, S. P. and Nakamura, S., "Semipolar 2021 InGaN / GaN Light-Emitting Diodes for High-Ef fi ciency Solid-State Lighting," J. Disp. Technol. **9**(4), 190–198 (2013).

[68] Mounir, C., Koslow, I. L., Wernicke, T., Kneissl, M., Kuritzky, L. Y., Adamski, N. L., Oh, S. H., Pynn, C. D., DenBaars, S. P., Nakamura, S., Speck, J. S. and Schwarz, U. T., "On the optical polarization properties of semipolar (20 2 ¯ 1) and (20 2 ¯ 1 ¯) InGaN/GaN quantum wells," J. Appl. Phys. **123**(8), 085705 (2018).

[69] Zhao, Y., Tanaka, S., Yan, Q., Huang, C.-Y., Chung, R. B., Pan, C.-C., Fujito, K., Feezell, D., Van de Walle, C. G., Speck, J. S., DenBaars, S. P. and Nakamura, S., "High optical polarization ratio from semipolar (202¯1¯) blue-green InGaN/GaN light-emitting diodes," Appl. Phys. Lett. **99**(5), 051109 (2011).

[70] Schade, L., Schwarz, U. T., Wernicke, T., Weyers, M. and Kneissl, M., "Impact of band structure and transition matrix elements on polarization properties of the photoluminescence of semipolar and nonpolar InGaN quantum wells," Phys. status solidi **248**(3), 638–646 (2011).

[71] Park, S. H., "Crystal orientation effects on many-body optical gain of wurtzite InGaN/GaN quantum well lasers," Japanese J. Appl. Physics, Part 2 Lett. **42**(2 B) (2003).

[72] Leung, B., Wang, D., Kuo, Y.-S. and Han, J., "Complete orientational access for semipolar GaN devices on sapphire," Phys. status solidi **253**(1), 23–35 (2016).

[73] Wernicke, T., Schade, L., Netzel, C., Rass, J., Hoffmann, V., Ploch, S., Knauer, A., Weyers, M., Schwarz, U. and Kneissl, M., "Indium incorporation and emission wavelength of polar, nonpolar and semipolar InGaN quantum wells," Semicond. Sci. Technol. **27**(2), 024014 (2012).

[74] Holder, C., Speck, J. S., DenBaars, S. P., Nakamura, S. and Feezell, D., "Demonstration of Nonpolar GaN-Based Vertical-Cavity Surface-Emitting Lasers," Appl. Phys. Express **5**(9), 092104 (2012).

[75] Holder, C. O., Leonard, J. T., Farrell, R. M., Cohen, D. A., Yonkee, B., Speck, J. S., Denbaars, S. P., Nakamura, S. and Feezell, D. F., "Nonpolar III-nitride vertical-cavity surface emitting lasers with a polarization ratio of 100% fabricated using photoelectrochemical etching," Appl. Phys. Lett. **105**(3), 1–6 (2014).

[76] Leonard, J. T., Young, E. C., Yonkee, B. P., Cohen, D. A., Shen, C., Margalith, T., Ng, T. K., DenBaars, S. P., Ooi, B. S., Speck, J. S. and Nakamura, S., "Comparison of nonpolar III-

nitride vertical-cavity surface-emitting lasers with tunnel junction and ITO intracavity contacts," 97481B (2016).

[77] Forman, C. A., Lee, S., Young, E. C., Kearns, J. A., Cohen, D. A., Leonard, J. T., Margalith, T., DenBaars, S. P. and Nakamura, S., "Continuous-wave operation of *m* -plane GaN-based vertical-cavity surface-emitting lasers with a tunnel junction intracavity contact," Appl. Phys. Lett. **112**(11), 111106 (2018).

[78] Hamaguchi, T., Nakajima, H., Ito, M., Mitomo, J., Satou, S., Fuutagawa, N. and Narui, H., "Lateral carrier confinement of GaN-based vertical-cavity surface-emitting diodes using boron ion implantation," Jpn. J. Appl. Phys. **55**(12), 122101 (2016).

[79] Wu, J.-Z., Long, H., Shi, X., Ying, L., Zheng, Z. and Zhang, B.-P., "Reduction of Lasing Threshold of GaN-Based Vertical-Cavity Surface-Emitting Lasers by Using Short Cavity Lengths," IEEE Trans. Electron Devices **65**(6), 1–5 (2018).

[80] Kelchner, K. M., Kuritzky, L. Y., Nakamura, S., Denbaars, S. P. and Speck, J. S., "Stable vicinal step orientations in m-plane GaN," J. Cryst. Growth **411**, 56–62 (2015).

[81] Lu, T. C., Kao, T. T., Chen, S. W., Kao, C. C., Kuo, H. C. and Wang, S. C., "CW lasing of current injection blue GaN-based vertical cavity surface emitting lasers," 2008 Conf. Quantum Electron. Laser Sci. Conf. Lasers Electro-Optics, CLEO/QELS **141102**(2008), 1–4 (2008).

[82] Forman, C. A., Lee, S. G., Young, E. C., Kearns, J., Cohen, D. A., Leonard, J. T., Margalith, T., DenBaars, S. P. and Nakamura, S., "Continuous-wave operation of nonpolar GaN-based vertical-cavity surface-emitting lasers," Proc. SPIE, 83, SPIE-Intl Soc Optical Eng (2018).

[83] Hamaguchi, T., Hoshina, Y., Hayashi, K., Tanaka, M., Ito, M., Ohara, M., Jyoukawa, T., Kobayashi, N., Watanabe, H., Yokozeki, M., Koda, R. and Yanashima, K., "Room-temperature continuous-wave operation of green vertical-cavity surface-emitting lasers with a curved mirror fabricated on {20−21} semi-polar GaN," Appl. Phys. Express **13**(4) (2020).

[84] Mei, Y., Weng, G.-E., Zhang, B.-P., Liu, J.-P., Hofmann, W., Ying, L.-Y., Zhang, J.-Y., Li, Z.-C., Yang, H. and Kuo, H.-C., "Quantum dot vertical-cavity surface-emitting lasers covering the 'green gap,'" Light Sci. Appl. **6**(1), e16199–e16199 (2017).

[85] Kawaguchi, M., Imafuji, O., Nagamatsu, K., Yamanaka, K., Takigawa, S. and Katayama, T., "Design and lasing characteristics of GaN vertical elongated cavity surface emitting lasers," Proc. SPIE **8986**, 89861K (2014).

[86] Hamaguchi, T., Tanaka, M., Mitomo, J., Nakajima, H., Ito, M., Ohara, M., Kobayashi, N., Fujii, K., Watanabe, H., Satou, S., Koda, R. and Narui, H., "Lateral optical confinement of GaN-based VCSEL using an atomically smooth monolithic curved mirror," Sci. Rep. **8**(1), 10350 (2018).

[87] Cosendey, G., Castiglia, A., Rossbach, G., Carlin, J. F. and Grandjean, N., "Blue monolithic AlInN-based vertical cavity surface emitting laser diode on free-standing GaN substrate," Appl. Phys. Lett. **101**(15), 151113 (2012).

[88] Liu, W.-J., Hu, X.-L., Ying, L.-Y., Zhang, J.-Y. and Zhang, B.-P., "Room temperature continuous wave lasing of electrically injected GaN-based vertical cavity surface emitting lasers," Appl. Phys. Lett. **104**(25), 251116 (2014).

[89] Onishi, T., Imafuji, O., Nagamatsu, K., Kawaguchi, M., Yamanaka, K. and Takigawa, S., "Continuous Wave Operation of GaN Vertical Cavity Surface Emitting Lasers at Room Temperature," IEEE J. Quantum Electron. **48**(9), 1107–1112 (2012).

[90] Kuramoto, M., Kobayashi, S., Tazawa, K., Tanaka, K., Akagi, T. and Saito, T., "In-phase supermode operation in GaN-based vertical-cavity surface-emitting laser," Appl. Phys. Lett. **115**(4), 041101 (2019).

[91] Kuramoto, M., Kobayashi, S., Akagi, T., Tazawa, K., Tanaka, K., Saito, T. and Takeuchi, T., "High-output-power and high-temperature operation of blue GaN-based vertical-cavity surface-emitting laser" (2018).

[92] Kuramoto, M., Kobayashi, S., Akagi, T., Tazawa, K., Tanaka, H. and Takeuchi, T., "Nano-height cylindrical waveguide in GaN-based vertical-cavity surface-emitting lasers," Appl. Phys. Express **13**(8), 082005 (2020).

[93] Omae, K., Higuchi, Y., Nakagawa, K., Matsumura, H. and Mukai, T., "Improvement in Lasing Characteristics of GaN-based Vertical-Cavity Surface-Emitting Lasers Fabricated Using a GaN Substrate," Appl. Phys. Express **2**(5), 052101 (2009).

[94] Yasar, S., Bilican, I., Oduncuoglu, M., Agan, S. and Uluer, I., "The Theoretical Investigation of InGaAs/GaAs Quantum Well Lasers Systems," Online (2015).

[95] Mehta, K., Liu, Y. S., Wang, J., Jeong, H., Detchprohm, T., Dupuis, R. D. and Yoder, P. D., "Thermal Design Considerations for III-N Vertical-Cavity Surface-Emitting Lasers Using Electro-Opto-Thermal Numerical Simulations," IEEE J. Quantum Electron. **55**(5) (2019).

[96] Sarzala, R. P., Piskorski, L., Czyszanowski, T. and Dems, M., "Influence of various bottom DBR designs on the thermal properties of blue semiconductor-metal subwavelength-grating VCSELs," Materials (Basel). **12**(19) (2019).

[97] Tien-Chang Lu, Jun-Rong Chen, Shih-Wei Chen, Hao-Chung Kuo, Chien-Cheng Kuo, Cheng-Chung Lee and Shing-Chung Wang., "Development of GaN-Based Vertical-Cavity Surface-Emitting Lasers," IEEE J. Sel. Top. Quantum Electron. **15**(3), 850–860 (2009).

[98] Lu, T.-C., Kao, C.-C., Kuo, H.-C., Huang, G.-S. and Wang, S.-C., "CW lasing of current injection blue GaN-based vertical cavity surface emitting laser," Appl. Phys. Lett. **92**(14), 141102 (2008).

[99] Lu, T. C., Chen, J. R., Chen, S. W., Kuo, H. C., Kuo, C. C., Lee, C. C. and Wang, S. C., "Development of GaN-based vertical-cavity surface-emitting lasers," IEEE J. Sel. Top. Quantum Electron. **15**(3), 850–860 (2009).

[100] Ikeyama, K., Kozuka, Y., Matsui, K., Yoshida, S., Akagi, T., Akatsuka, Y., Koide, N., Takeuchi, T., Kamiyama, S., Iwaya, M. and Akasaki, I., "Room-temperature continuous-wave operation of GaN-based vertical-cavity surface-emitting lasers with n-type conducting AlInN/GaN distributed Bragg reflectors," Appl. Phys. Express **9**(10), 102101 (2016).

[101] Muranaga, W., Akagi, T., Fuwa, R., Yoshida, S., Ogimoto, J., Akatsuka, Y., Iwayama, S., Takeuchi, T., Kamiyama, S., Iwaya, M. and Akasaki, I., "GaN-based vertical-cavity surface-emitting lasers using n-type conductive AlInN/GaN bottom distributed Bragg reflectors with graded interfaces," Jpn. J. Appl. Phys. **58**(SCCC01) (2019).

[102] Zhang, C., Park, S. H., Chen, D., Lin, D. W., Xiong, W., Kuo, H. C., Lin, C. F., Cao, H. and Han, J., "Mesoporous GaN for Photonic Engineering-Highly Reflective GaN Mirrors as an Example," ACS Photonics **2**(7), 980–986 (2015).

[103] Chen, D., Xiao, H. and Han, J., "Nanopores in GaN by electrochemical anodization in hydrofluoric acid: Formation and mechanism," J. Appl. Phys. **112**(6), 064303 (2012).

[104] Zhang, Y., Ryu, S.-W., Yerino, C., Leung, B., Sun, Q., Song, Q., Cao, H. and Han, J., "A conductivity-based selective etching for next generation GaN devices," Phys. status solidi **247**(7), 1713–1716 (2010).

[105] Mishkat-Ul-Masabih, S. M., Aragon, A. A., Monavarian, M., Luk, T. S. and Feezell, D. F., "Electrically injected nonpolar GaN-based VCSELs with lattice-matched nanoporous distributed Bragg reflector mirrors," Appl. Phys. Express **12**(3), 036504 (2019).

[106] Kasahara, D., Morita, D., Kosugi, T., Nakagawa, K., Kawamata, J., Higuchi, Y., Matsumura, H. and Mukai, T., "Demonstration of Blue and Green GaN-Based Vertical-Cavity Surface-Emitting Lasers by Current Injection at Room Temperature," Appl. Phys. Express **4**(7), 072103 (2011).

[107] Higuchi, Y., Omae, K., Matsumura, H. and Mukai, T., "Room-Temperature CW Lasing of a GaN-Based Vertical-Cavity Surface-Emitting Laser by Current Injection," Appl. Phys. Express **1**(12), 121102 (2008).

[108] Hamaguchi, T., Fuutagawa, N., Izumi, S., Murayama, M. and Narui, H., "Milliwatt-class GaN-based blue vertical-cavity surface-emitting lasers fabricated by epitaxial lateral overgrowth," Phys. status solidi **213**(5), 1170–1176 (2016).

[109] Hamaguchi, T., Nakajima, H., Tanaka, M., Ito, M., Ohara, M., Jyoukawa, T., Kobayashi, N., Matou, T., Hayashi, K., Watanabe, H., Koda, R. and Yanashima, K., "Sub-milliampere-threshold continuous wave operation of GaN-based vertical-cavity surface-emitting laser with lateral optical confinement by curved mirror," Appl. Phys. Express **12**(4), 044004 (2019).

[110] Izumi, S., Fuutagawa, N., Hamaguchi, T., Murayama, M., Kuramoto, M. and Narui, H., "Room-temperature continuous-wave operation of GaN-based vertical-cavity surface-emitting lasers fabricated using epitaxial lateral overgrowth," Appl. Phys. Express **8**(6), 062702 (2015).

[111] Sarzla, R. P., Spiewak, P. and Wasiak, M., "Influence of resonator length on performance of nitride TJ VCSEL," IEEE J. Quantum Electron. **55**(6), 1–1 (2019).

[112] Leonard, J. T., Cohen, D. A., Yonkee, B. P., Farrell, R. M., DenBaars, S. P., Speck, J. S. and Nakamura, S., "Smooth e-beam-deposited tin-doped indium oxide for III-nitride vertical-cavity surface-emitting laser intracavity contacts," J. Appl. Phys. **118**(14), 145304 (2015).

[113] Lee, S., Forman, C. A., Lee, C., Kearns, J., Young, E. C., Leonard, J. T., Cohen, D. A., Speck, J. S., Nakamura, S. and DenBaars, S. P., "GaN-based vertical-cavity surface-emitting lasers with tunnel junction contacts grown by metal-organic chemical vapor deposition," Appl. Phys. Express **11**(6), 062703 (2018).

[114] Hashemi, E., Gustavsson, J., Bengtsson, J., Stattin, M., Cosendey, G., Grandjean, N. and Haglund, A., "Engineering the lateral optical guiding in gallium nitride-based vertical-cavity surface-emitting laser cavities to reach the lowest threshold gain," Jpn. J. Appl. Phys. **52** (2013).

[115] Hashemi, E., Bengtsson, J., Gustavsson, J., Stattin, M., Cosendey, G., Grandjean, N. and Haglund, Å., "Analysis of structurally sensitive loss in GaN-based VCSEL cavities and its effect on modal discrimination," Opt. Express **22**(1), 411 (2014).

[116] Hashemi, E., Bengtsson, J., Gustavsson, J., Calciati, M., Goano, M. and Haglund, Å., "Thermal lensing effects on lateral leakage in GaN-based vertical-cavity surface-emitting laser cavities," Opt. Express **25**(9), 9556 (2017).

[117] Hayashi, N., Ogimoto, J., Matsui, K., Furuta, T., Akagi, T., Iwayama, S., Takeuchi, T.,

Kamiyama, S., Iwaya, M. and Akasaki, I., "A GaN-Based VCSEL with a Convex Structure for Optical Guiding," Phys. status solidi **215**(10), 1700648 (2018).

[118] Kuramoto, M., Kobayashi, S., Akagi, T., Tazawa, K., Tanaka, K., Saito, T. and Takeuchi, T., "Enhancement of slope efficiency and output power in GaN-based vertical-cavity surface-emitting lasers with a SiO_2 -buried lateral index guide," Appl. Phys. Lett. **112**(11), 111104 (2018).

[119] Leonard, J. T., Cohen, D. A., Yonkee, B. P., Farrell, R. M., Margalith, T., Lee, S., DenBaars, S. P., Speck, J. S. and Nakamura, S., "Nonpolar III-nitride vertical-cavity surface-emitting lasers incorporating an ion implanted aperture," Appl. Phys. Lett. **107**(1), 011102 (2015).

[120] Uzan-Saguy, C., Salzman, J., Kalish, R., Richter, V., Tish, U., Zamir, S. and Prawer, S., "Electrical isolation of GaN by ion implantation damage: Experiment and model," Appl. Phys. Lett. **74**(17), 2441 (1999).

[121] Pearton, S. J., Vartuli, C. B., Zolper, J. C., Yuan, C. and Stall, R. A., "Ion implantation doping and isolation of GaN," Appl. Phys. Lett. **67**(10), 1435–1437 (1995).

[122] Ronning, C., Dalmer, M., Uhrmacher, M., Restle, M., Vetter, U., Ziegeler, L., Hofsäss, H., Gehrke, T., Järrendahl, K., Davis, R. F. and Collaboration, I., "Ion implanted dopants in GaN and AlN: Lattice sites, annealing behavior, and defect recovery," J. Appl. Phys. **87**(5), 2149 (2000).

[123] Wong, P. S., Yan, J., Wu, T. C., Kyi, W., Pao, J. and Riaziat, M., "Tunnel junction 850-nm VCSEL for aperture uniformity and reliability," 25 February 2017, 101220B, International Society for Optics and Photonics.

[124] Hofmann, W., "High-speed buried tunnel junction vertical-cavity surface-emitting lasers," IEEE Photonics J. **2**(5), 802–815 (2010).

[125] Marjani, S., Hosseini, S. E. and Faez, R., "Threshold characteristics analysis of InP-based PhC VCSEL with buried tunnel junction," 2013 21st Iran. Conf. Electr. Eng., 1–4, IEEE (2013).

[126] Lee, S., Forman, C. A., Kearns, J., Leonard, J. T., Cohen, D. A., Nakamura, S. and DenBaars, S. P., "Demonstration of GaN-based vertical-cavity surface-emitting lasers with buried tunnel junction contacts," Opt. Express **27**(22), 31621–31628 (2019).

[127] Leonard, J. T., Yonkee, B. P., Cohen, D. A., Megalini, L., Lee, S., Speck, J. S., DenBaars, S. P. and Nakamura, S., "Nonpolar III-nitride vertical-cavity surface-emitting laser with a photoelectrochemically etched air-gap aperture," Appl. Phys. Lett. **108**(3), 031111 (2016).

[128] Yeh, P. S., Chang, C.-C., Chen, Y.-T., Lin, D.-W., Liou, J.-S., Wu, C. C., He, J. H. and Kuo, H.-C., "GaN-based vertical-cavity surface emitting lasers with sub-milliamp threshold and small divergence angle," Appl. Phys. Lett. **109**(24), 241103 (2016).

[129] Bandres, M. A. and Gutiérrez-Vega, J. C., "Ince–Gaussian modes of the paraxial wave equation and stable resonators," J. Opt. Soc. Am. A **21**(5), 873 (2004).

[130] "Optical resonators and Gaussian beams - Laguerre-Gaussian Modes.", <http://www.optique-ingenieur.org/en/courses/OPI_ang_M01_C03/co/Contenu_14.html> (11 June 2020).

[131] Schwarz, U. T., Bandres, M. A. and Gutiérrez-Vega, J. C., "Observation of Ince–Gaussian modes in stable resonators," Opt. Lett. **29**(16), 1870 (2004).

[132] Leonard, J. T., Young, E. C., Yonkee, B. P., Cohen, D. A., Margalith, T., DenBaars, S. P.,

Speck, J. S. and Nakamura, S., "Demonstration of a III-nitride vertical-cavity surface-emitting laser with a III-nitride tunnel junction intracavity contact," Appl. Phys. Lett. **107**(9), 091105 (2015).

[133] Kuc, M., Sarzaa, R. P. and Nakwaski, W., "Physics of mode selectivity of vertical-cavity surface-emitting diode lasers," J. Appl. Phys. **108**(4) (2010).

[134] Nakwaski, W., "VCSEL structures used to suppress higher-order transverse modes," Opto-electronics Rev. **19**(1), 119–129 (2011).

[135] Unold, H. J., Mahmoud, S. W. Z., Jäger, R., Grabherr, M., Michalzik, R. and Ebeling, K. J., "Large-area single-mode VCSELs and the self-aligned surface relief," IEEE J. Sel. Top. Quantum Electron. **7**(2), 386–392 (2001).

[136] Nakajima, H., Hamaguchi, T., Tanaka, M., Ito, M., Jyokawa, T., Matou, T., Hayashi, K., Ohara, M., Kobayashi, N., Watanabe, H., Koda, R. and Yanashima, K., "Single transverse mode operation of GaN-based vertical-cavity surface-emitting laser with monolithically incorporated curved mirror," Appl. Phys. Express **12**(8), 084003 (2019).

[137] Haller, C., Carlin, J.-F., Jacopin, G., Liu, W., Martin, D., Butté, R. and Grandjean, N., "GaN surface as the source of non-radiative defects in InGaN/GaN quantum wells," Appl. Phys. Lett. **113**(11), 111106 (2018).

[138] Scheibenzuber, W. G., Schwarz, U. T., Sulmoni, L., Dorsaz, J., Carlin, J. F. and Grandjean, N., "Recombination coefficients of GaN-based laser diodes," J. Appl. Phys. **109**(9), 093106 (2011).

[139] Hao, M., Ishikawa, H., Egawa, T., Shao, C. L. and Jimbo, T., "Anomalous compositional pulling effect in InGaN/GaN multiple quantum wells," Appl. Phys. Lett. **82**(26), 4702–4704 (2003).

[140] Pereira, S., Correia, M. R., Pereira, E., O'donnell, K. P., Trager-Cowan, C., Sweeney, F. and Alves, E., "Compositional pulling effects in In x Ga 1Àx NÕGaN layers: A combined depth-resolved cathodoluminescence and Rutherford backscatteringÕchanneling study."

[141] Forman, C. A., "Achieving Continuous-Wave Lasing for Violet m -plane GaN-Based Vertical-Cavity Surface-Emitting Lasers" (2018).

[142] "Room-temperature photoenhanced wet etching of GaN.", Appl. Phys. Lett. **68**(11), 1531 (1996).

[143] Lee, S., Mishkat-Ul-Masabih, S., Leonard, J. T., Feezell, D. F., Cohen, D. A., Speck, J. S., Nakamura, S. and DenBaars, S. P., "Smooth and selective photo-electrochemical etching of heavily doped GaN:Si using a mode-locked 355nm microchip laser," Appl. Phys. Express **10**(1) (2017).

[144] Jayaprakash, R., Kalaitzakis, F. G., Kayambaki, M., Tsagaraki, K., Monroy, E. and Pelekanos, N. T., "Ultra-smooth GaN membranes by photo-electrochemical etching for photonic applications," J. Mater. Sci. **49**(11), 4018–4024 (2014).

[145] Youtsey, C., Adesida, I. and Bulman, G., "Highly anisotropic photoenhanced wet etching of n-type GaN," Appl. Phys. Lett. **71**(15), 2151–2153 (1997).

[146] Youtsey, C., Adesida, I., Romano, L. T. and Bulman, G., "Smooth n-type GaN surfaces by photoenhanced wet etching," Appl. Phys. Lett. **72**(5), 560–562 (1998).

[147] Xiao, X., Fischer, A. J., Coltrin, M. E., Lu, P., Koleske, D. D., Wang, G. T., Polsky, R. and Tsao, J. Y., "Photoelectrochemical etching of epitaxial InGaN thin films: Self-limited kinetics and nanostructuring," Electrochim. Acta **162**, 163–168 (2015).

[148] Morkoc, H., [Handbook of Nitride Semiconductors and Devices, Electronic and Optical Processes in Nitrides], John Wiley & Sons, Ltd (2009).

[149] Lin, M. S., Lin, C. F., Huang, W. C., Wang, G. M., Shieh, B. C., Dai, J. J., Chang, S. Y., Wuu, D. S., Liu, P. L. and Horng, R. H., "Chemical-mechanical lift-off process for InGaN epitaxial layers," Appl. Phys. Express **4**(6) (2011).

[150] Search, H., Journals, C., Contact, A., Iopscience, M. and Address, I. P., "Anomalous Electrochemical Behavior of N-Type GaN Films on α-Al2O3 Substrates Anomalous Electrochemical Behavior of N-Type GaN Films on α -Al 2 O 3 Substrates," Jpn. J. Appl. Phys **38**(4B), 26192621 (1999).

[151] Abbas, A. S., Alyamani, A. Y., Nakamura, S. and Dembaars, S. P., "Enhancement of n-type GaN (20–21) semipolar surface morphology in photo-electrochemical undercut etching," Appl. Phys. Express **12**(3), 036503 (2019).

[152] Ping, A. T., Chen, Q., Yang, J. W., Asif Khan, M. and Adesida, I., "The effects of reactive ion etching-induced damage on the characteristics of ohmic contacts to n-type GaN," J. Electron. Mater. (1998).

[153] Mehta, K., Liu, Y.-S., Wang, J., Jeong, H., Detchprohm, T., Park, Y. J., Alugubelli, S. R., Wang, S., Ponce, F. A., Shen, S.-C., Dupuis, R. D. and Yoder, P. D., "Theory and Design of Electron Blocking Layers for III-N-Based Laser Diodes by Numerical Simulation," IEEE J. Quantum Electron. **54**(6), 1–11 (2018).

[154] Kuwano, Y., Kaga, M., Morita, T., Yamashita, K., Yagi, K., Iwaya, M., Takeuchi, T., Kamiyama, S. and Akasaki, I., "Lateral Hydrogen Diffusion at p-GaN Layers in Nitride-Based Light Emitting Diodes with Tunnel Junctions," Jpn. J. Appl. Phys. **52**(8S), 08JK12 (2013).

[155] Kearns, J. A., Back, J., Cohen, D. A., DenBaars, S. P. and Nakamura, S., "Demonstration of blue semipolar ($20\bar{2}\bar{1}$) GaN-based vertical-cavity surface-emitting lasers," Opt. Express **27**(17), 23707 (2019).

[156] Coldren, L. A., Corzine, S. W. and Masanovic, M. L., [Diode lasers and photonic integrated circuits, 2nd ed.], Wiley (2012).

[157] Becerra, D. L., Cohen, D. A., Mehari, S., DenBaars, S. P. and Nakamura, S., "Compensation effects of high oxygen levels in semipolar AlGaN electron blocking layers and their mitigation via growth optimization," J. Cryst. Growth **507**, 118–123 (2019).

[158] Łódzka, P., Fizyki, I. and Fotoniki, Z., "Wpływ niedokładności wykonania wybranych elementów azotkowego lasera VCSEL na jego charakterystyki emisyjne," Prz. Elektrotechniczny **09**, 127 (2019).

[159] Johnson, P. and Christy, R., "Optical constants of transition metals: Ti, V, Cr, Mn, Fe, Co, Ni, and Pd," Phys. Rev. B **9**(12), 5056–5070 (1974).

[160] Johnson, P. B. and Christy, R. W., "Optical Constants of the Noble Metals," Phys. Rev. B **6**(12), 4370–4379 (1972).

[161] Tong, H., Zhao, H., Handara, V. A., Herbsommer, J. A. and Tansu, N., "Analysis of thermoelectric characteristics of AlGaN and InGaN semiconductors," Phys. Simul.

Optoelectron. Devices XVII **7211**(February 2009), 721103 (2009).

[162] Kearns, J. A., Back, J., Palmquist, N. C., Cohen, D. A., DenBaars, S. P. and Nakamura, S., "Inhomogeneous Current Injection and Filamentary Lasing of Semipolar (2021¯) Blue GaN-Based Vertical-Cavity Surface-Emitting Lasers with Buried Tunnel Junctions," Phys. status solidi **217**(7), 1900718 (2020).

[163] Hull, B. A., Mohney, S. E., Venugopalan, H. S. and Ramer, J. C., "Influence of oxygen on the activation of p-type GaN," Appl. Phys. Lett. **76**(16), 2271–2273 (2000).

[164] Lu, W., Aplin, D., Clawson, A. R. and Yu, P. K. L., "Effects of the gas ambient in thermal activation of Mg-doped p-GaN on Hall effect and photoluminescence," J. Vac. Sci. Technol. A Vacuum, Surfaces, Film. **31**(1), 011502 (2013).

[165] Mehari, S., Cohen, D. A., Becerra, D. L., Nakamura, S. and DenBaars, S. P., "Semipolar InGaN blue laser diodes with a low optical loss and a high material gain obtained by suppression of carrier accumulation in the p-waveguide region," Jpn. J. Appl. Phys. **58**(2), 020902 (2019).

[166] Wada, H., Babić, D. I., Ishikawa, M. and Bowers, J. E., "Effects of nonuniform current injection in GaInAsP/InP vertical- cavity lasers," Appl. Phys. Lett. **60**(24), 2974–2976 (1992).

[167] Sekiguchi, S., Miyamoto, T., Kimura, T., Okazaki, G., Koyama, F. and Iga, K., "Improvement of current injection uniformity and device resistance in long-wavelength vertical-cavity surface-emitting laser using a tunnel junction," Japanese J. Appl. Physics, Part 1 Regul. Pap. Short Notes Rev. Pap. **39**(7 A), 3997–4001 (2000).

[168] Michalzik, R., [VCSELs : fundamentals, technology and applications of vertical-cavity surface-emitting lasers], Springer (2013).

[169] Khromov, S., Gregorius, D., Schiller, R., Lösch, J., Wahl, M., Kopnarski, M., Amano, H., Monemar, B., Hultman, L. and Pozina, G., "Atom probe tomography study of Mg-doped GaN layers," Nanotechnology **25**(27) (2014).

[170] Bennett, S. E., Ulfig, R. M., Clifton, P. H., Kappers, M. J., Barnard, J. S., Humphreys, C. J. and Oliver, R. A., "Atom probe tomography and transmission electron microscopy of a Mg-doped AlGaN/GaN superlattice," Ultramicroscopy **111**(3), 207–211 (2011).

[171] Pettersson, L. A. A., Roman, L. S. and Inganäs, O., "Modeling photocurrent action spectra of photovoltaic devices based on organic thin films," J. Appl. Phys. **86**(1), 487–496 (1999).